DEVELOPMENT OF BARIUM HEXAFERRITE COMPOSITE MATERIALS FOR MICROWAVE ABSORPTION

Wu Yuping

(B. Eng., University of Science and Technology, Beijing, P. R. China)

A THESIS SUBMITTED
FOR THE DEGREE OF DOCTOR OF PHILOSOPHY
DEPARTMENT OF PHYSICS
NATIONAL UNIVERSITY OF SINGAPORE

2006

ACKNOWLEDGEMENTS

I would like to express my sincere gratitude to my principle supervisor, Professor Ong Chong Kim, for accepting me to be his student, and for his encouragement, support and guidance with scientific insight as well as the art of presentation of ideas. He has been constructing a motivating, enthusiastic and dedicating atmosphere in the Centre for Superconducting and Magnetic Materials (CSMM), which benefits me a lot.

I am deeply indebted to my co-supervisor, Dr. Li Zheng-Wen. Thank him to help me get on my feet at the beginning. He gave me the freedom to pursue my own ideas, but was always there if things went away. His insightful questions and suggestions greatly influenced the contents of this work, and his careful comments and criticisms have shaped almost every line in this thesis.

Special thanks go to Temasek Laboratories (TLs), for the financial support with this project during these three years. I also would like to acknowledge the following individuals in TLs who contributed valuable input and assistance to this project: Prof. Lim Hock, Mr. Gan Yeow Beng, Dr. Chen Linfeng, Dr. Kong Lingbing, Dr. Liu Lie and Dr. Rao Xuesong.

My appreciation goes to Dr. Wang Shejie, Research Fellow in Institute of Materials Research and Engineering (IMRE). Thanks for his help on SEM measurements, and a lot of constructive guidance and discussion.

Many thanks also go to the Materials Science Department and the Data Storage

Institute (DSI), for the assistance on the VSM measurements.

My friends and fellow graduate students have made my graduate life full of fondness. Special thanks go to: Dr. Tan Chin Yaw, Mr. Liu Huajun, Ms. Li Qin, Mr. Chang Kok Boon, Ms. Liu Yan and Mr. Wang Peng.

Last but not least, I would like to give my heartfelt thanks to my family for their constant support and love, and most of all, my husband, Lin Guoqing, for his unending encouragement during the past three years**.** He also gave me a lot of constructive guidance and discussion on this project.

TABLE OF CONTENTS

ABSTRACT

Electromagnetic (EM) materials with strong absorbing property at microwave frequency have been used extensively in defense, industry and commerce. This study focused on developing barium hexaferrite composites for microwave absorption.

Theoretically speaking, in order to obtain low reflectivity and wide absorbing band in gigahertz (GHz), microwave absorbing materials should have large static permeability $\mu_0^{'}$, large maximum imaginary permeability $\mu_{\max}^{''}$, small permittivity $\varepsilon^{'}$ and suitable resonance frequency f_r. Therefore, this study mainly aimed to explore the possibility to improve the high-frequency magnetic properties and control the resonance frequency with ions substitution and oxides doping. Meanwhile, investigating and understanding the physical mechanisms of magnetic resonance and EM absorption were also the themes of this thesis. In addition, this study also aimed to investigate the influence of ferrite concentration on the absorbing characteristics of composites. It is hoped that, with this study, EM materials with excellent absorbing performance in microwave frequency can be obtained.

Taking into account the good magnetic property of *W*-type and *c*-plane anisotropy of *Y*-type hexaferrites, we choose these two materials for investigation in this work. All ferrite materials were fabricated by solid-state reaction. Ions substitution and oxides doping were both employed to enhance the absorbing performance by modifying the static and dynamic magnetic properties. Various techniques, such as X-ray diffraction (XRD), scanning electron microscopy (SEM), vibrating sample magnetometer (VSM),

impedance/material analyzer and vector network analyzer (VNA), were used to examine the microstructure, static magnetic properties and high-frequency characteristics of ferrites. Based on the metal-backed single-layer model, the absorbing ability of composites was estimated with the data of complex permittivity and permeability.

In order to control the resonance frequency and increase the permeability, CoZn-substituted BaW, $BaCo_xZn_{2-x}Fe_{16}O_{27}$ (x varying from 0 to 2.0), were investigated. The results showed that Co ions are able to modify the anisotropy from *c*-axis to *c*-plane at x=0.5-0.7. For BaW composites (35 vol% of ferrite powders) with *c*-plane anisotropy, the natural resonance frequency shifts from about 2.0 GHz at x=0.7 to 12.8 GHz at x=1.5. The predicted reflection loss (*RL*) indicates that the samples of x=0.7 and 1.0 are the potential candidates for microwave absorbing materials with low reflectivity and broad bandwidth covering C-band (4-8 GHz) and X-band (8-12 GHz).

Three series of substituted BaY ferrites, $Ba_2Co_xNi_{2-x}Fe_{12}O_{22}$, $Ba_2Ni_xZn_{2-x}Fe_{12}O_{22}$ and $Ba_2Zn_xCo_{2-x}Fe_{12}O_{22}$ (x varying from 0 to 2.0), were also prepared and investigated. The predicted *RL* shows that the composite (50 vol% of ferrite powders) of $Ba_2Zn_{1.2}Ni_{0.8}Fe_{12}O_{22}$ has the best absorbing property for use as EM materials. The bandwidth for absorption of more than 10 dB is from 3.9 to 11.8 GHz, and the relative bandwidth is over 3 with a thickness of 3.3 mm. On the other hand, the absorbing frequency band is changed greatly with various ions substitution. The composites with high Zn^{2+} concentration are suitable for C-band, while those with high Ni^{2+} concentration are suitable for X-band, and those with high Co^{2+} concentration are for Ku-band (12-18 GHz).

In order to enhance the static and dynamic magnetic properties, ten kinds of oxides, varied from divalent to pentavalent, were doped in $BaCoZnFe_{16}O_{27}$ separately. The results showed that V_2O_5 is mostly promising to increase the permeability. Comparing with the undoped sample, the permeabilities $\mu_0^{'}$ and $\mu_{max}^{''}$ increase by about 42 % (from 3.1 to 4.4) and 50 % (from 1.2 to 1.8), respectively, for the sample doped with 1.0 wt% of V_2O_5. Correspondingly, the maximum relative bandwidth (W_{max}) for absorption of more than 10 dB increases from 3.0 to 3.9, increasing by 30 %. In addition, it was also found that W_{max} for the composites filled with $BaCo_xZn_{2-x}Fe_{16}O_{27}$ (x=1.3 and 1.5) increases by more than 50 % with 1.0 wt% of V_2O_5 doping.

The electromagnetic and microwave absorbing characteristics were investigated for composites with various ferrite volume concentration (V_c=25, 35, 40 and 50 %). The compositions of filled ferrite powders were $BaCo_xZn_{2-x}Fe_{16}O_{27}$ with x=0.7 and 1.0. It was found that composites filling with 50 vol% ferrite powders have excellent microwave absorbing performance with suitable flexibility and density.

This study provides some useful information and physical understanding on hexaferrites for microwave absorbing applications.

(a). It has shown that V_2O_5 can significantly enhance the absorbing performance of BaW ferrites. As compared with the corresponding undoped samples, the maximum relative bandwidth W_{max} increases by 30~50 % for the composites of $BaCo_xZn_{2-x}Fe_{16}O_{27}$ $(1.0 \le x \le 1.5)$ with 1.0 wt% of V_2O_5 doping. These doped composites are suitable candidates for EM materials used in C-, X- and Ku-bands.

(b). There are two kinds of resonance mechanisms, natural resonance and domain wall resonance. For BaW and most of BaY composites, there are two resonance peaks.

The peak at high frequency is attributed to natural resonance, while the other at low frequency results from domain wall resonance. However, for BaY composites with large Zn concentration, the occurrence of three magnetic resonance peaks was observed. It was verified that the highest frequency peak is for natural resonance and the other two low frequency peaks are contributed by domain wall resonance.

(c). There are two kinds of EM absorbing mechanisms, magnetic loss and thickness loss (quarter wavelength effect); thus two dips were observed in most RL_{min}-t (minimum reflection loss versus thickness) curves, especially for the composites with large ferrite concentration. The location of the absorbing peak originated from magnetic loss is tightly related with the natural resonance frequency. However, for the composites with low ferrite content, magnetic loss is negligible and thickness loss is the major contribution of absorption. In this case, only one dip was observed in RL_{min}-t curves.

(d). It was found that the crystalline anisotropy is effectively modified with suitable ions substitution in hexaferrites, leading to a great shift of natural resonance frequency. For BaW and BaY with *c*-plane anisotropy, a linear relationship between the natural resonance frequency and anisotropy field has been verified. This result presents an effective way to control the location of absorbing frequency band, which is very useful for the design of EM materials in various frequency bands.

(e). In addition to the crystalline anisotropy, the natural resonance frequency is also related with the shape of ferrite particles. It was observed and theoretically proved, with the change in particles shape from spherical to plate-like, the natural resonance frequency is shifted to low frequency due to the demagnetizing effect.

LIST OF TABLES

Chapter 1:

Chapter 2:

Chapter 4:

Chapter 5:

Chapter 6:

Appendix A:

Appendix B:

LIST OF FIGURES

Chapter 1:

Chapter 2:

Chapter 3:

Chapter 4:

Chapter 5:

Chapter 6:

Chapter 7:

Appendix A:

ABBREVIATIONS AND SYMBOLS

Abbreviations:

EM	Electromagnetic
XRD	X-ray diffraction
SEM	Scanning electron microscopy
VSM	Vibrating sample magnetometer
VNA	Vector network analyzer
BaM	*M*-type hexaferrite, $BaFe_{12}O_{19}$
BaW or Me_2W	*W*-type hexaferrite, $BaMe_2Fe_{16}O_{27}$
BaY or Me_2Y	*Y*-type hexaferrite, $Ba_2Me_2Fe_{12}O_{22}$
BaZ or Me_2Z	*Z*-type hexaferrite, $Ba_3Me_2Fe_{24}O_{41}$
Hz	Hertz
MHz	Megahertz
GHz	Gigahertz
C-band	4-8 GHz
X-band	8-12 GHz
Ku-band	12-18 GHz

Symbols:

a, c	Lattice parameters
V	Cell volume
M_s	Saturation magnetization
H_c	Coercivity or coercive force
H_a	Anisotropy field for *c*-axis anisotropy

H_θ	Out-of-plane anisotropy field for *c*-plane anisotropy
H_ϕ	In-plane anisotropy field for *c*-plane anisotropy
$\gamma/2\pi$	Gyromagnetic ratio, 2.8 GHz/kOe
$\varepsilon = \varepsilon' - j\varepsilon''$	Complex permittivity, ε' represents the real part, ε'' is the imaginary part
$\mu = \mu' - j\mu''$	Complex permeability, μ' represents the real part, μ'' is the imaginary part
$\mu_0^{'}$	Static permeability, usually taken as the real permeability at low frequency, such as 0.1 0r 0.01 GHz
$\mu_{\max}^{''}$	Maximum imaginary permeability
f_r	Resonance frequency
f_{up} and f_{low}	Upper- and lower-frequency limits of the bandwidth for a given attenuation
W	Relative bandwidth, $W=f_{up}/f_{low}$
RL_{min}	Dip of *RL*-frequency curve
t_o	Optimum thickness, at which the relatice bandwidth W has the maximum value (W_{max})
m_o	Optimum weight of unit area for a composite
f_m	Matching frequency
t_m	Matching thickness

LIST OF PUBLICATIONS

1. Y.P. Wu, C.K. Ong, Z.W. Li, L.F. Chen, G.Q. Lin, and S.J. Wang, "Microstructural and high-frequency magnetic characteristics of *W*-type barium ferrites doped with V_2O_5", *Journal of Applied Physics*, **97**, 063909 (2005).

2. Y.P. Wu, C.K. Ong, Z.W. Li, L.F. Chen and S.J. Wang, "Effect of doping SiO_2 on high-frequency magnetic properties for *W*-type barium ferrite", *Journal of Applied Physics*, **95**, 4235 (2004).

3. Y.P. Wu, C.K. Ong, Z.W. Li and G.Q. Lin, "Improved microwave magnetic and attenuation properties due to the dopant V_2O_5 in W-type barium ferrites", *Journal of Physics D: Applied Physics*, **39**, 2915 (2006).

4. Y.P. Wu, C.K. Ong, G.Q. Lin and Z.W. Li, "Microstructure and high-frequency magnetic characteristics of V_2O_5 doped W-type barium ferrite", In *Proc. MRS-S National Conference on Advanced Materials*, Singapore, 6 August 2004.

5. Y.P. Wu, Z.W. Li, G.Q. Lin and C.K. Ong, "High-frequency magnetic properties for composites of ZnNi-substituted Y-type barium hexaferrites", *International Conference on Materials for Advanced Technologies 2007*, submitted.

6. Z.W. Li, Y.P. Wu, G.Q. Lin and L.F. Chen, "Static and dynamic magnetic properties of CoZn substituted Z-type barium ferrite $Ba_3Zn_{2-x}Co_xFe_{24}O_{41}$ composites", *Journal of Magnetism and Magnetic Materials*, **310**, 145 (2007).

7. G.Q. Lin, Y.P. Wu and Z.W. Li, "Improvement of the electromagnetic properties in composites with flake-like Co_2Z powders by molten-salt synthesis", *IEEE Transactions on Magnetics*, **42**, No. 10, 3326 (2006).

8. Z.W. Li, Y.P. Wu, G.Q. Lin and T. Liu, "The effect of V_2O_5 on high-frequency properties for *W*-type barium ferrite composites", *IEEE Transactions on Magnetics*, **42**, No. 10, 3365 (2006).

9. Z.W. Li, L.F. Chen, Y.P. Wu and C.K. Ong, "Microwave attenuation properties of *W*-type barium ferrite $BaZn_{2-x}Co_xFe_{16}O_{27}$ composites", *Journal of Applied Physics*, **96**, 534 (2004).

10. Z.W. Li, L.F. Chen, Y.P. Wu and C.K. Ong, "Magnetic characteristics of $BaCo_xZn_{2-x}Fe_{16}O_{27}$ composites at microwave frequencies", *International Conference on Materials for Advanced Technologies 2003, Proceeding of the Symposium R: Electromagnetic Materials*, Singapore, 86 (2003).

11. G.Q. Lin, Z.W. Li, Y.P. Wu and C.K. Ong, "The effect of particle size on the magnetic properties of barium ferrite", In *Proc. MRS-S National Conference on Advanced Materials*, Singapore, 6 August 2004.

12. Z.W. Li, G.Q. Lin, L.F. Chen, Y.P. Wu, and C.K. Ong, "$Co^{2+}Ti^{4+}$ substituted Z-type barium ferrite with enhanced imaginary permeability and resonance frequency", *Journal of Applied Physics*, **99**, 63905 (2006).

13. Z.W. Li, G.Q. Lin, L.F. Chen, Y.P. Wu, and C.K. Ong, "Magnetic properties of Co-Ti substituted Z-type barium ferrite $Ba_3Co_{2+x}Ti_xFe_{24-2x}O_{41}$ composites at microwave frequency", *Physical Review B*, submitted.

14. Z.W. Li, G.Q. Lin, L.F. Chen, Y.P. Wu, and C.K. Ong, "Doping effects on complex permeability spectra for W-type barium ferrite composites", *Journal of Applied Physics*, submitted.

15. G.Q. Lin, Z.W. Li, L.F. Chen, Y.P. Wu, and C.K. Ong, "Effects of doping on the high-frequency magnetic properties of barium ferrites composites", *International Conference on Materials for Advanced Technologies 2005, Proceeding of the Symposium R: Electromagnetic Materials*, Jul. 3-8, Singapore, 125-128 (2005).

16. Z.W. Li, G.Q. Lin, L.F. Chen, Y.P. Wu, and C.K. Ong, "Size effect on the static and dynamic magnetic properties for *W*-type barium ferrite composites: from micro-particles to nanoparticles", *Journal of Applied Physics*, **98**, 094310 (2005).

17. G.Q. Lin, Z.W. Li, L.F. Chen, Y.P. Wu, and C.K. Ong, "Influence of demagnetizing field on the permeability of soft magnetic composites", *Journal of Magnetism and Magnetic Materials*, **305**, 291 (2006).

CHAPTER 1: INTRODUCTION

1.1 Microwave absorbing materials

Since the Second World War, microwave radars have been used to detect distant airborne targets. The detectability of aircrafts affects not only their survival in the hostile territory but the mission success rate. Indeed radars were so overwhelmingly successful in detecting distant targets that there has been a growing and widespread interest in stealth technology. Therefore, it is necessary to explore methods to minimize the radar signal reflected from a vehicle.

There are only four basic techniques for reducing microwave or electromagnetic (EM) wave energy: shaping of the vehicle, EM absorbing materials, passive cancellation and active cancellation. The first two techniques are the most practical and are most often applied. In current stealthy aircraft designs, although shaping technique is first employed to create a platform design with inherently low radar reflection in the primary threat sectors, many situations require microwave absorbing materials to treat areas whose shape could not be optimized or to reduce the effects of creeping waves or traveling waves on the signal. Therefore, knowledge of the design and application of microwave absorbing materials is vital to minimize the radar signal.

Microwave absorbing materials are based on the fact that some substances absorb energy from electromagnetic fields passing through them. Such materials are characterized by the indices of refraction, which are complex numbers, such as permittivity ($\varepsilon = \varepsilon' - j\varepsilon''$) and permeability ($\mu = \mu' - j\mu''$). The imaginary components

in the indices of refraction (ε" and μ") account for the microwave energy loss in the materials. The loss is actually the conversion of EM wave energy into heat.

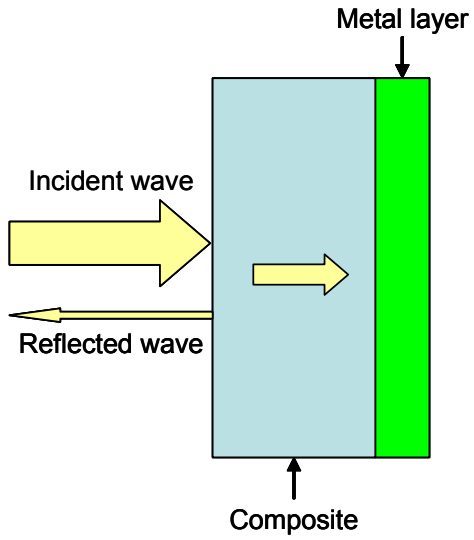

Fig. 1-1. The sketch map for the metal-backed single-layer absorber.

In practical applications, microwave absorbing materials are often coated onto other metallic structures to reduce scattering, as schematically shown in Fig. 1-1. This is the simplest structure of absorbers, which is called metal-backed single-layer model. In this case, to achieve low reflection, two problems need to be resolved. The first matter is how to allow the incident EM wave penetrating into the material with the lowest reflection and the other is how to absorb the EM wave with the maximum amount. To resolve the first problem, the impedance match between the material and free space is needed, *i.e.* $\sqrt{\mu/\varepsilon}$ =1, where μ and ε are the complex permeability and permittivity of the absorbing material, respectively. Unfortunately, for most of EM materials, μ' is generally much smaller than ε' at microwave frequency. Thus, it is necessary to increase μ' and decrease ε' to satisfy the impedance match. In the second problem,

the applied material should have large imaginary part of permittivity ε" or permeability μ" at microwave frequency to significantly absorb the incident EM wave. Therefore, EM materials with excellent absorbing ability should have high permeability μ' , small permittivity ε' , and large magnetic or dielectric loss at microwave frequency.

In considerations of practical applications, there are also some other requirements for EM absorbing materials, such as low density, small thickness, high mechanical strength and good chemically stability.

1.2 Candidates for filler of composites

In general, microwave absorbing materials consist of dielectric or magnetic filler and polymer. In the past, lossy dielectric materials have been used for absorbing EM wave due to the low density and perfect temperature stability.[1, 2, 3] Common dielectric materials used for absorption are carbon, graphite and metal flakes, *etc.*.[4, 5] However, they are usually too bulky for convenient operation. For example, in order to obtain a same absorbing performance as magnetic materials, the effective thickness of dielectric materials would be over 12 cm, while the thickness for magnetic materials is only about 0.2 cm.[6, 7] Therefore, in recent years, magnetic absorbing materials have attracted considerable attention.

Ferrites and metallic alloys are two most important magnetic fillers for use as EM absorbing materials. Some fundamental properties of ferrites and metallic magnetic materials are listed in Table 1-1. Metal materials usually have large saturation magnetization and high complex permeability ($\mu = \mu' - j\mu''$). Therefore, it is possible to make thin absorbers using metallic magnetic materials.[8, 9] Among the metallic

magnetic powders, Fe-Si-Al alloy, carbonyl iron, Fe, Co or Ni and their permalloys have been widely studied as absorbing materials.[10, 11, 12, 13] However, there are still some serious drawbacks when metallic magnetic materials are used for EM absorption. The electric conductivity of these materials is generally high, and resonance frequency is very low.[14] Due to the eddy current loss, the permeability decreases rapidly at high frequency.[15] In addition, the permittivity is very large, thus it is difficult to satisfy impedance match between the material and free space. Therefore, general metallic magnetic materials are also not suitable candidates for microwave absorption.

Table 1-1. Properties for ferrites and metallic magnetic materials. μ_i is the initial permeability, ε is the absolute value of permittivity, f_r is the resonance frequency, ρ is the resistivity and T_c is the Curie temperature.

	μ_i	ε	f_r (Hz)	ρ (Ω·cm)	Density (g/cm^3)	Chemical Stability	T_c (K)
Metal	10^3-10^5	>100	$<10^3$	$<10^{-2}$	~7.8	Oxidation	>1000
Ferrite	10-10^4	~14	10^6-10^{10}	10^2-10^{10}	~5.0	Excellent	~700

As compared with metals, ferrites have many important characteristics, such as low permittivity, high resonance frequency, high resistivity, low density and good chemical stability, which are just required for microwave absorbing materials. Especially, in multilayer EM materials, ferrites play an irreplaceable role as matching layers between EM material and free space due to their good impedance matching property. However, as compared with the dielectric materials, the main drawbacks of ferrites are their high density and relatively poor temperature stability, which need to be improved.

According to the crystal structure, ferrites can be divided into three main groups: spinel, garnet and hexaferrite.[16] The properties and applications of these ferrites have been summarized by Li *et al.*[17] and are listed in Table 1-2. Most of spinel ferrites have relatively high initial permeability and have been extensively applied to electrical and electronic technology. However, because of the Snoek limits,[18] the resonance frequency is low (not higher than a few hundred megahertz (MHz)), thus the permeability of the Spinel ferrites decreases to about 1 in the microwave band. Garnet ferrites have high gyro-magnetic property, very low magnetic and dielectric loss. Hence, they are very useful in nonreciprocal devices. However, the resonance frequency is even lower than that of spinel ferrites. Therefore, both spinel and garnet ferrites are not suitable for use as EM materials at microwave frequency.

Table 1-2. Fundamental properties of three groups of ferrite materials. μ_i is the initial permeability, f_r is the resonance frequency and ρ is the resistivity.[17]

Ferrite		μ_i	f_r	ρ (Ω·cm)	Applications
Spinel	MnZn	10^4	<1 MHz	10^2	Electric and electronic industry; EM absorbing materials
	NiZn	10^2-10^3	<300 MHz	10^6-10^8	
Garnet	YIG	10^2	1-100 MHz	10^{10}	Microwave device
Barium Hexaferrite		20-40	1-80 GHz	~10^6	Magnetic recording materials; Microwave device; EM materials

Hexaferrites have significantly large crystalline anisotropy due to their low crystal symmetry, as compared with the cubic symmetry of spinel or garnet ferrites. Therefore, the resonance frequency can reach as high as 100 GHz.[19] Furthermore, the location of resonance can be modified over a wide frequency range by the substitution of ions in hexaferrites.[20] In addition, hexaferrites with *c*-plane anisotropy are soft

magnetic materials with relatively large permeability. Therefore, hexaferrites are promising candidates for the development of microwave absorbing materials.

1.3 Objective of this study

Barium hexaferrite is one of the typical hexagonal ferrites. In the barium-ferrite family, *W*-type ferrites have the highest saturation magnetization and relatively high Curie temperature, while most of *Y*-type ferrites have *c*-plane anisotropy. It is well known that high saturation magnetization and *c*-plane anisotropy are necessary for an excellent microwave absorbing material, and high Curie temperature is important for any magnetic material. Hence, these two kinds of ferrite are promising for the development of microwave absorbing materials.

As we know, microwave frequency bands cover a frequency range from 3 MHz to 300 GHz, but the greatest number of operational radar waves fall within 1-18 GHz. Hence, the magnetic resonance frequency for studied ferrites should be controlled as several GHz. On the other hand, for an ideal EM absorbing material, the reflectivity should remain as small as possible over as wide a frequency range as possible. Therefore, this study will focus on controlling the resonance frequency and enhancing the absorbing performance in BaW and BaY hexaferrites. The main objectives are summarized as follows.

a. Fabricate pure *W*- and *Y*-type barium hexaferrites using solid-state reaction and examine some important properties, such as static and dynamic magnetic property, with various measurement methods.

b. Explore the possibility of improving the high-frequency magnetic and absorbing properties with ions substitution and oxides doping.

c. Investigate the influence of ferrite concentration in composites on the

microwave absorbing performance.

d. Investigate and understand the physical mechanisms of magnetic resonance and microwave absorption.

e. Obtain EM materials with low reflectivity and broad bandwidth at microwave frequency.

The thesis is organized as follows.

Firstly, a brief introduction about this study, including background information and our motivations, is given in Chapter 1. This is followed by Chapter 2, which presents a systematical review about the basic understanding of barium hexaferrites, theories of high-frequency magnetic property and previous investigations on hexaferrites for microwave applications.

During this research, various measurements are required for the evaluation of ferrites properties, such as static and dynamic magnetic properties. Therefore, before the engagement of this investigation, Chapter 3 will be preceded with the introduction of experimental techniques used in this work, including the samples fabrication, characterization techniques and data analysis methods.

Based on the review on previous investigations in Chapter 2, it can be confirmed that ions substitution, especially Co^{2+} substitution, is an effective method to control magnetic resonance frequency for ferrites. Meanwhile, it is well known that suitable ions substitution in ferrites, such as Zn^{2+}, can improve the static magnetic property. Therefore, in this study, ions substitution will be investigated to control the absorbing frequency and enhance the absorbing property. Chapter 4 and Chapter 7 will systematically report the effect of ions substitution on microstructure, static magnetic,

electromagnetic and microwave absorbing properties for *W*- and *Y*-type ferrites, respectively.

The composites consist of ferrite powders and epoxy resin. Therefore, the volume concentration of ferrite will have strong influence on the properties of composites. In Chapter 5, the influence of ferrite concentration on complex permittivity, permeability and absorbing properties will be studied.

In addition to ions substitution, oxides doping is another effective method to control static and dynamic magnetic properties of ferrites by the modification of microstructure. Therefore, in Chapter 6, BaW doped with V_2O_5 will be investigated. The effect of various amount V_2O_5 doping (varying from 0-1.5 wt%) in $BaCoZnFe_{16}O_{27}$ and 1.0 wt% V_2O_5 doping in $BaCo_xZn_{2-x}Fe_{16}O_{27}$ (x=1.3 and 1.5) will be explored in detail.

Finally, the thesis is completed with two appendices. In Appendix A, the investigation on 1.0 wt% of various oxides (from divalent to pentavalent) doping in $BaCoZnFe_{16}O_{27}$ will be reported and analyzed. Some tables from Chapter 7 are listed in Appendix B.

It is hoped that this study should provide some useful information of hexaferrites for microwave absorbing application. On the one hand, the microwave absorbing performance of *W*- and *Y*-type hexaferrites, including absorbing frequency and absorbing ability, may be effectively modified by ion substitution and oxide doping. Some physical understanding on these variations would be addressed. On the other hand, with the investigation of composites with various ferrite concentrations, a suitable ferrite concentration for composites may be obtained.

CHAPTER 2: LITERATURE REVIEW

2.1 Basic knowledge of hexaferrites

Most of the hexaferrites have been developed over the past several decades. Their crystal structure and magnetic properties have been studied in detail. This section will devote to describe the basic knowledge of hexaferrites, including chemical composition, crystal structure and static magnetic properties.

2.1.1 Composition and crystal structure

The chemical compositions of the hexagonal compounds are shown in Fig. 2-1 as part of a ternary phase diagram and in Table 2-1 for the BaO-MeO-Fe_2O_3 system. It is evident that hexaferrites include a large amount of different compounds and have many types, including $BaFe_{12}O_{19}$ (*M*-type, BaM), $BaMe_2Fe_{16}O_{27}$ (*W*-type, BaW), $Ba_2Me_2Fe_{12}O_{22}$ (*Y*-type, BaY), $Ba_3Me_2Fe_{24}O_{41}$ (*Z*-type, BaZ), $Ba_2Me_2Fe_{28}O_{46}$ (*X*-type, BaX) and $Ba_4Me_2Fe_{36}O_{60}$ (*U*-type, BaU). Here, Me represents a divalent ion, such as Fe^{2+}, Co^{2+}, Ni^{2+}, Cu^{2+} and Zn^{2+}, or a combination of them. In addition, S and T are constituent blocks of the hexagonal compounds, which will be explained in detail later, while B was reported as an antiferromagnetic hexagonal compound[21] with composition of $BaFe_2O_4$ and, here, it is an intermediate phase for preparation of BaM from Fe_2O_3 and BaO.

Table 2-1 also lists the crystallographic building for each type of hexaferrites. R ($BaFe_6O_{11}$), S (Fe_6O_8 or $Me_2Fe_4O_8$) and T ($Ba_2Fe_8O_{14}$) are the building blocks of the crystal. R*, S* and T* indicate the blocks obtained by rotating R, S and T through

180 ˚ around the vertical axis, respectively.

Figure 2-2 shows the perspective drawing of blocks R, S and T separately. All of them have a close-packed arrangement of O atoms. Ba^{2+} is located in oxygen layer to replace O^{2-}. Fe ion occupies the interstitial positions of the oxygen lattice. Me ion also locates at the interstitial positions of the oxygen lattice by replacing Fe. The S unit is formed by two formula units Fe_3O_4 with the spinel structure thus containing two tetrahedral and four octahedral cation sites. The R block has the stoichiometry $BaFe_6O_{11}$, with five octahedral sites of two different types and one trigonal bipyramidal site. The T unit has four layers with formula $Ba_2Fe_8O_{14}$, where Fe ions occupy two tetrahedral sites, and six octahedral sites of two different types. The block lengths are 4.81 Å, 11.61 Å and 14.52 Å for the S, RS and TS blocks, respectively.[22] The crystal for any type of hexaferrite is built up by the superposition of these blocks along the vertical axis, which is characterized as *c*-axis.

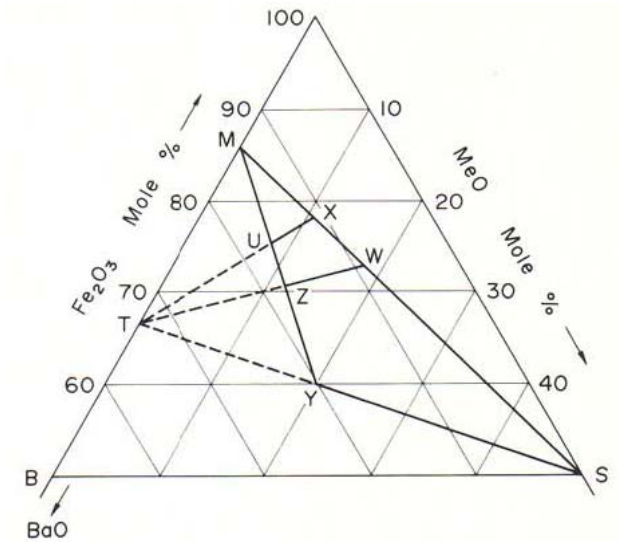

Fig. 2-1. The relationships of chemical compositions among barium hexaferrites.[23]

Table 2-1. Chemical composition and crystallographic building for hexaferrites.[24]

Type	Chemical formula	Abbreviation	No. of molecules per unit cell	Crystallographic building per unit cell
M	$BaFe_{12}O_{19}$	BaM	2	RSR*S*
W	$BaMe_2Fe_{16}O_{27}$	BaW or Me_2W	2	RSSR*S*S*
Y	$Ba_2Me_2Fe_{12}O_{22}$	BaY or Me_2Y	3	3(ST)
Z	$Ba_3Me_2Fe_{24}O_{41}$	BaZ or Me_2Z	2	RSTSR*S*T*S*
X	$Ba_2Me_2Fe_{28}O_{46}$	BaX or Me_2X	3	3(RSR*S*S*)
U	$Ba_4Me_2Fe_{36}O_{60}$	BaU or Me_2U	1	RSR*S*T*S*

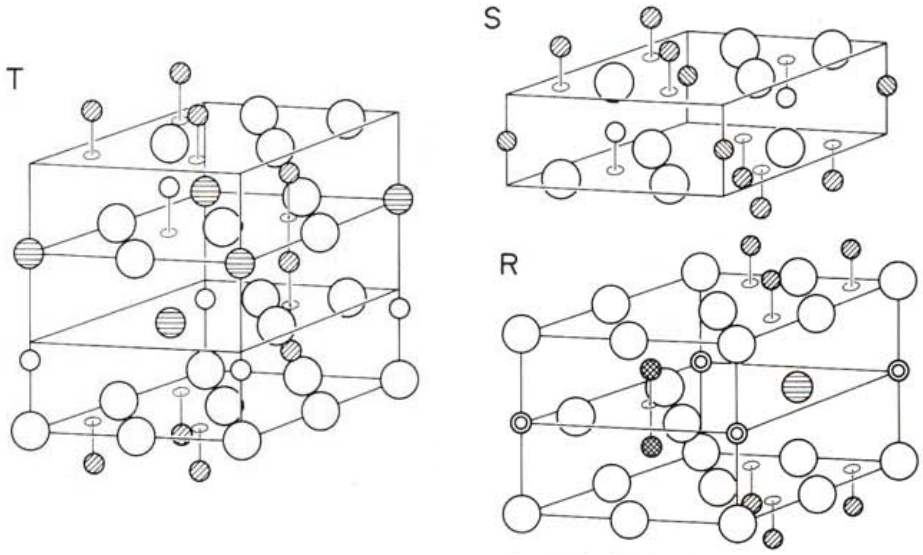

Fig. 2-2. Perspective drawings of building blocks S, R and T in the hexagonal compounds (The big white ball, middle hatched ball and small ball represent O^{2-}, Ba^{2+} and Fe^{3+} ions, respectively).[25]

Among all types of hexaferrite, *M*-type ferrite has the simplest crystal structure. As shown in Fig. 2-3, the unit cell of BaM, which is built up by superposition of two S-blocks and two R-blocks, is expressed as RSR*S* and contains ten close-packed oxygen planes. Five oxygen planes make one molecule and two molecules make one unit cell. Fe^{3+} ions occupy five different sublattices of 12k, $4f_{VI}$, 2a, $4f_{IV}$ and 2b. Here,

the symbols of k, f_{VI}, a, f_{IV} and b are Wyckoff's notations and the numbers represent the amount of positions. The space group of the compound is denoted as $P6_3/mmc$. The lattice parameters of *a* and *c* have been reported as 0.588 nm and 2.32 nm, respectively.[26]

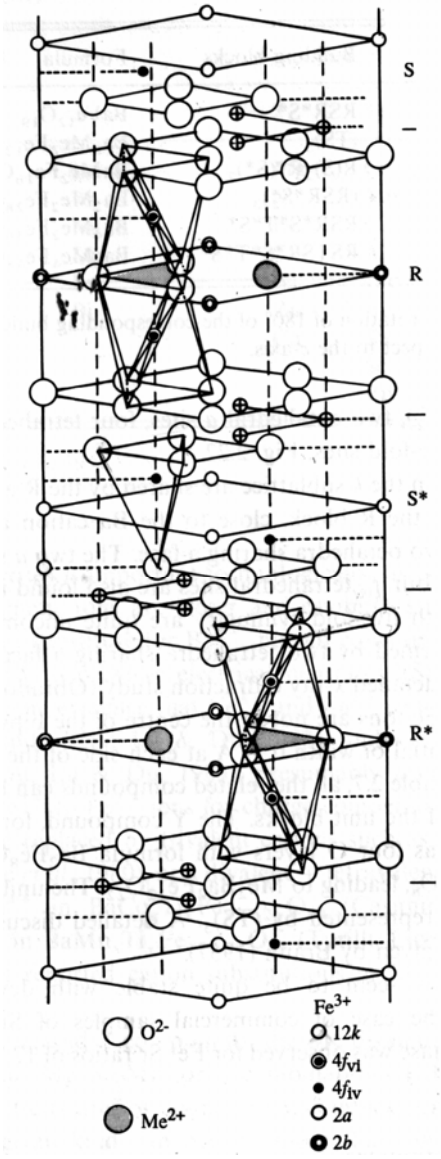

Fig. 2-3. Unit cell of $BaFe_{12}O_{19}$.[27]

The unit cell of *W*-type ferrite is built up by superposition of four S-blocks and two R-blocks. Fig. 2-4 shows a cross section of the *W*-structure having a hexagonal packing,

which is closely related to the *M*-structure. The only difference is that the successive R-blocks are interspaced by two S-blocks instead of one, as the case in the *M*-structure. The cations of Me^{2+} and Fe^{3+} occupy seven different sublattices of 12k, 4e, $4f_{IV}$, $4f_{VI}$, 6g, 4f and 2d.

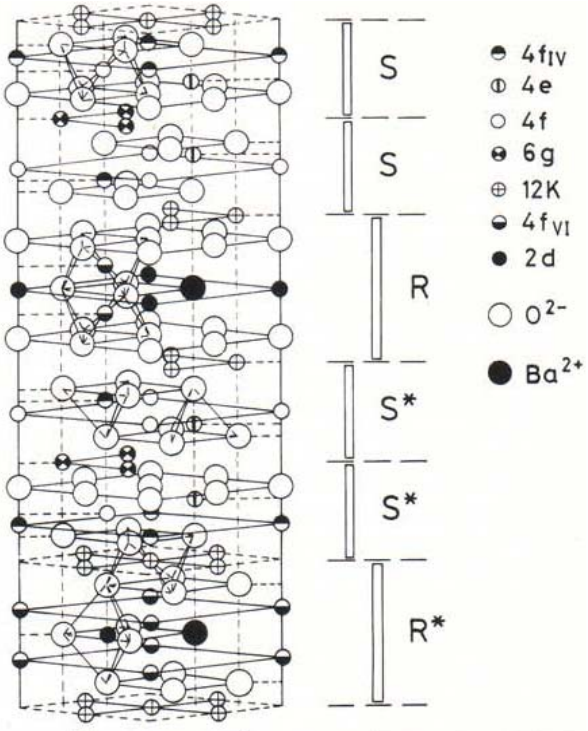

Fig. 2-4. Unit cell of the $BaMe_2Fe_{16}O_{27}$.[28]

The unit cell of *Y*-type compound is built up by the superposition of three S-blocks and three T-blocks, as shown in Fig. 2-5, in which the difference lattice sites are also distinguished by different symbols. There are six different sublattices for cations, including $3a_{VI}$, $6c_{VI}$, $3b_{VI}$, $18h_{VI}$, $6c_{IV}$ and $6c_{IV}$*. Here, sublattices having the same crystalline symmetry but belonging to different blocks are marked by an asterisk.

The crystalline structure of BaZ is more complicated. The unit cell is formed by the

superposition of four S-blocks, two T-blocks and two R-blocks, and the divalent and trivalent cations are distributed among ten different lattice sites. Fig. 2-6 shows a cross section of the *Z*-structure.

In addition, the unit cell of *X*-type ferrite consists of four alternate layers of the *M*-structure and *W*-structure, and the unit cell of the *U*-type ferrite is built up by the superposition of two *M*-blocks and one *Y*-block along the *c*-axis. Both structures belong to the space symmetry group $R\bar{3}m$.

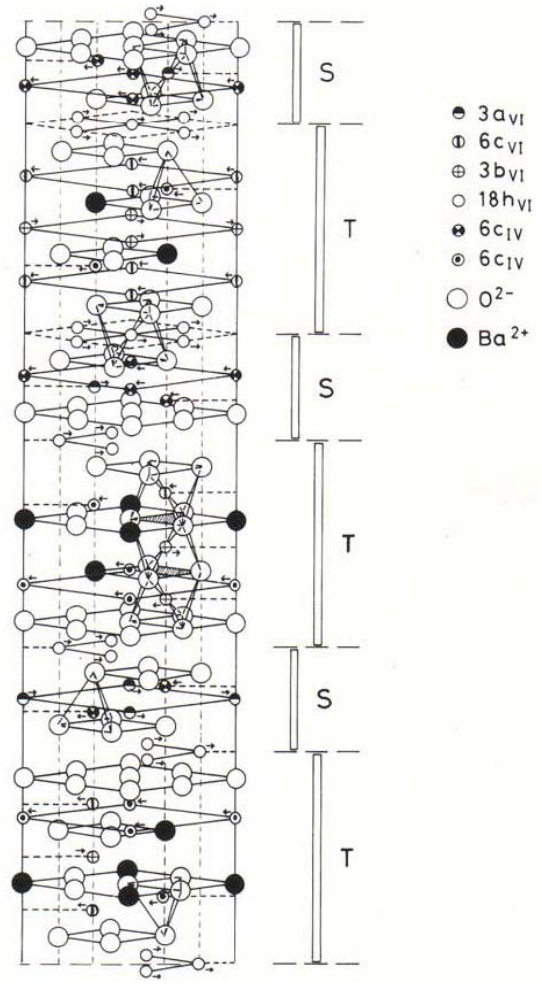

Fig. 2-5. Unit cell of the $Ba_2Me_2Fe_{12}O_{22}$.[29]

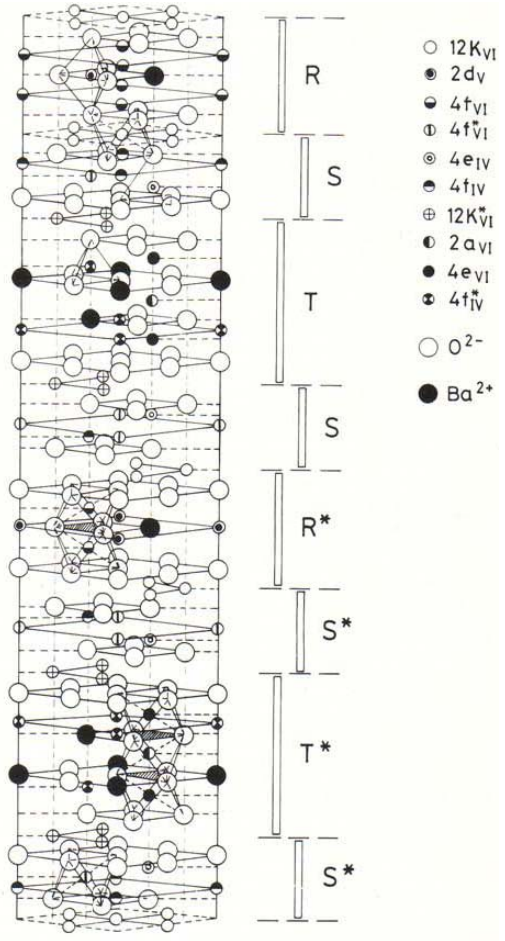

Fig. 2-6. Unit cell of the $Ba_3Co_2Fe_{24}O_{41}$.[30]

2.1.2 Magnetic ordering

The spins in some materials have a spontaneous alignment in a zero field. Such materials are known as the magnetic ordering materials. Due to the competition of thermal and exchange energies, the spontaneous magnetization will disappear at certain temperature, which is known as Curie or Neel temperature (T_c). The Heisenberg exchange interaction,

$$H = -2\sum_{i<j} g_{ij} S_i \cdot S_j , \qquad 2\text{-}1$$

is used to describe the ordering of neighboring localized magnetic moments. Here, g is the exchange parameter and S_i is the spin quantum number of atom i. A positive g favors parallel alignment (ferromagnetic order) and a negative g favors antiparallel alignment (antiferromagentic order). When two antiferromagnetically coupled sublattices in materials have unequal moments, the net moment is not zero. Such materials are called ferrimagnetic materials. Hexaferrite is a typical ferrimagnetic material.

It has been described that, in hexaferrite structures, cations (Fe^{3+} and Me^{2+}) are located at the interstitial positions of the oxygen lattice. Thus, these ions are mutually separated by oxygen ions. In this case, a direct exchange interaction between the cation orbitals is excluded. Therefore, some form of mediated or indirect exchange interaction must be considered. A model proposed by Neel and formulated in detail by Anderson[31] described the exchange interaction between the 3*d* electrons of magnetic ions through the 2*p* electrons of oxygen ions. This interaction is known as super-exchange interaction, which distinguishes with the direct exchange interaction in metals and alloys.

A simple picture that adequately describes super-exchange is shown in Fig. 2-7. Two transition metal ions (T) are separated by an oxygen ion. The *p* orbital of oxygen ion, which is filled in the ground state, can exchange an electron with each of the adjacent 3*d* orbitals. Thus, the bonding is mostly ionic. The positive and negative phase parts of the wave function for each orbital are represented by solid and dashed lines, respectively. The doubly occupied p_x orbital has two electrons of opposite spin. When an electron is exchanged or shared by the overlapping orbitals between two sites, the spin is conserved as the electron hops from the *p*-like to the *d*-like orbital. The result

is that the two T ions must have opposite spin directions. A simpler electronic state picture is shown in the lower part of Fig. 2-7.

Generally, apart from the electronic structure of magnetic ions, super-exchange interaction strongly depends on the geometry of arrangement of the two interacting ions and the intervening oxygen ion. Both the distance and the angles are relevant. The interaction is greatest for an angle of 180 º and vanished for 90 º. Usually, only the interactions within the first coordination sphere (both cations in contact with the anion) are supposed to be of importance and the others are often disregarded.

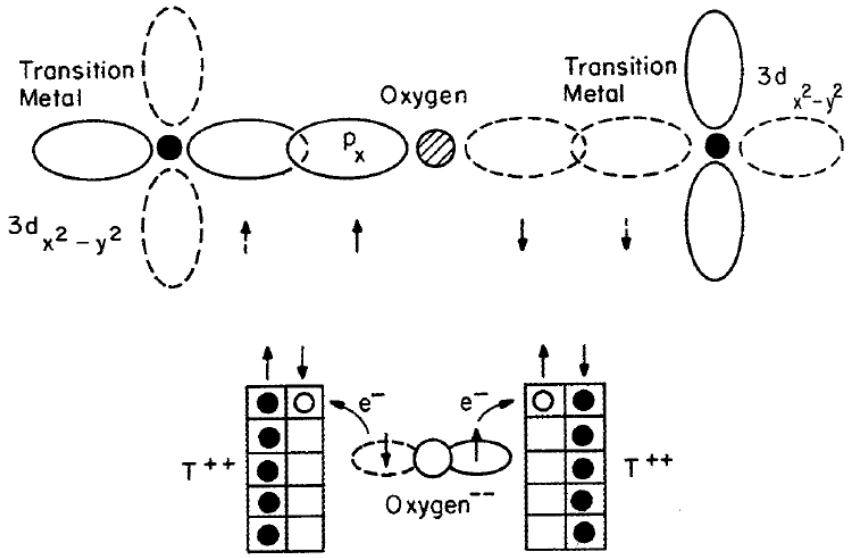

Fig. 2-7. Schematic of *d* and *p* orbitals important to the super-exchange interaction.[32]

In *M*-type hexaferrite structure, there are five sublattices that iron ions could occupy. The five sublattices fall into three types of coordinations, namely, octahedral sites, tetrahedral sites and trigonal bipyramidal sites, as listed in Table 2-2. Here, the arrow represents the orientation of the magnetic moments of each cation as a result of super-exchange interaction. S block contains four Fe^{3+} ions of spin-up in octahedral sites

and two Fe^{3+} ions of spin-down in tetrahedral sites; while in R block, there are three Fe^{3+} ions of spin-up in octahedral sites, two Fe^{3+} ions of spin-down in octahedral sites and one Fe^{3+} ion of spin-up in trigonal bipyramidal site. Because Fe^{3+} has the magnetic moment of 5 μ_B at 0 K, the total magnetization per unit formula can be calculated as

$$M_s \text{ (0 K)} = 5\times(6\text{-}2\text{+}1\text{-}2\text{+}1) = 20\ \mu_B.$$

This value agrees very well with the experimental results of 20.6 μ_B and 19.3 μ_B.[33]

Table 2-2. Coordination number and direction of magnetic moment of Fe^{3+} ions in the unit cell of the *M*-type hexaferrite.[34]

Coordination	Wyckoff's notation	Number of positions	Spin direction
Octahedral	k f_{VI} a	12 4 2	↑ ↓ ↑
Tetrahedral	f_{IV}	4	↓
Trigonal bipyramidal	b	2	↑

Table 2-3 lists the number of ions, spin orientation and coordination of the different cation sublattices in the *W*-, *Y*- and *Z*-type hexaferrites. Different from *M*-type, these compounds contain divalent cation, which can be Co^{2+}, Zn^{2+}, Ni^{2+}, Fe^{2+}, Cu^{2+}, Mg^{2+} or Mn^{2+}, or a combination of them. Hence, the static magnetic properties, such as saturation magnetization and Curie temperature, can be greatly changed by the substitution of various kinds of metal ions and the distribution of these ions. The special saturation magnetization at temperature of absolute zero and 293 K, and the Curie temperature T_c for some hexagonal ferrites reported by various authors are collected in Table 2-4. It is evident that *W*-type ferrites (BaW) have the highest

saturation magnetization and relatively high Curie temperature in the hexaferrites family. As a result, this kind of ferrites has been of the research interest for decades.

Table 2-3. Number of ions, coordination and spin orientation for the various cations of *W*-,[28] *Y*-[29] and *Z*-type[30] structures. Sublattices having the same crystalline symmetry but belonging to different blocks are marked by an asterisk.

Type of structure	Sublattice	Coordination	Number of positions	Block	Spin
W-type	12K	Octahedral	12	R-S	↑
	4e	Tetrahedral	4	S	↓
	$4f_{IV}$	Tetrahedral	4	S	↓
	$4f_{VI}$	Octahedral	4	R	↓
	6g	Octahedral	6	S-S	↑
	4f	Octahedral	4	S	↑
	2d	Hexahedral	2	R	↑
Y-type	$6c_{IV}$	Tetrahedral	6	S	↓
	$3a_{VI}$	Octahedral	3	S	↑
	$18h_{VI}$	Octahedral	18	S-T	↑
	$6c_{VI}$	Octahedral	6	T	↓
	$6c_{IV}$*	Tetrahedral	6	T	↓
	$3b_{VI}$	Octahedral	3	T	↑
Z-type	$12k_{VI}$	Octahedral	12	R-S	↑
	$2d_{V}$	Five-fold	2	R	↑
	$4f_{VI}$	Octahedral	4	R	↓
	$4f_{VI}$*	Octahedral	4	S	↑
	$4e_{IV}$	Tetrahedral	4	S	↓
	$4f_{IV}$	Tetrahedral	4	S	↓
	$12k_{VI}$*	Octahedral	12	T-S	↑
	$2a_{VI}$	Octahedral	2	T	↑
	$4e_{VI}$	Octahedral	4	T	↓
	$4f_{IV}$*	Tetrahedral	4	T	↓

Table 2-4. The saturation magnetization per gram M_s at absolute zero and 293 K, and the Curie temperature T_c for hexagonal ferrites.[35]

Structure Type	Composition	M_s (0 K) (emu/g)	M_s (293 K) (emu/g)	T_c (˚C)
BaM	$BaFe_{12}O_{19}$	100	68	470
BaW	$BaMn_2Fe_{16}O_{27}$	97	59	415
	$BaFe_2Fe_{16}O_{27}$	98	78	455
	$BaNiFeFe_{16}O_{27}$	79	52	520
	$BaZnFeFe_{16}O_{27}$	108	73	430
BaY	$Ba_2Mn_2Fe_{12}O_{22}$	42	31	290
	$Ba_2Co_2Fe_{12}O_{22}$	39	34	340
	$Ba_2Ni_2Fe_{12}O_{22}$	25	24	390
	$Ba_2Zn_2Fe_{12}O_{22}$	72	42	130
	$Ba_2Mg_2Fe_{12}O_{22}$	29	23	280
BaZ	$Ba_3Co_2Fe_{24}O_{41}$	69	50	410
	$Ba_3Cu_2Fe_{24}O_{41}$	60	46	440
	$Ba_3Zn_2Fe_{24}O_{41}$	55	58	360

2.1.3 Magnetocrystalline anisotropy

The preference of the magnetization lying in a particular direction is called magnetic anisotropy. Magnetic anisotropy can have its origin in sample shape, crystal symmetry, stress or directed atomic pair ordering. Attention is focused here on magnetocrystalline anisotropy, which is an intrinsic property of a magnet.

The physical origin of magnetocrystalline anisotropy is based on two necessary effects, a low symmetry crystal field and a nonzero spin-orbit interaction. If the atomic orbital has zero angular moment ($L_Z = 0$), such as Fe^{3+} and Mn^{2+}, it does not

matter what the symmetry of the crystal field is; the orbital can take on any orientation with respect to the crystal. If the orbitals have nonzero $<L_Z>$, such as Co^{2+} and Fe^{2+}, they may assume any orientation in a spherically symmetric crystal field, while only certain orientations will be preferred in crystal fields of lower symmetry. Therefore, Co^{2+} and Fe^{2+} ions have more contribution to magnetocrystalline anisotropy than Fe^{3+} and Mn^{2+} due to the nonzero orbital angular moment. In addition, hexaferrites have lower crystal symmetry than spinel ferrites, thus the former have stronger anisotropy.

According to the easy magnetization directions, barium hexaferrites can be divided into two types, *c*-axis and *c*-plane anisotropies, as shown in Fig. 2-8. They are associated with the easy magnetization along *c*-axis and in *c*-plane, respectively. For *c*-axis anisotropy, the magnetic field required for rotation of magnetization vectors from $[0001]$ to $[000\bar{1}]$ direction is defined as the anisotropy field H_a. On the other hand, for *c*-plane anisotropy, there are six easy magnetization directions separated by angles of 60 º from each other in the *c*-plane. They lie along the crystallographic directions of $[10\bar{1}0]$, $[\bar{1}100]$ and $[0\bar{1}10]$. When a magnetic field is applied, the magnetization vectors can be rotated from one easy magnetization direction to another by going through the *c*-axis or rotating in the *c*-plane. The corresponding magnetic fields required are defined as out-of-plane anisotropy field H_θ and in-plane anisotropy field H_ϕ, respectively.

The energy required to rotate the magnetization from the easy direction to another direction is called magnetocrystalline anisotropy energy, which can be expressed in terms of certain anisotropy constants and the direction to which the magnetization is

rotated. When the direction of the spontaneous magnetization in a hexagonal crystal is expressed by polar coordinates, θ and ϕ with respect to the crystal axis, assuming the *z*-axis is along the hexagonal *c*-axis, then the magntocrystalline energy *E* is given by

$$E = K_1 \sin^2\theta + K_2 \sin^4\theta + K_3 \sin^6\theta \cos 6\phi + ..., \qquad 2\text{-}2$$

where K_1, K_2 and K_3… are the first, second and third…order magnetocrystalline anisotropy constants, respectively.

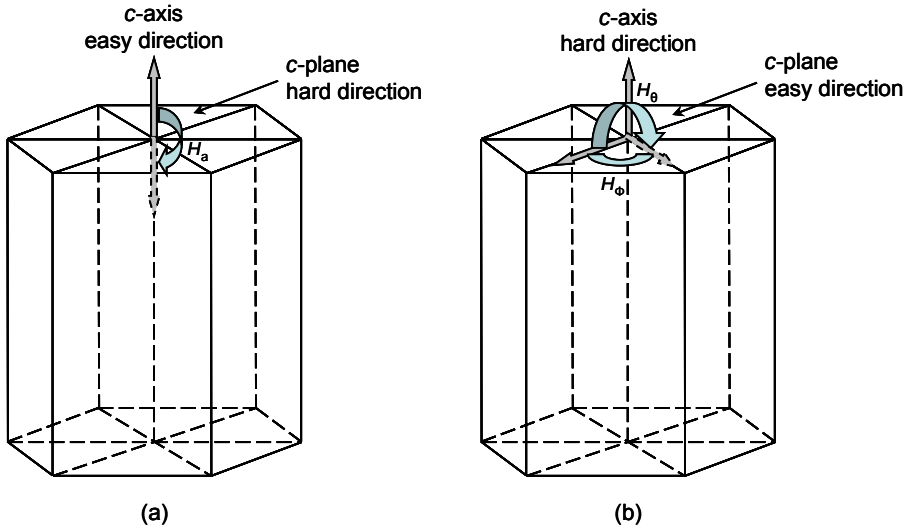

Fig. 2-8. Two types of the anisotropy for barium ferrites, (a) *c*-axis, and (b) *c*-plane anisotropies.

For *c*-axis anisotropy, $K_1 > 0$ and normally, K_2, K_3,… are negligible in comparison with K_1. In this case, the magnetocrystalline anisotropy field H_a is given by

$$H_a = \frac{2K_1}{M_s}. \qquad 2\text{-}3$$

On the other hand, for *c*-plane anisotropy, $K_1 + 2K_2 < 0$, and the anisotropy field H_θ

and H_ϕ can be expressed as

$$H_\theta = -\frac{2(K_1 + 2K_2)}{M_s} \text{ and} \qquad 2\text{-}4$$

$$H_\phi = \frac{36K_3}{M_s}, \qquad 2\text{-}5$$

respectively. Therefore, the value of anisotropy filed can be easily estimated from the data of anisotropy constants and saturation magnetization.

In the barium family, most of *Y*-type ferrites have *c*-plane anisotropy, while most of the other types have *c*-axis anisotropy. It is because there is no R-block in the *Y*-type structure, which consists of alternate stacking of S- and T-blocks. It has been introduced that, in the R-block, there exists a trigonal bipyramidal site, which is named as the 2b site for *M*-ferrite and the 2d site for *W*- and *Z*-ferrites. The large magnetocrystalline anisotropy of these three types of ferrites was explained by Smit from the effect of Fe^{3+} in the trigonal bipyramidal site, where a ferric ion is surrounded by five oxygen ions.[36] Fuchikami also theoretically showed the contribution of Fe^{3+} in the trigonal site as principally responsible for the uniaxial anisotropy.[37]

One of the important characteristics for hexaferrites is that the crystalline anisotropy can be changed over a large range of values by the substitution of the transition metal ions for other divalent ions. It has been confirmed that Co^{2+} has strong contribution to planar anisotropy due to its negative contribution to the first order magnetocrystalline anisotropy constant K_1.[30] On the other hand, other metallic ions, such as Zn^{2+}, Ni^{2+}, Fe^{2+} and Fe^{3+}, lead to *c*-axis anisotropy. Therefore, the substitution of Co ions should

be able to modify the anisotropy from *c*-axis to *c*-plane for *M*-, *W*- and *Z*-ferrites, and increase the *c*-plane anisotropy for *Y*-ferrite.[38, 39, 40]

2.2 Theories of high-frequency magnetic property

2.2.1 Permeability

For high-frequency applications, the most important property of magnetic materials is permeability. The initial permeability μ is defined as the derivative of the induction $\vec{B}$ with respect to the internal field $\vec{H}$ in the demagnetized state:

$$\mu = \frac{d\vec{B}}{d\vec{H}} \qquad \text{with } H \to 0 \text{ and } B \to 0. \tag{2-6}$$

At microwave frequencies, and also in anisotropic crystals, $d\vec{B}$ and $d\vec{H}$ may be in different directions; the permeability then has tensor character. In the case of polycrystalline materials containing a large number of randomly oriented crystallites, the permeability will be a scalar.

The magnetic energy density *E* is given by

$$E = \frac{1}{4\pi}\int \vec{H} \cdot d\vec{B}. \tag{2-7}$$

For a time-harmonic field $H = H\sin\omega t$, the dissipation can be described by a phase difference δ between $\vec{H}$ and $\vec{B}$. In this case, the permeability concept may be extended to include the losses. Therefore, we first introduce the quantity $\hat{\mu} = \hat{B} \big/ \hat{H}$ as the ratio of the amplitudes of $\vec{B}$ and $\vec{H}$,

$$B = \hat{B}\sin(\omega t - \delta) = \hat{\mu}\,\hat{H}\cos\delta\sin\omega t - \hat{\mu}\,\hat{H}\sin\delta\cos\omega t. \tag{2-8}$$

The component $\hat{\mu}\hat{H}\cos\delta$, which is in phase with $\vec{H}$, is related to the maximum stored magnetic energy density *E*',

$$E' = \frac{1}{8\pi}\hat{\mu}\hat{H}^2\cos\delta. \qquad 2\text{-}9$$

The component $\hat{\mu}\hat{H}\sin\delta$ is 90º out of phase with $\vec{H}$. This component is a measure for the losses. In the steady state, the losses can be found by integrating Eq. 2-7 over one period $T = 2\pi/\omega$. The energy dissipation *P* per unit volume and time is therefore

$$P = \frac{1}{4\pi}\frac{1}{T}\int_0^T H\frac{dB}{dt}dt = \frac{\omega}{8\pi}\hat{\mu}\hat{H}^2\sin\delta. \qquad 2\text{-}10$$

In the complex notation with the time factor $\exp(j\omega t)$, we can write Eq. 2-8 as $B = \mu H$ by introducing the complex permeability

$$\mu = \mu' - j\mu'' = \hat{\mu}\cos\delta - j\hat{\mu}\sin\delta, \qquad 2\text{-}11$$

from which it follows that $\hat{\mu} = |\mu|$. The real part μ' describes the stored energy and the imaginary part μ'' describes the dissipation. The behavior of μ' and μ'' versus frequency is called a permeability spectrum.

2.2.2 Ferromagnetic resonance and natural resonance

The basic theory of the dynamic response of ferromagnetic materials was originally developed by Landau and Lifshitz in 1935.[41] As shown in Fig. 2-9, the precession of magnetization vector $\vec{M}$ under an effect magnetic field $\vec{H}_{eff}$ is given by

$$\frac{d\vec{M}}{dt} = -\gamma \vec{M} \times \vec{H}_{eff} - \frac{\lambda}{M^2} \vec{M} \times (\vec{M} \times \vec{H}_{eff}), \qquad 2\text{-}12$$

where γ is the gyromagnetic ratio and λ is the damping coefficient. $\vec{M}$ and $\vec{H}_{eff}$ can be expressed by

$$\vec{M} = \begin{pmatrix} m_x \\ m_y \\ M_0 + m_z \end{pmatrix} \qquad 2\text{-}13$$

and

$$\vec{H}_{eff} = \begin{pmatrix} h_{ex} - N_x m_x \\ h_{ey} - N_y m_y \\ H_e + h_{ez} - N_z (M_0 + m_z) \end{pmatrix}, \qquad 2\text{-}14$$

respectively. Here, h_e is *ac* field and m is *ac* magnetization. H_e is *dc* field, which is contributed by the applied field H_0 and anisotropy field H_a. M_0 is *dc* magnetization. The directions of $\vec{H}_e$ and $\vec{M}_0$ are along the *z*-axis.

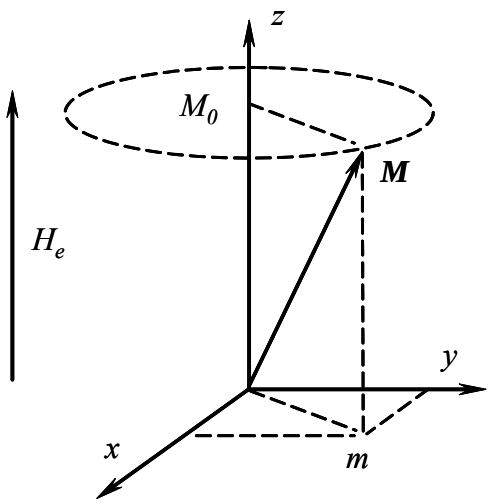

Fig. 2-9. The precession of magnetization vector $\vec{M}$ under an effect field $\vec{H}_{eff}$.

Let h_e and m are both with the time factor $\exp(i\omega t)$. In the case of $|h_e| << H_e$ and $|m| << M_e$, M_0 can be expressed as $M_0 \approx M = M_s$. For a small ellipsoidal particle, we can roughly obtain

$$\vec{m} = \chi^e \cdot \vec{h}_e = \begin{pmatrix} \chi^e_{xx} & -i\chi^e_a & 0 \\ i\chi^e_a & \chi^e_{yy} & 0 \\ 0 & 0 & 0 \end{pmatrix} \cdot \vec{h}_e \qquad 2\text{-}15$$

where

$$\begin{cases} \chi^e_{xx} = \dfrac{\omega_m(\omega_y + i\lambda\omega)}{(\omega_x + i\lambda\omega)(\omega_y + i\lambda\omega) - \omega^2}, \\ \chi^e_{yy} = \dfrac{\omega_m(\omega_x + i\lambda\omega)}{(\omega_x + i\lambda\omega)(\omega_y + i\lambda\omega) - \omega^2}, \\ \chi^e_a = \dfrac{-\omega_m\omega}{(\omega_x + i\lambda\omega)(\omega_y + i\lambda\omega) - \omega^2}, \end{cases} \qquad 2\text{-}16$$

and

$$\begin{cases} \omega_x = \omega_0 + (N_x - N_z)\omega_m, \\ \omega_y = \omega_0 + (N_y - N_z)\omega_m, \\ \omega_0 = \gamma H_e, \\ \omega_m = \gamma M_s. \end{cases} \qquad 2\text{-}17$$

This is the expression of tensor susceptibility for an ellipsoidal particle. Specially, for a spherical grain, the demagnetizing factors of each particle are equal, $N_x = N_y = N_z$, thus Eq. 2-15 becomes

$$\vec{m} = \chi^e \cdot \vec{h}_e = \begin{pmatrix} \chi^e & -i\chi^e_a & 0 \\ i\chi^e_a & \chi^e & 0 \\ 0 & 0 & 0 \end{pmatrix} \cdot \vec{h}_e \qquad 2\text{-}18$$

with

$$\begin{cases} \chi^e = \dfrac{\omega_m(\omega_0 + i\lambda\omega)}{(\omega_0 + i\lambda\omega)^2 - \omega^2}, \\ \chi_a^e = \dfrac{-\omega_m\omega}{(\omega_0 + i\lambda\omega)^2 - \omega^2}. \end{cases} \quad 2\text{-}19$$

For a spherical multi-particle system, the orientation of grains is random and nearly continuous, thus it can be deduced that

$$\vec{m} = \frac{2}{3}\chi^e \vec{h}_e. \quad 2\text{-}20$$

In this case, the permeability (susceptibility) will be scalar and is expressed as

$$\mu = \chi + 1 = \frac{2}{3}\frac{\omega_m(\omega_0 + i\lambda\omega)}{(\omega_0 + i\lambda\omega)^2 - \omega^2} + 1. \quad 2\text{-}21$$

Since $\omega_m = \gamma M_s$, $\omega_0 = \gamma H_e$ and $\omega = 2\pi f$, the above equation can be rewritten as

$$\mu(f) = \frac{\chi_0\left(1 + i\lambda f/f_R\right)}{\left(1 + i\lambda f/f_R\right)^2 - \left(f/f_R\right)^2} + 1 \quad 2\text{-}22$$

where $\chi_0 = \mu_0 - 1 = \frac{2}{3}\frac{M_s}{H_e}$ is the static susceptibility and $f_R = \frac{\gamma H_e}{2\pi}$ is the intrinsic resonance frequency. This expression is usually known as Kittel Equation.[42] Obviously, if $H_0 = 0$, f_R is determined by the anisotropy field. In this case, the phenomenon of magnetization resonance is called natural resonance. In the case of $H_0 \neq 0$, the phenomenon is usually described as ferromagnetic resonance.

2.2.3 Domain wall resonance

In an *ac* magnetic field, $h = h_o e^{i\omega t}$, domain wall will vibrate at the equilibrium position z_o, as shown in Fig. 2-10. Based on the spring model,[43] the moving wall has a kinetic energy proportional to the square of its velocity, $\frac{d^2 z}{dt^2}$, while the effective mass of the wall m_w is expressed as $m_w = \left(c\gamma^2 d\right)^{-1}$, where c is a constant, γ is wall energy per unit area, and d is the wall thickness. Suppose the equilibrium position of the wall is caused by a potential energy $V = 0.5\alpha z^2$, where α is stiffness coefficient. The damping of domain wall movement can be described as $-\beta v$ and β is damping coefficient.

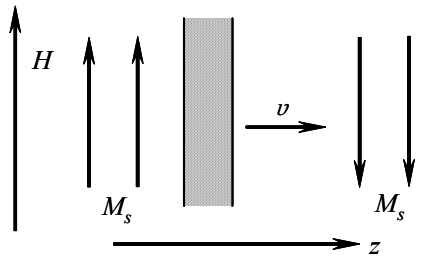

Fig. 2-10. The movement of 180 º domain wall.

Therefore, in CGS units, the movement of the domain wall in an *ac* field is determined as

$$m_w \frac{d^2 z}{dt^2} + \beta \frac{dz}{dt} + \alpha z = 2M_s h = 2M_s h_o e^{i\omega t}. \qquad 2\text{-}23$$

From Eq. 2-23, we get

$$z = z_o e^{i\omega t} = \frac{2M_s h_o}{\alpha + i\omega\beta - \omega^2 m_w} e^{i\omega t}. \qquad 2\text{-}24$$

On the other hand, the change in magnetization *M* due to the wall movement is given by

$$\Delta M = \frac{2M_s z}{l}, \qquad 2\text{-}25$$

where *l* is the length of domain. Then, the wall susceptibility is expressed as

$$\chi(\omega) = \frac{\Delta M}{h} = \frac{2M_s z}{h} = \frac{4M_s^2}{l(\alpha + i\omega\beta - \omega^2 m_w)} = \frac{\chi_o}{1 - \left(\frac{\omega}{\omega_R}\right)^2 + i\frac{\omega}{\omega_{R1}}}, \qquad 2\text{-}26$$

where $\chi_o = \frac{4M_s^{\ 2}}{l\alpha}$ is the static susceptibility, $\omega_R = \sqrt{\frac{\alpha}{m_w}}$ is the wall resonance angular frequency, and $\omega_{R1} = \frac{\alpha}{\beta}$ is the wall relaxation angular frequency. Taking into account of $f = \frac{\omega}{2\pi}$ and $\mu_0 = \chi_0 + 1$, we can rewritten Eq. 2-26 as:

$$\mu(f) = \chi(f) + 1 = \frac{\chi_o}{1 - \left(\frac{f}{f_R}\right)^2 + i\frac{f}{f_{R1}}} + 1, \qquad 2\text{-}27$$

where f_R and f_{R1} are the intrinsic resonance and relaxation frequency, respectively.

2.2.4 Dispersion type

According to the magnitude of damping coefficient, the permeability spectrum can be divided into two typical types, namely resonance-type and relaxation-type.

In the case of $\lambda << 1$ for natural resonance or $f_R << f_{R1}$ for domain wall resonance, the permeability spectra are typical resonance-type. The expression of $\mu(f)$ for both

kinds of resonance can be given by an identical form as

$$\mu(f) = \frac{\chi_0}{1 + i\left(\frac{f}{f_{R1}}\right) - \left(\frac{f}{f_R}\right)^2} + 1 . \qquad 2\text{-}28$$

The real and imaginary parts can be written as

$$\begin{cases} \mu'(f) = \chi_o \dfrac{1 - (f/f_R)^2}{\left[1 - (f/f_R)^2\right]^2 + (f/f_{R1})^2} + 1 \\ \mu''(f) = \chi_o \dfrac{f/f_{R1}}{\left[1 - (f/f_R)^2\right]^2 + (f/f_{R1})^2} \end{cases} . \qquad 2\text{-}29$$

For natural resonance, f_R is the resonance frequency and $f_{R1} = {}^{2}\!/_{\lambda}\, f_R$. For domain wall resonance, f_{R1} represents the relaxation frequency and f_R is the intrinsic resonance frequency. This expression is usually known as Lorentz equation.

Figure 2-11a qualitatively shows the resonance-type permeability spectra. The real permeability $(\mu'(f) - 1)$ has a positive maximum and a negative minimum, and changes rapidly near the resonance frequency f_R. There is a narrow and strong resonance peak in the spectrum of the imaginary part $\mu''(f)$. The value of μ'' is maximum at the resonance frequency.

On the other hand, if $\lambda >> 1$ for natural resonance or $f_{R1} << f_R$ for domain wall resonance, $\mu(f)$ for both resonances can be simplified as

$$\mu(f) = \frac{\chi_0}{1 + i\left(\frac{f}{f_R}\right)} + 1, \qquad 2\text{-}30$$

which is Debye equation. The corresponding real and imaginary parts are

$$\begin{cases} \mu'(f) = \dfrac{\chi_0}{1+(f/f_R)^2} + 1 \\ \mu''(f) = \chi_0 \dfrac{(f/f_R)}{1+(f/f_R)^2} \end{cases} . \qquad 2\text{-}31$$

This is typical relaxation-type permeability spectra and f_R represents the relaxation frequency f_{R1}.

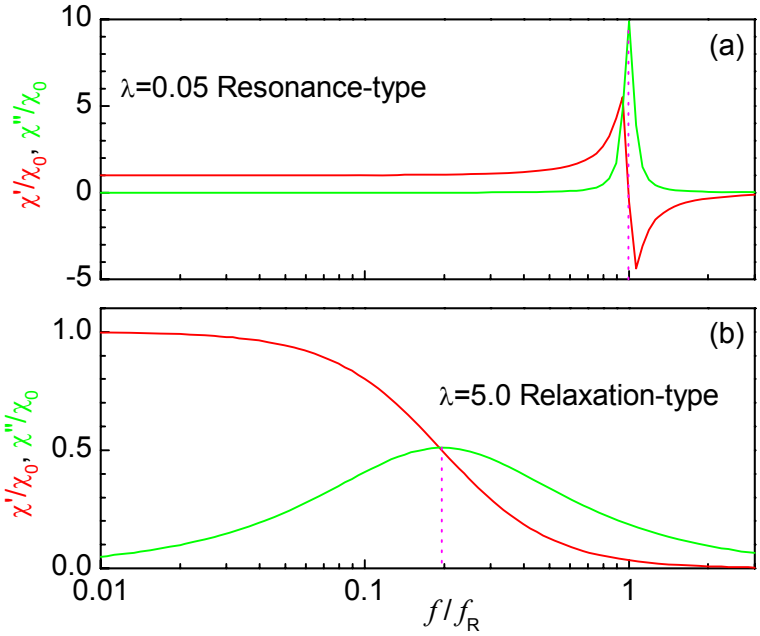

Fig. 2-11. Typical complex permeability spectra: (a). Resonance-type and (b). Relaxation-type.

The dependence of complex permeability on frequency is qualitatively shown in Fig. 2-11b. With the increase in frequency, the real permeability μ' monotonously and slowly decreases, and is always larger than unity. There is a broad and weak resonance peak for the spectrum of the imaginary part $\mu''(f)$. The maximum imaginary permeability $\mu''_{\max}$ is about half of the static susceptibility χ_0. However,

for most of EM materials, the permeability spectra are expected to be middle-type, which is between the resonance- and relaxation-type.

According to Fig. 2-11, the frequency corresponding to the maximum imaginary permeability $\mu''_{\max}$ is defined as the apparent resonance frequency f_r. Obviously, for resonance-type dispersion, the apparent resonance frequency f_r is close to the intrinsic resonance frequency f_R. However, for relaxation-type, f_r is smaller than f_R. In this study, for simplicity, the apparent resonance frequency f_r is also called as resonance frequency. But it should be borne in mind that f_r is different from the intrinsic resonance frequency f_R. The relationship between f_r and f_R can be derived as follows.

Based on Eq. 2-22, the imaginary permeability can be expressed as

$$\mu''(f) = \chi''(f) = \chi_0 \frac{\lambda\left(f/f_R\right)\left[1+\left(1+\lambda^2\right)\left(f/f_R\right)^2\right]}{1-2\left(1-\lambda^2\right)\left(f/f_R\right)^2+\left(1+\lambda^2\right)^2\left(f/f_R\right)^4}. \qquad 2\text{-}32$$

In the condition of $\frac{\partial \mu''(f)}{\partial f} = 0$, the maximum imaginary permeability $\mu''_{\max}$ is obtained as

$$\mu''_{\max} = \frac{1}{2}\chi_0\sqrt{1+\frac{1}{\lambda^2}}. \qquad 2\text{-}33$$

The corresponding frequency is

$$f_r = \sqrt{\frac{1}{1+\lambda^2}} f_R. \qquad 2\text{-}34$$

In addition, from Eq. 2-33, it can be deduced that the maximum imaginary permeability is tightly related with the static susceptibility χ_0 and the damping coefficient λ. A large μ''_{max} can be obtained in the case of large χ_0 or small λ.

2.3 Previous investigation on high-frequency hexaferrites

Due to very high specific resistance, remarkable flexibility in tailoring the magnetic properties, ease of preparation, and, last but not least, price and performance considerations, hexaferrites are the first choice for microwave absorbing materials. However, there are still some problems, such as very high resonance frequency, low permeability and high density, *etc.*. In this section, the previous investigation on high-frequency properties for hexaferrites, such as resonance frequency, permeability and absorbing ability, will be generally reviewed.

2.3.1 Control of resonance frequency

Microwave frequency bands cover a frequency range from 3 MHz to 300 GHz, but the greatest number of operational radar waves fall within 1-18 GHz. According to the introduction in Chapter 1, the microwave absorbing characteristics of EM materials are mostly controlled by the complex permittivity ε and permeability μ. Since the complex permittivity of ferrites is constant in the GHz frequency region, the absorbing characteristics strongly depend on the resonance phenomena of the ferrite body.[6] In the preceding section, the magnetic resonance has been described and classified as domain wall resonance and natural resonance.

Kwon *et al.* investigated the effect of the resonance phenomena on the microwave absorbing properties of NiZn-substituted *Y*-type ferrites ($Ba_2Ni_{2-x}Zn_xFe_{12}O_{22}$).[38, 44]

They reported that the domain wall resonance did not seem to affect the microwave absorbing phenomena, and the absorbing phenomena occurred by natural resonance only. The matching frequency f_m, at which the minimum reflectivity is obtained, is always slightly higher than the natural resonance frequency f_r.

It has been introduced that the natural resonance frequency f_r is determined by the anisotropy field H_a or H_θ (Section 2.2.2) and the crystalline anisotropy of hexaferrites can be changed over a large range of values by the substitution of the transition metal ions for other divalent ions (Section 2.1.3). Therefore, it was proposed to modify the resonance frequency with suitable ions substitution. The most-studied example is the substitution of Fe^{3+} by an ion or ions pair in *M*-type ferrites.

Cho *et al.* investigated the magnetic and microwave absorbing properties for $BaFe_{12-2x}A_xCo_xO_{19}$ with planar magnetic anisotropy, where A is a tetravalent ion of Ti^{4+} or Ru^{4+}.[45] They reported that, for the sintered specimen with TiCo (x=1.3), the resonance frequency is 2.56 GHz. The specimens with RuCo have higher resonance frequencies of 7.23 GHz (x=0.5) and 9.38 GHz (x=0.7). The initial permeability at low frequency is 5.3, 3.0 and 2.5 for TiCo (x=1.3), RuCo (x=0.5) and RuCo (x=0.7), respectively. The smaller the initial permeability, the higher the resulting resonance frequency is. On the other hand, the complex permeability spectra were also measured for the composites (the mixing ratio of ferrite powder to silicon rubber was 4 by weight). Comparing with the sintered specimen, both μ' and μ'' are reduced and the resonance frequency is shifted to higher frequency. The microwave absorbing property of the composites was estimated and listed in Table 2-5.

The high-frequency properties and microwave absorption was studied in a wide

frequency range (5-70 GHz) of ferrite powders belonging to the systems $BaSc_xFe_{12-x}O_{19}$ and $Ba(CoTi)_xFe_{11.9-x}Mn_{0.1}O_{19}$, where x varies from 0 to 1.8.[46] The introduction of Mn is related to the observed improvement of the dielectric properties at microwave frequencies of CoTi-substituted Ba hexaferrites.[47] It was found that, as x increases from 0 to 1.6, the natural resonance frequency continuously decreases from about 48 GHz to 10 GHz for Sc-substituted ferrite and 16 GHz for CoTi-substituted sample. Furthermore, for the same amount of additive, the Sc-substituted ferrite has the lower natural resonance frequency.

Table 2-5. The matching frequency f_m, the matching thickness t_m, the minimum reflection loss RL_{min}, the upper- and lower-limits of frequency, f_{up} and f_{low}, of bandwidth for absorption of more than 10 dB, and the relative bandwidth of $W=f_{up}/f_{low}$ for the composites of $BaFe_{12-2x}A_xCo_xO_{19}$ ($A=Ti^{4+}$ or Ru^{4+}).[45]

	f_m (GHz)	t_m (mm)	RL_{min} (dB)	f_{up} (GHz)	f_{low} (GHz)	$W=f_{up}/f_{low}$
A=Ti; x=1.3	9.5	2.94	-28	11.0	5.4	2.04
A=Ru; x=05	13.4	2.20	-32	15.1	7.9	1.91
A=Ru; x=0.7	14.0	2.00	-47	17.8	9.1	1.96

Polycrystalline hexaferrites with composition $BaFe_{12-2x}A_xMe_xO_{19}$ (A=Ru, Ir; Me=Co, Zn) were prepared by standard ceramic techniques for x varying from 0 to 1.[48] As expected, the natural resonance frequency is very high for a low substituted ratio, decreases with x as the axial anisotropy field gets lower, reaches a minimum when this axial field disappears, then increases again with the in-plane anisotropy field. Magnetic losses (μ'') are the highest (~5-6) when the resonance frequency reaches a minimum of about 2 GHz.

High-frequency magnetic properties for polycrystalline hexagonal ferrites ($Ba_2(Ni_{1-}$

$_xZn_x)_2Fe_{12}O_{22}$, $Ba_3(Co_{1-x}Zn_x)_2Fe_{24}O_{41}$ and $Ba(Co_{1-x}Zn_x)_2Fe_{16}O_{27}$) were systematically investigated by Nakamura *et al.*.[49] The samples were prepared by the double sintering method and the complex permeability spectra were measured at the frequency range from 6 MHz-6 GHz. In the *Y*-type ferrites, all of them exhibited soft magnetic performance (*c*-plane anisotropy). As x increases from 0 to 0.8, the low-frequency permeability increases from 4 to 15 and the natural resonance frequency shifts from 1.5 to 0.5 GHz. In *Z*- and *W*-type ferrites, the soft magnetic materials were obtained with $x<0.6$ for the *Z*-ferrite and $x<0.5$ for the *W*-ferrite. For the *Z*-type ferrites, the low-frequency permeability increases from 15 to 21 and the natural resonance frequency shifts from 800 to 300 MHz, as x increases from 0 to 0.6. For the *W*-type ferrites, the low-frequency permeability increases from 5 to 14 and the natural resonance frequency shifts from 3 GHz to 800 MHz, as x increases from 0 to 0.5. The electromagnetic wave absorption on the metal-backed single layered structure was estimated and listed in Table 2-6.

Kim *et al.* also investigated the magnetic (static and high-frequency) and microwave absorbing properties for *W*-type hexaferrites of $BaCo_xNi_{2-x}Fe_{16}O_{27}$ (x varying from 0 to 1.4).[50] They reported that the resonance frequency decreases with Co substitution. The specimens with composition of x=0.2 and x=0.4 show the superior microwave absorbing properties in Ka-band (26.5-40 GHz). For the specimen of x=0.4, the bandwidth (with respect to -20 dB reflection loss) is 26.5-32 GHz at a matching thickness of 0.9 mm. The CoNi-substituted BaW ferrites can, therefore, be suggested as a good absorbing material for the electromagnetic radiation in the frequency range of Ka-band.

ZnTi-, In- and Sc-substituted *Z*-type ferrites ($Ba_3Zn_2Fe_{24}O_{41}$) were investigated by

Lubitz.[51] It was found that In and Sc have only a small effect on the resonance frequency at the concentrations studied. The additional Zn and Ti, on the other hand, rapidly reduce the resonance frequency until ~1 Fe/f.u. (one of the 24 Fe atoms in the formula unit) is removed. Since, the *Z*-structure only contains one bipyramidal site/f.u., and this site has a major role in producing the uniaxial anisotropy, it was inferred that the strong reduction of anisotropy is a result of the Zn and/or Ti having a strong preference to replace Fe at that site. In addition, Lubitz *et al.* also reported that the resonance frequency of *Z*-type hexaferrites can be controlled over a wide range by choice of an appropriate mixture of Zn, Ni and Co as divalent species and these materials are suitable for microwave absorption in the 5-20 GHz range.[52]

Table 2-6. The center frequency, the matching thickness and the absorption band, in which the absorption is more than 10 dB, for the hexagonal ferrite single layered absorbers.[49]

x		Center Fre. (GHz)	Mat. Thick (mm)	Absor. Band (GHz)
Y-type	0	3.6	3.0	2.5-4.8
	0.2	2.7	3.0	1.8-3.6
	0.4	2.4	3.0	1.4-3.0
	0.6	2.1	3.0	1.2-2.9
	0.8	1.4	3.5	0.7-2.0
Z-type	0	1.2	3.0	0.7-2.1
	0.3	1.2	3.0	0.7-2.1
	0.4	1.1	3.0	0.6-2.0
	0.5	0.9	3.5	0.5-1.7
	0.6	0.7	4.0	0.4-1.1
W-type	0.4	3.6	2.0	2.1-5.5
	0.5	2.1	2.5	1.1-3.6

The effect of Co and Cu substitution on the magnetization mechanism of Zn_2Y ($Ba_2Zn_{2-2x-2y}Co_{2x}Cu_{2y}Fe_{12}O_{22}$ with $0 \leq x \leq 0.1$ and $0 \leq y \leq 0.4$) hexagonal ferrite was investigated.[53] Experimental results showed that Co substitution will increase the magnetic anisotropy distinctly and move the resonance peak towards high frequency; Cu substitution will decrease the initial permeability and tune dispersion character in very high frequency efficiently. Proper control of treatment conditions is necessary to improve the magnetic properties. The similar contribution of Co substitution on the resonance frequency of $Ba_2Zn_xCo_{2-x}Fe_{12}O_{22}$ was also reported by Zhang *et al.*.[54]

2.3.2 Enhancement of EM absorbing ability

It has been mentioned that, for ferrite materials with excellent absorbing ability, high permeability μ' and large magnetic loss in microwave frequency are necessary. Therefore, in order to enhance the absorbing performance, it is vital to improve the permeability of hexaferrites.

A research group in China has conducted some studies on designing the high-frequency property and absorbing performance of hexaferrites. The CoTi-substituted barium ferrites $BaFe_{12-2x}Co_xTi_xO_{19}$ were prepared by chemical coprecipitation and low-temperature sintering with Bi_2O_3 doping.[55] It was found that the initial permeability of sintered barium ferrites could be promoted effectively with Bi_2O_3 doping. Furthermore, high temperature for barium ferrite particles fabrication resulted in high permeability for sintered ferrites. The initial permeability $\mu' > 14$ of sintered ferrites could be obtained with Bi_2O_3 content varying from 2 to 5 wt% compared with $\mu' = 6$ without Bi_2O_3 doping when sintered at 950 °C for 5 h. Barium ferrites with initial permeability $\mu' > 10$, magnetic resonant frequency > 1 GHz were obtained

when they were sintered at 900 °C with 2 wt% Bi_2O_3 doping in the CoTi substituted range 1.2-1.3. On the other hand, they also investigated the low temperature sintering behaviors and high-frequency properties of Cu-modified Co_2Z ferrites.[56, 57] The microstructures and properties are significantly influenced by the sintering temperature, the amount of Bi_2O_3 addition, as well as Cu content. In addition, Mn-substituted $Ba_3Co_2Fe_{23-12x}Mn_{12x}O_{41}$ hexaferrites where $0 \leq x < 0.1$ were investigated.[58] It was found that the initial permeability was sensitively controlled by the substitution of Mn because of magnetostriction compensation.

There are some other investigations carried out by some researchers in Japanese.[59, 60] It was reported the $BaFe_{9.5}(Co_{0.4}Ti_{0.6})_{2.5}O_{19}$ sample, which was sintered at 1423 K for 5 hrs with a Bi_2O_3 addition of 2 wt%, exhibited high permeability (μ''_{max} =25 and μ''_{1GHz} =10). This sample also showed a good microwave absorbing property (*RL*<-20 dB) with a small matching thickness of 3.1 mm at 0.65 GHz. On the other hand, the EM wave absorption properties for composites of TiMn-substituted ferrite ($BaFe_{12-x}(Ti_{0.5}Mn_{0.5})_xO_{19}$) and epoxy resin were investigated by these researchers.[61, 62] The permeability, which originate from the ferromagnetic resonance, can be controlled both in the frequency axis and in amplitude by adjusting the substituted amount x and the powder mixture ratio. The $BaFe_9(Ti_{0.5}Mn_{0.5})_3O_{19}$ ferrite-resin composite, which was produced by sintering at 1573 K for 20 h, crushing into powder (150-300 μm) and mixing with epoxy resin at a ratio of 70 mass%, exhibited a wide bandwidth (Δf=7.2 GHz) from 13.75 GHz to 20.95 GHz. Δf values of 1.4-5.4 GHz in the frequency range 6.35-15.65 GHz were obtained by changing x from 3.5 to 4.5. In addition, they also conducted an investigation on $Ba_{1-x}La_xZn_xFe_{12-x-y}(Me_{0.5}Mn_{0.5})_yO_{19}$ (x=0-0.5, y=1.0-3.0, Me=Zr or Sn) and found that the permeabilities (μ' and μ'') for

ZrMn-substituted samples are significantly larger than those for TiMn-substituted samples.[63]

The effect of glass addition on the magnetic properties of $(Ba_{0.5}Sr_{0.5})_3Co_2Fe_{24}O_{41}$ (Co_2Z) ferrites was investigated by Hsiang et al.[64] The densification of Co_2Z ferrites was enhanced by addition of glass due to the liquid phase sintering. The initial permeability decreased slightly and the resonant frequency shifted to a higher frequency range with increasing the addition of glass.

Based on the above reviews, it can be deduced that both ions substitution and oxides doping are effective to control the high-frequency magnetic properties and EM absorbing performance. However, there are few studies which directly present the effect of oxides doping on absorbing behavior for *W*-type hexaferrites.

2.3.3 Considerations for practical applications

Some studies have been carried out to investigate the effects of ferrite materials and their volume concentration in the composite on absorbing performance.

Kim *et al.* studied the dependence of microwave absorbing property on ferrite volume fraction in MnZn ferrite-rubber composites.[65] In their work, the volume concentration of ferrite was varied in the range V_f=0, 0.1, 0.2, 0.26 and 0.4. They indicated that, as the ferrite volume fraction increases, the minimum reflection loss decreases from -5 dB to about -40 dB for V_f<0.26, and about -40 dB for $V_f \geq 0.26$. They concluded that the samples for V_f<0.26 are inadequate for microwave absorbing materials, although the samples for $0.26 \leq V_f \leq 0.45$ are adequate.

The complex permeability and permittivity spectra in X-band (8-12 GHz) frequencies and their relationship with microwave absorbing properties were investigated in ferrite-rubber composite material.[66] The mixing ratio of ferrite to rubber (F/R in weight) was varied in the range of 3-5. It is concluded that the variation of F/R ratio in the composite specimens, which is a useful technique to control the permeability and permittivity, gives a better insight into the relationship between the material constants and microwave absorbing properties.

It has been mentioned that large absorbing bandwidth should be one of characteristics of an ideal microwave absorbing material. In addition, low density is an important requirement for a practical application material. However, little work has been carried out about the dependence of density of composites and maximum absorbing bandwidth on the ferrite fraction.

CHAPTER 3: EXPERIMENTAL TECHNIQUES

3.1 Samples preparation

3.1.1 Hexaferrite powders

Many methods have been introduced to fabricate hexaferrites, such as chemical co-precipitation method,[67] glass crystallization method,[68] sol-gel method,[69] ball milling,[70] solid-state reaction,[71] water-in-oil emulsion,[72] and so on.[73, 74] A review of these methods has been given by Hibst.[75] To fabricate pure barium ferrite particles, the simplest one is solid-state reaction.[50, 76] In this work, all hexagonal ferrites were fabricated with this method.

W-type

To prepare ferrites of $BaCo_xZn_{2-x}Fe_{16}O_{27}$ (x=0-2), the starting materials were powders of high purity $BaCO_3$ (197.3392 g/mol, 99+%), Co_3O_4 (240.7972 g/mol, 99+%), ZnO (81.3894 g/mol, 99+%) and Fe_2O_3 (159.6922 g/mol, 99+%).

The chemical reaction is as follows:

$$BaCO_3+\frac{x}{3}Co_3O_4+(2-x)ZnO+8Fe_2O_3 \rightarrow BaCo_xZn_{2-x}Fe_{16}O_{27}. \qquad 3\text{-}1$$

In this formula, only the balance of elements of Ba, Co, Zn, and Fe is considered. This is because, during sintering in air, carbon reacts with oxygen to form volatile CO_2 and the required quantity of O_2 is controlled automatically by air.

The starting materials were weighed and mixed, then put into a vial made of hard steel, together with iron balls and appropriate amount of acetone enough to merge balls and mixture. The vial was then sealed and placed in a ball-mill machine. The mixture was ball-milled for half an hour and the slurry was poured into a beaker. After the evaporation of the acetone, the ferrite powders were molded under a pressure of about 8-10 tons to form cylindrically shaped samples of 16 mm in diameter and about 3 mm in thickness. A small quantity of polyvinyl alcohol (PVA) was used as a binding agent. The samples were then heated in a furnace in air for the first sintering. The heating curve is shown in Fig. 3-1. The heating and cooling rate was 5 ˚C per min and the dwell was 1200 ˚C for 4 hrs. Actually, the cooling rate was slower than the scheduled rate; the samples cooled down with the furnace at low temperature. Then the samples were ball-milled for 1.5 hrs. After desiccation, the mixture was then pressed into disks again, followed by the second sintering. The heating curve is similar to Fig. 3-1. However, the dwell temperature was 1270 ˚C instead of 1200 ˚C. Finally, the sintered disks were crushed into powders, which went thought a sieve with 200-meshes. The average size of the particles was less than 10 μm. The flow diagram of powders preparation is illustrated in Fig. 3-2.

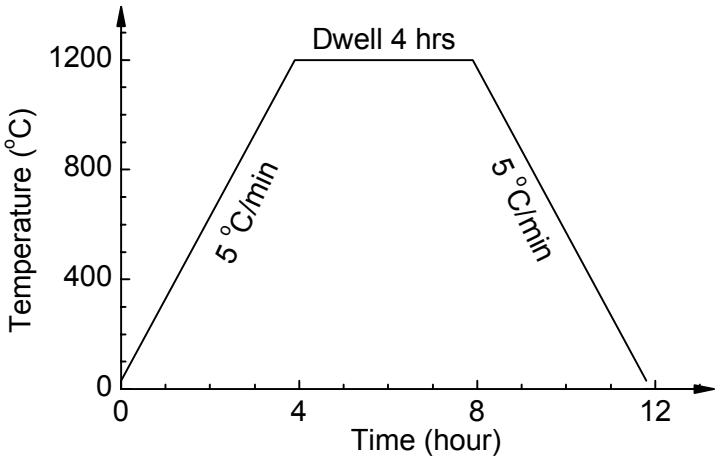

Fig. 3-1. A schematic heating process for the preparation of *W*-type bulks.

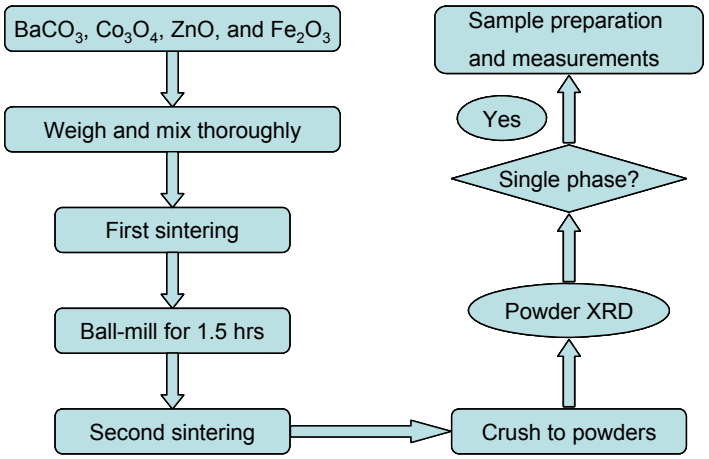

Fig. 3-2. Fabrication procedures for *W*-type powders by the solid-state method.

In addition, for the samples doped with a small amount of oxide, the preparation process was similar to those of the undoped samples. The only difference was, after first sintering, the required amount of oxide was added into the mixture and ball-milled together, as shown in Fig. 3-2.

Y-type

In this study, *Y*-type barium ferrites were fabricated by a two-step solid-state reaction. Firstly, *M*-type barium ferrite (BaM), $BaFe_{12}O_{19}$, is prepared by solid-state reaction. The starting materials for BaM were powders of high purity $BaCO_3$ (197.3392 g/mol, 99+%) and Fe_2O_3 (159.6922 g/mol, 99+%). The chemical reaction is as follows:

$$BaCO_3+6Fe_2O_3 \rightarrow BaFe_{12}O_{19}. \qquad 3\text{-}2$$

Similarly, in this formula, only the balance of elements of Ba and Fe is considered. According to the above equation, the required weight of $BaCO_3$ and Fe_2O_3 can be calculated. Similar to the preparation of *W*-type ferrite, the *M*-type ferrite powders were synthesized and used as the starting materials in the preparation of *Y*-type

ferrite. Fig. 3-3 shows the X-ray diffraction pattern for powders of BaM. The standard pattern for *M*-type structure is also included for identification, which is based on JCPDS International Center for Diffraction Data (Nos. 39-1433 and 84-0757). It is obvious that the sample is single phase with *M*-type hexagonal structure; hence, it is suitable for use as the starting material for BaY fabrication.

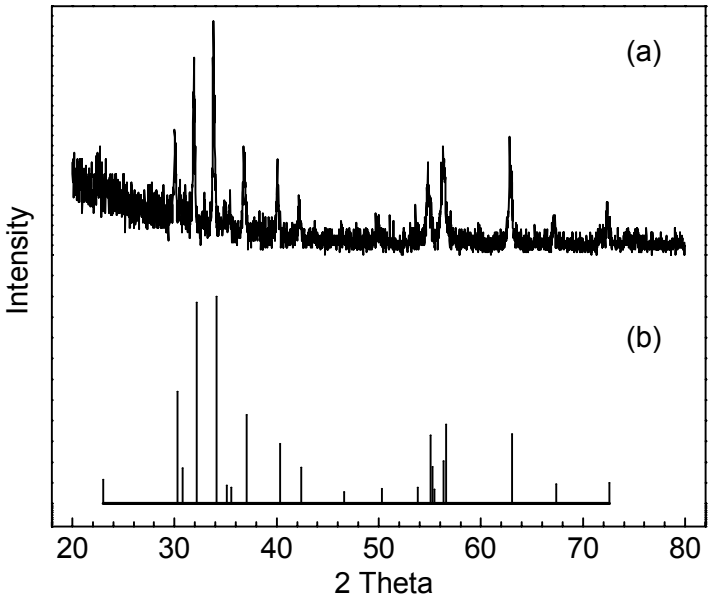

Fig. 3-3. X-ray diffraction pattern for $BaFe_{12}O_{19}$: (a) Experimental result and (b) Standard Pattern.

For $Ba_2Co_xZn_{2-x}Fe_{12}O_{22}$ (x=0-2) samples preparation, the starting materials were powders of $BaCO_3$ (197.3392 g/mol, 99+%), Co_3O_4 (240.7972 g/mol, 99+%), ZnO (81.3894 g/mol, 99+%), and $BaFe_{12}O_{19}$ (1111.4826 g/mol, pure phase confirmed by powder XRD).

The chemical reaction is as follows:

$$BaCo_3+\frac{x}{3}Co_3O_4+(2-x)ZnO+BaFe_{12}O_{19}\rightarrow Ba_2Co_xZn_{2-x}Fe_{12}O_{22}. \qquad 3\text{-}3$$

Similarly, the weight of $BaCO_3$, Co_3O_4, ZnO, and $BaFe_{12}O_{19}$ was calculated separately.

The starting materials were weighed, mixed and ground thoroughly for 1.5 hrs. After the evaporation of the acetone, cylindrically shaped ferrite samples of 16 mm in diameter and about 3 mm in thickness were heated in a tube furnace. The heating curve is shown in Fig. 3-4. The samples were heated from room temperature to 800 ˚C with the rate of 5 ˚C/min and from 800 ˚C to 1200 ˚C with the rate of 3 ˚C/min, followed by dwelling at 1200 ˚C for 4 hrs. Then the samples were cooled down slowly to room temperature and reground for 1.5 hrs. After desiccation, the mixture was then pressed into disks again and resintered following a similar curve as based on Fig. 3-4. However, the dwell time was 10 hrs instead of 4 hrs. Finally, the sintered samples were crushed into powders for the phase-verification and specimens preparation. Similarly, a sieve with 200-meshes was used and the average size of the particles was less than 10 μm. The flow diagram of powders preparation is illustrated in Fig. 3-5.

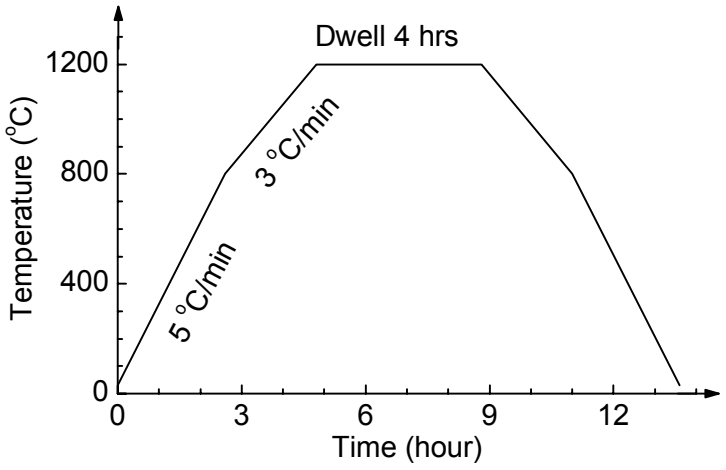

Fig. 3-4. A schematic heating process for the preparation of *Y*-type bulks.

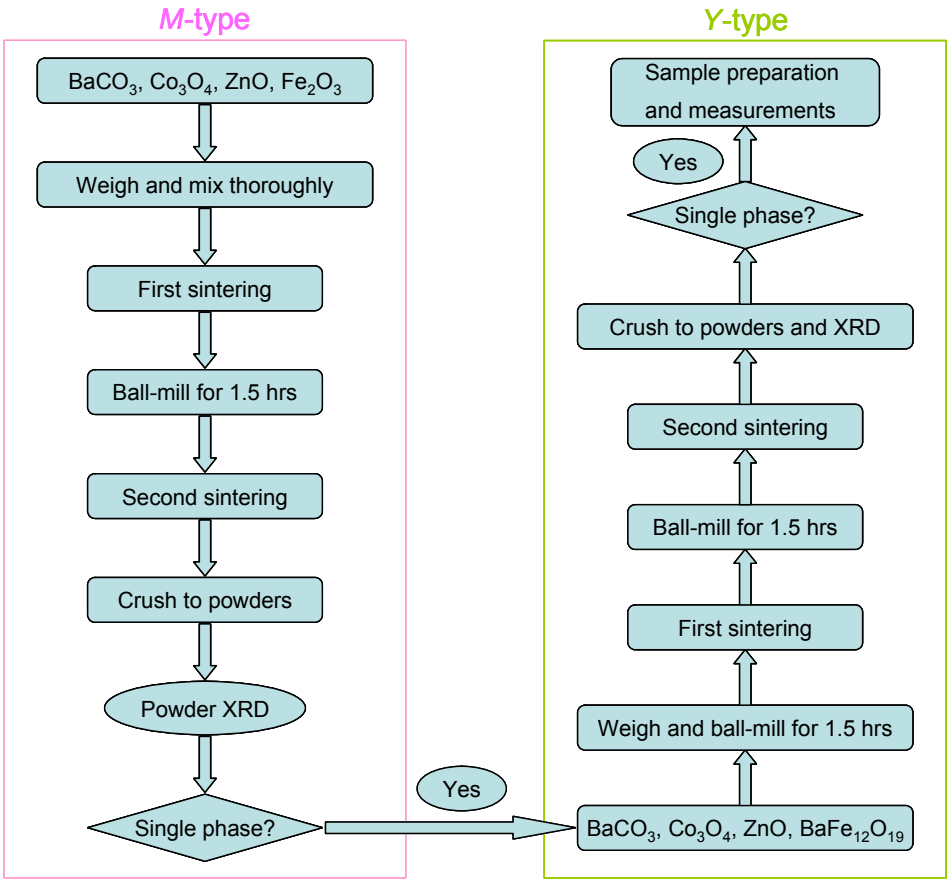

Fig. 3-5. Preparing procedures for *Y*-type ferrite by a modified solid-state method.

3.1.2 Specimens for measurement

Three types of specimens were fabricated for various measurements. (1). In order to measure magnetization curves and *M*-*H* loops, the sintered sample with diameter of about 4 mm and thickness of about 1.5-1.8 mm was prepared. The procedure of preparing this kind of specimen is very simple. With a specially designed mould, a small amount (about 0.05 g) of ferrite powders was pressed into a disk and sintered at 1270 ˚C (BaW) or 1200 ˚C (BaY) for 4 hrs. After weighting, this sample will be used for VSM measurement. (2). Magnetically aligned samples were prepared for the measurement of magnetocrystalline anisotropy field. (3). In order to characterize dynamic magnetic properties, composites were prepared by mixing fine powders of

ferrite with epoxy resin. In this section, the fabrication of aligned samples and composites will be introduced in detail.

Aligned samples

The aligned samples were prepared by mixing the fine powders of ferrite with epoxy resin, followed by placing the mixture into a mould under a magnetic field. These samples were used in X-ray diffraction test and the measurement of anisotropy field H_a or H_θ.

In order to obtain a well-aligned sample, some conditions need to be obtained. Firstly, the used particles must be fine enough to be with the scale of single-domain size. Secondly, the volume concentration of the powders should be very small so that the powders can rotate freely. Normally, the size of the particles is about 1 μm and the concentration of the ferrite is about 7 % by weight. Thirdly, all powders should be magnetically aligned before the solidification of matrix. The used epoxy resin is completely solidified in about 90 min. Hence, the whole process of sample preparation must be completed in short time. In general, the duration is controlled under 30 min. Finally, a magnetic field with suitable intensity is needed. In this work, the applied magnetic field is 3-6 kOe and is modified with the magnitude of anisotropy field for various samples.

The starting materials, ferrite powders and epoxy resin, were weighed separately and mixed together completely. The mixture was then filled in hollow aluminum moulds with a thickness of 2 mm, and diameters of 20 mm and 4 mm.

Subsequently, the mould was placed perpendicularly in a magnetic field. After the epoxy was solidified, the magnetic field was removed. The aligned status and the

type of magnetocrystalline anisotropy (*c*-axis or *c*-plane) were checked by X-ray diffraction using the large disk-like aligned sample (diameter of 20 mm). The small samples (diameter of 4 mm) will be used to determine the anisotropy field (H_a or H_θ).

Composites for microwave measurement

The composites for microwave measurement were prepared by mixing fine powders of ferrite with epoxy resin. The volume concentration of ferrite powders is between 25 and 50 %. The density of the ferrite powders is estimated at 5.3 g/cm^3 and the density of the epoxy resin is 1.1 g/cm^3. The powders and the epoxy resin according to required volume concentration were mixed homogeneously and then put the mixture into a toroidal mould with an outer diameter of 6.9 mm, an inner diameter of 3.0 mm, and a length of about 6.8 mm. The mixture is placed in an oven at 70 ºC for 24 hrs for the solidification of the epoxy. Finally, each composite sample was cut into three pieces with a thickness of about 2 mm for the microwave measurement. In order to reduce the experimental errors, the values of complex parameters were obtained by averaging over the data measured from three different samples for each composite.

3.2 Measurement equipment

Several kinds of techniques were used to characterize the microstructure, static magnetic properties and microwave properties of ferrites. They include X-ray diffraction (XRD), field-emission gun scanning election microscope (FEG-SEM), vibrating sample magnetometer (VSM), vector network analyzer (VNA) and the impedance/material analyzer.

3.2.1 X-ray diffraction (XRD)

XRD is conventionally used to characterize crystal structures. The spacing between the diffraction crystal planes (d) and the angle of incident X-ray (θ) obey Bragg's Law:

$$2d \sin\theta = n\lambda, \qquad 3\text{-}4$$

where n is the order of corresponding reflection, and λ is the wavelength of the X-ray source. The intensity of the diffracted X-rays is recorded as a function of the diffraction angle 2θ. From this equation, the d spacing can be obtained.

In this study, a Philips PW1710 Diffractometer with a Cu K_α radiation source (λ=1.54056 Å), combined with the computer running *PC-APD* analytical software for peak identification, was used. The scan mode used was θ-2θ. The step size of the scan (2θ angles) was 0.02 º and the scanning speed was 0.01 º/s. By comparing the measured 2θ angles (or d-spacing) and relative intensity of the corresponding peak with the standard patterns found in the JCPDS powder diffraction file, the crystalline phase can be identified. Furthermore, the lattice parameters can be calculated based on the Miller indices of each set of crystal planes, which will be explained in the next section.

3.2.2 Scanning electron microscopy (SEM)

SEM is a widely used materials characterization technique for its large depth of focus, the excellent contrast and easy preparation of particle, solids and thin films samples. It is extensively used in surface imaging, microstructure examination and particle size evaluation. In a SEM, electrons thermoionicly emitted from a LaB_6 cathode filament are drawn to an anode, focused by two successive condenser lenses into a beam with

very fine spot size. Electron beams have energy up to 20-30 keV. Upon impinging on the specimen, the primary electrons decelerate in losing energy and transfer the energy inelastically to other atomic electrons and to the lattice. Through continuous random scattering events, the primary beam effectively spreads and fills a teardrop-shaped interaction volume with a multitude of electronic excitations. The result is a distribution of electrons that manage to leave the specimen with an energy spectrum. The SEM imaging mode relies on detection of this lowest portion of the emitted energy distribution. Their very low energy means they originate from a surface depth of no larger than several angstroms. The signal is captured by a detector consisting of a scintillator-photomultiplier combination, and the output serves to modulate the intensity of a CRT, which is rastered in synchronism with the raster-scanned primary beam. The image magnification is then simply the ratio of scan lengths on the CRT to that on the specimen. Great depth of focus enables to obtain images with three-dimensional quality from a nonplanar surface.

In the present study, a Philips field-emission gun 300 scanning election microscope was used, which has a maximum accelerating voltage of 30 kV with maximum magnification of about 200,000. Because barium ferrite is electrically insulating at ambient temperature, a very thin platinum overcoat is generally sputtered on the surface before scanning to avoid surface charge accumulation.

3.2.3 Vibrating sample magnetometer (VSM)

VSM is widely used in magnetic materials research to measure the static magnetic properties. The general arrangement of a VSM is shown in Fig. 3-6. In a VSM, the time rate of change of magnetic flux in the pick-up coil is produced by mechanically

vibrating the magnetized sample. The magnetizing field in VSM can be provided either by an electromagnet or superconducting coils. If superconducting coils are used, magnetic field as high as several ten teslas can easily reached. The magnetic field in a VSM can be changed only slowly, over periods of ten of seconds. The sample is suspended on a nonmagnetic rod, which vibrates vertically over amplitude of perhaps 1.5 mm, at a frequency of 45 Hz. The pick-up coils are connected in pull-push; that is, as the sample ascends, both the coils produce the same electrical polarity. The alternating current (*ac*) voltage, which is proportional to sample's magnetic moment, produced by these coils is taken to an extremely high-gain lock-in amplifier. This lock-in amplifier is an extremely narrow bandwidth amplifier. The rectified output is then applied to a computer and the operation and the data processing are all controlled by it.

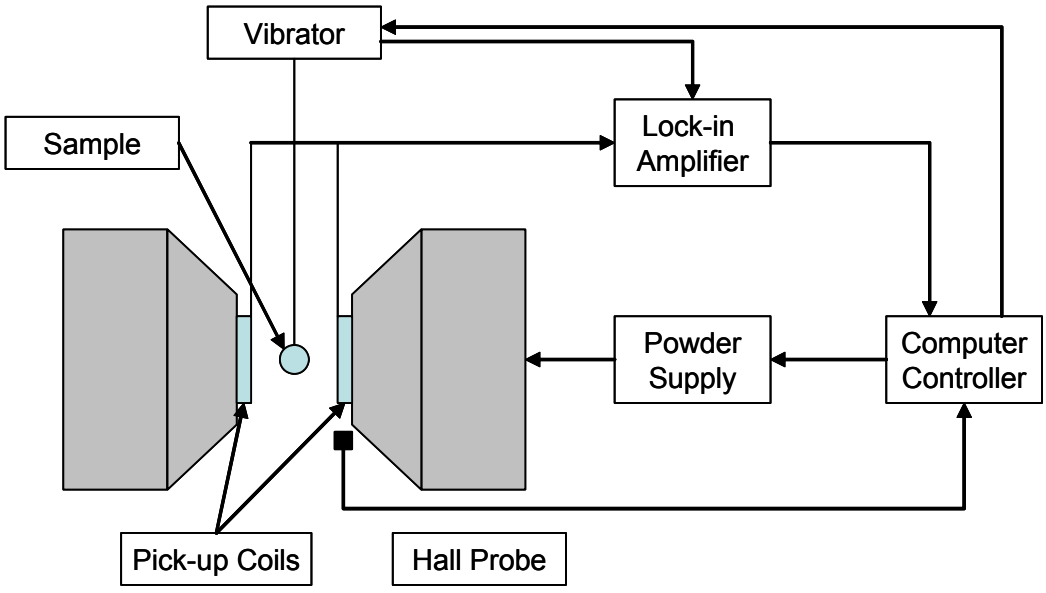

Fig. 3-6. A schematic diagram of a vibrating sample magnetometer.

In this work, an Oxford Instrument superconducting VSM with a maximum applied

field of 90 kOe and an Oxford Instrument electromagnetic VSM with a maximum applied field of 14 kOe were used. The VSM system should be carefully calibrated using the standard Ni samples.

The bulk sample for VSM testing is a disk of about 4 mm in diameter and 1.5-1.8 mm in thickness. The mass of sample is about 0.05 g, which is measured accurately. The magnetization (emu/g) was calculated from the data collected and the mass of sample. The demagnetizing corrections have been considered. For the sintered samples, the demagnetizing factors were calculated based on the shape of samples. For the aligned samples, due to very low volume concentration, the fine particles in epoxy can be considered as isolated particles without magnetic interaction. Therefore, the demagnetizing factors were taken as 1/3 along both easy and hard magnetization directions for the spherical particles.

3.2.4 Impedance/material analyzer & Vector network analyzer (VNA)

Impedance/material analyzer and VNA are widely-used equipments for the high-frequency measurements. In this study, the complex permeability μ and permittivity ε were simultaneously obtained by measuring the S_{11} and S_{21} parameters over 0.5-16.5 GHz using a HP8722D VNA. A HP4291B RF impedance/material analyzer was also used to measure the complex permeability over 0.01-1.8 GHz.

Impedance/material analyzer

Impedance/material analyzer can analyze impedance values, as well as permittivity ε and permeability μ. Impedance Z is generally defined as the total opposition a material, device or circuit offers to the flow of an *ac* at a given frequency, and is represented as a complex quantity. There are many measurement methods to determine impedance,

such as bridge method, resonant method, *I-V* method, RF *I-V* method, network analysis, and auto balancing bridge method.[77] For measurements from 100 MHz to 3 GHz, the RF *I-V* method may have the best measurement capability.

Figure 3-7 is the simplified block diagram for RF *I-V* method. The signal source section generates an RF test signal applied to the unknown device and had variable frequency range from 1 MHz to 3 GHz (typical). The amplitude of signal source output is adjusted for the desired test level by the output attenuator.

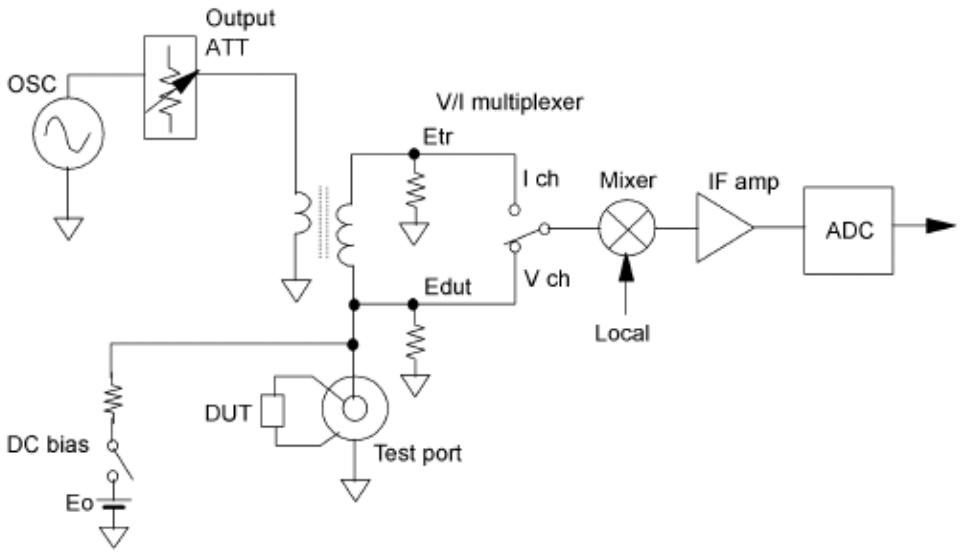

Fig. 3-7. Simplified block diagram for RF *I-V* method.[77]

The test head section is configured with a current detection transformer, *V*/*I* multiplexer, and test port. The measurement circuit is matched to the characteristic impedance of 50 Ω to ensure optimum accuracy at high frequencies. The test port also employs a precision coaxial connector of 50 Ω characteristic impedance. The *V* channel signal, E_{dut}, represents the voltage across the Device-Under-Test (DUT) and the *I* channel signal, E_{tr}, represents the current flowing through the DUT. Because the

measurement circuit impedance is fixed at 50 Ω, all measurements are made in reference to 50 Ω without ranging operation.

The *V/I* input multiplexer alternately selects the E_{dut} and E_{tr} signals so that the two vector voltages are measured with identical vector ratio detector to avoid tracking errors. The measuring ratio of the two voltages derives the impedance of the measured device as $Z = 50 \times (E_{dut} / E_{tr})$. Once the impedance has been found, it can be converted into the complex EM properties of the material, such as the complex permittivity ε and permeability μ.

In this study, a HP4291B RF impedance/material analyzer was used to measure the complex permeability over the frequency of 0.01-1.8 GHz. The impedance analyzer uses the RF *I-V* techniques to measure impedance from a ratio of voltage and current. To achieve highly accurate impedance measurements, a four-step calibration process was used to accurately resolve phase. In a conventional one-port calibration, open, short, and 50 Ω load standards are used. In the enhanced short/open/load/air-capacitor calibration, the air capacitor serves as a low-loss phase standard.

Vector network analyzer (VNA)

VNA is widely used in microwave frequency applications to measure the complex scattering (*S*) parameters of an unknown DUT. Two-port measurement technique, called transmission line technique, is commonly used in high-frequency measurements, as shown in Fig. 3-8. High-quality cables are used as transmission lines to connect to the device. The amount of energy that is reflected and transmitted is expressed as *S*-parameters. Fig. 3-8 and Eq. 3-5 show how the *S*-parameters are defined, where S_{11} is reflection a port 1 with port 2 matched, S_{21} is forward

transmission with port 2 matched, S_{12} is reverse transmission with port 1 matched, and S_{22} is reflection at port 2 with port 1 matched.

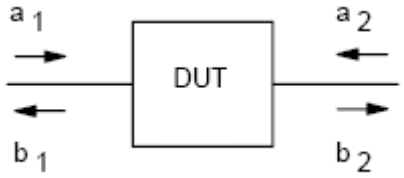

Fig. 3-8. Sacttering parameter description of a two-pot device.

$$\begin{pmatrix} b_1 \\ b_2 \end{pmatrix} = \begin{pmatrix} S_{11}S_{22} \\ S_{21}S_{22} \end{pmatrix} \begin{pmatrix} a_1 \\ a_2 \end{pmatrix} \qquad 3\text{-}5$$

To find the *S*-parameters, the measurement at b_1 or b_2 while a_1 or a_2 is carried out. Once the *S*-parameters have been found, they can be converted into the complex EM properties of the material, such as the complex permittivity ε and permeability μ.

Prior to measuring the sample, the VNA and associated cable connections should be calibrated. This process consist of measuring the reflection of open, short, and load terminators at the end of each of the phase matched cables, followed by connecting the two phase matched cables together and measuring the through and reflected response. Then the adapters are added and the reflection of open, short, and load terminators are measured. To check the calibration, an empty sample holder can be measured first. If the test of the empty sample holder showed no losses with a permittivity and permeability of 1, the calibration is completed and the VNA facility is ready for use.

In this study, a HP8722D VNA with a coaxial waveguide sample holder was used to measure the complex permittivity ε and permeability μ in the frequency range of 0.5-16.5 GHz. Custom software run on an external computer controls the VNA and the VNA is connected to a pair of 7 mm phase matched coaxial cables via its two ports. The length of the waveguide l is 59.96 mm. A gold-plated coaxial air line with a precision 7 mm connector interface was used to hold the measurement samples. The position of the samples was controlled carefully to ensure accuracy. S_{21} and S_{11} parameters were simultaneously measured. The complex permittivity and permeability were deduced from *S*-parameters. The Agilent Technologies 85071E Materials Measurement software streamlines the process of measuring complex permittivity and permeability with VNA. The easy-to-use software guides the user through setup and measurement, instantly converting *S*-parameter network analyzer data into the selected data format and displaying the results within seconds.

It should be noted that, in the measurement, the length of the waveguide l is 59.96 mm. When l is half of the wavelength or it's multiple, the corresponding frequency is

$$f = \frac{c}{\lambda} = \frac{c}{2l} n = \frac{3*10^{8}}{2*59.96*10^{-3}} n = 2.5n \text{ GHz},$$

where c is the velocity of light and n is a positive integer. The measurement results at these frequencies are inherently unstable and some peaks are observed. These peaks are not the intrinsic properties of the samples, and they are neglected in the following discussions.

3.3 Data analysis

3.3.1 Lattice parameters

In X-ray diffraction patterns, by measuring the 2θ values, the *d*-spacing (the distance between the diffracting planes) for each diffraction peak can be calculated. Meanwhile, according to the standard diffraction pattern, Miller indices, (*h k l*), are labeled for each peak. For crystals with hexagonal structure, the relationship between *d*-spacing and Miller indices is given by[78]

$$\frac{1}{d^2} = \frac{4}{3}\frac{(h^2 + hk + k^2)}{a^2} + \frac{l^2}{c^2}, \qquad 3\text{-}6$$

where *a* and *c* are lattice parameters.

Due to the experimental uncertainty, the calculated results are often accompanied by noise. In this work, the least squares method is used to decrease the experimental uncertainty. It is well known that the *d*-spacing can be written as $d_{hkl} = d_{hkl}(a,c)$. The optimum parameters *a* and *c* should make objective function

$$\phi = \sum_{i=1}^{m} \left(d_{hkl}(a,c) - d_{hkl}^{*} \right)^2 \qquad 3\text{-}7$$

minimum, where d_{hkl}^{*} is experimental data obtained from X-ray diffraction patterns, *m* is the total numbers of diffraction lines selected, and *j* is the *j*th data corresponding to the index of crystal plane (*h k l*). From $\partial\phi/\partial a = 0$ and $\partial\phi/\partial c = 0$, the optimum *a* and *c* can be obtained.

In addition, the unit cell volume *V* can be calculated by

$$V = \frac{\sqrt{3}}{2} a^2 c\,. \qquad 3\text{-}8$$

3.3.2 Anisotropy field

The anisotropy field, for both *c*-axis and *c*-plane anisotropies, can be determined by the initial magnetization curves for aligned samples (Method A). In addition, for *c*-axis anisotropy, H_a can also be estimated by the magnetization curves for normal sintered samples (Method B).

Method A

For aligned samples, the initial magnetization curves were measured by vibrating sample magnetometer (VSM) along two directions, which are parallel and perpendicular to the aligned direction. As shown in Fig. 3-9a, the easy and hard magnetization curves are joined together at a certain magnetic field; the field corresponding to the intersection of two curves is defined as the anisotropy field H_θ for *c*-plane anisotropy or H_a for *c*-axis anisotropy. On the other hand, for the sample with large anisotropy field, the maximum applied magnetic field is insufficient to induce magnetic saturation along the hard magnetization direction; hence, two magnetization curves are disconnected. However, it is found that the dependence of $M(H)$ on H is highly linear in the high-field region, as illustrated in Fig. 3-9b. In this case, the linear extrapolation is used to roughly estimate the anisotropy field.

Method B

For the sintered samples with *c*-axis anisotropy, the anisotropy field H_a also can be estimated based on the law of approach to saturation,[79, 80 81, 82]

$$M(H) = M_s(1 + \frac{A}{H} + \frac{B}{H^2} + \cdots) + \chi_p H, \qquad 3\text{-}9$$

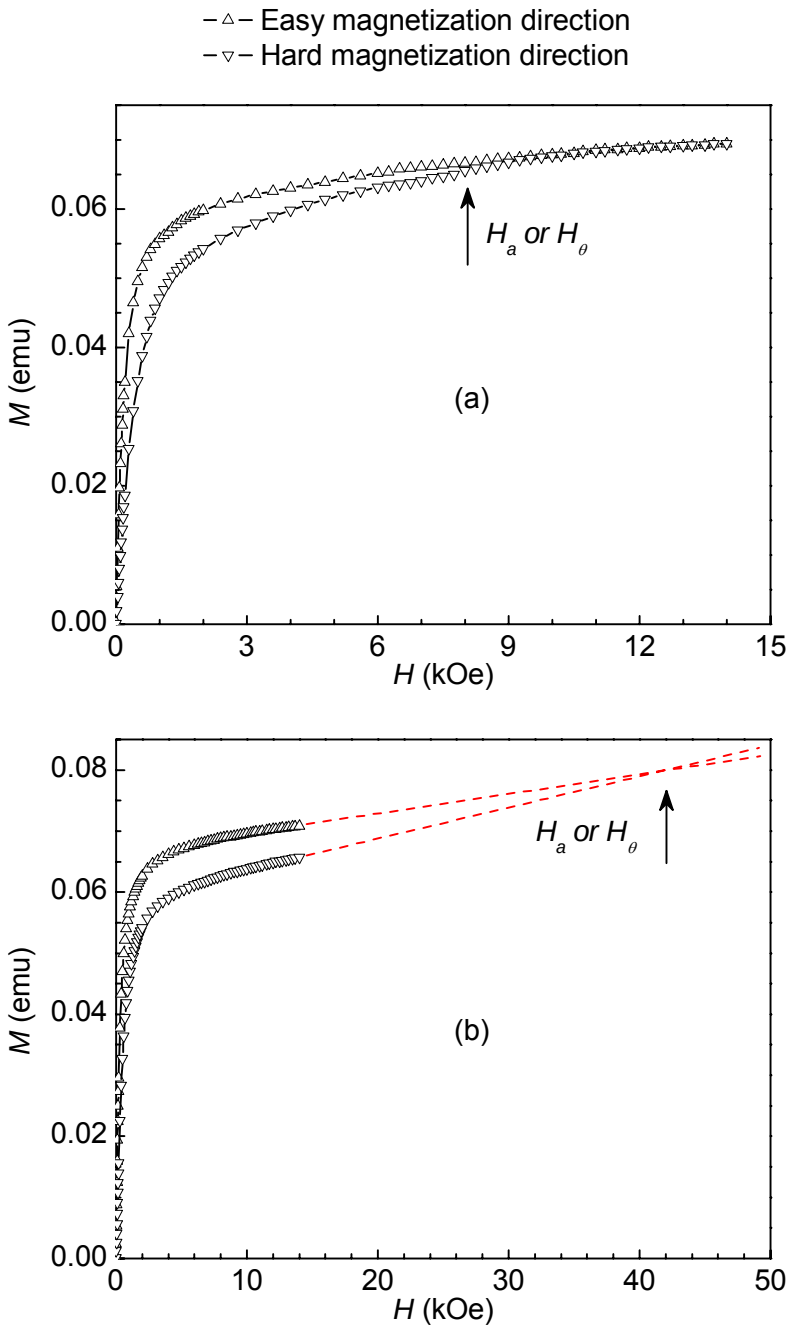

Fig. 3-9. The typical magnetization curves parallel and perpendicular to the alignment direction for the aligned sample. (a) Sample with small magnetocrystalline anisotropy; (b) Sample with large magnetocrystalline anisotropy.

where $H = H_0 - H_d$, H_0 is the applied field, and H_d is the demagnetization field of the samples. The term of A/H is related with the existence of inhomogeneities in the microcrystal, while B/H^2 is associated with the magnetocrystalline anisotropy.

Theoretically, the former should vanish at high fields.[83, 84, 85] Based on domain rotation model and the condition of $K_1 >> K_2$, where K_1 and K_2 are the first and second order magnetocrystalline anisotropy constants, respectively, B can be expressed as

$$B = -\frac{1}{15} H_a^2. \qquad 3\text{-}10$$

Based on the magnetization curve of $M(H)$ for sintered samples with *c*-axis anisotropy, the relationship between M and $1/H^2$ can be determined, as schematically shown in Fig. 3-10. It is found that there is a good linear relationship between $M(H)$ and $1/H^2$ in a specific range of magnetic filed, such as H=11-20 kOe for the example in Fig. 3-10. In this case, the terms of A/H and χ_p in Eq. 3-10 are neglected and the equation is expressed as

$$M(H) = M_s(1 + B/H^2). \qquad 3\text{-}11$$

Therefore, the value of B can be determined by the slope of the straight line and the anisotropy field H_a can be obtained by Eq. 3-10.

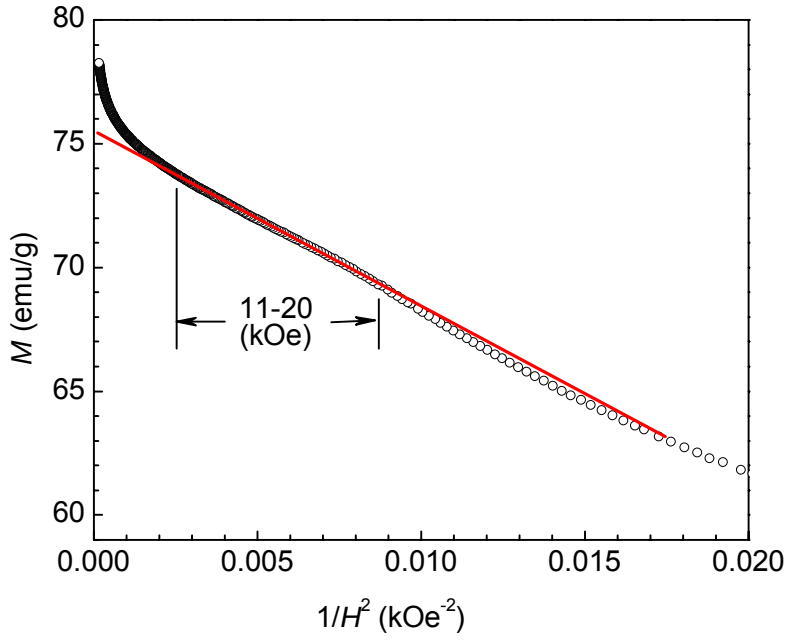

Fig. 3-10. The typical relationship between M and $1/H^2$ for sintered samples.

3.3.3 Saturation magnetization and coercivity

The values of saturation magnetization M_s and coercivity H_c can be estimated from magnetization curves and *M-H* loops, respectively. It has been mentioned that, two VSM facilities were used in this work; the magnetic field is produced by a superconducting coil with a maximum applied field of 90 kOe and by an electromagnet with a maximum field of 14 kOe.

For the results obtained from VSM with the superconducting magnet, it is observed that the dependence of $M(H)$ on H is highly linear in the high-field region , such as 50-80 kOe, as shown in Fig. 3-11a. Hence, with the neglecting of second, third and higher order terms, Eq. 3-9 can be rewritten as

$$M(H) = M_s + \chi_p H . \qquad 3\text{-}12$$

In this case, the values of M_s and χ_p can be obtained by a linear least squares fitting. On the other hand, for the results from VSM with electromagnet, the saturation magnetization M_s is defined as the value at the maximum applied filed of 14 kOe.

The *M-H* loops were measured with applied fields from -30 to +30 kOe for the VSM with superconducting magnet and from -14 to +14 kOe for that with electromagnet. The typical *M-H* loops for sintered samples are shown in Fig. 3-12. The coercivity H_c is obtained from the *M-H* loops.

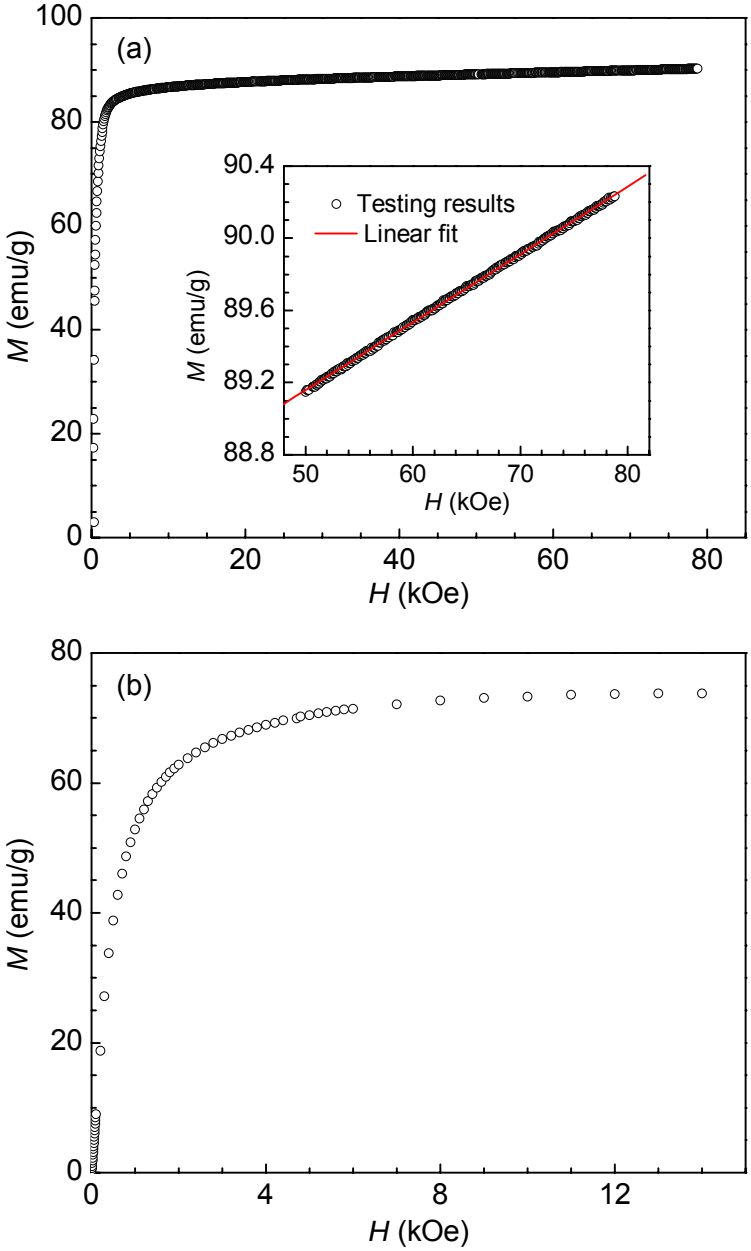

Fig. 3-11. Typical magnetization curves for sintered samples tested by: (a) superconducting VSM with applied field of 0-80 kOe; (Inset: Linear fitting result of magnezation curve in the range of 50-80 kOe.) and (b) electromagnetic VSM with applied field of 0-14 kOe.

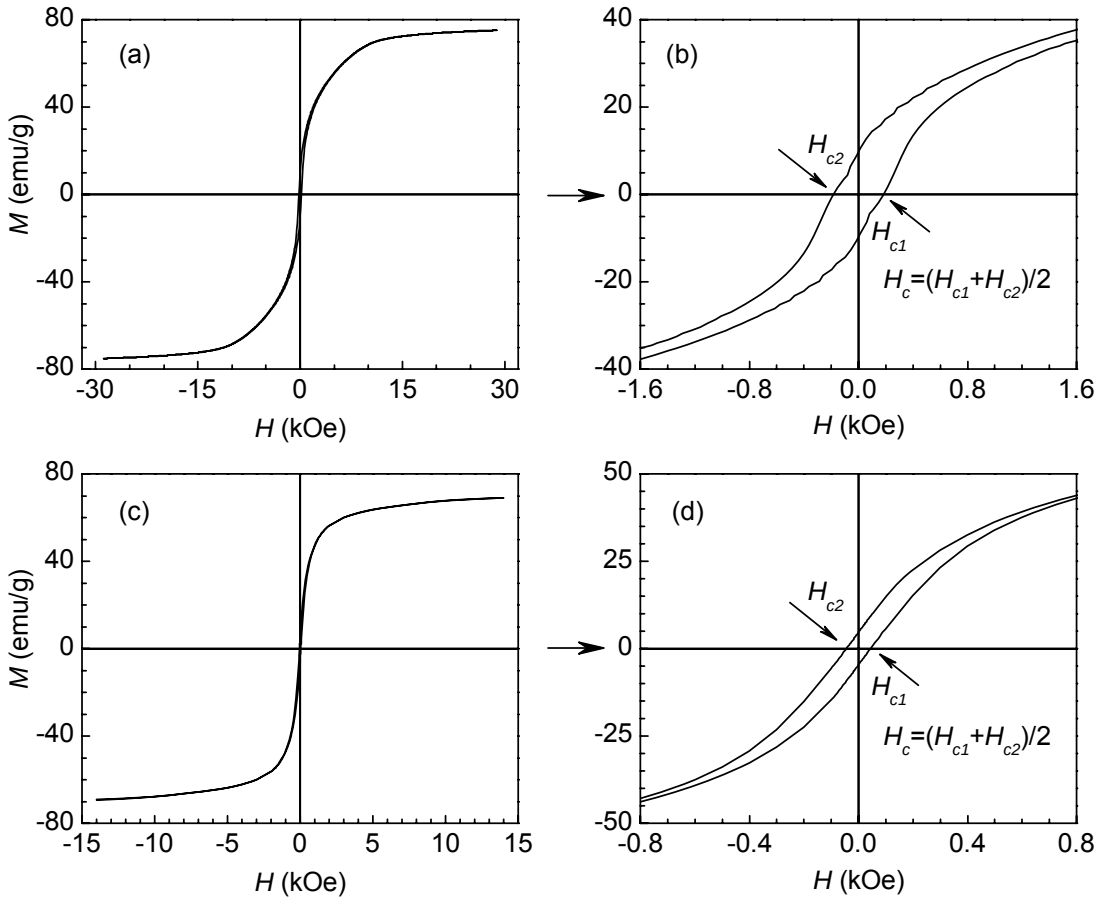

Fig. 3-12. Typical *M-H* loops for sintered samples tested by: (a). Superconducting VSM with applied field from -30 to +30 kOe, (b). Enlargement of the loop in (a) within -1.6 to 1.6 kOe, (c). Electromagnetic VSM with applied field from -14 to +14 kOe, and (d). Enlargement of the loop in (c) within -0.8 to 0.8 kOe,

3.3.4 Reflection Loss (*RL*)

In the case of a metal-backed single layer, Reflection loss (*RL*) is given by

$$\begin{cases} RL(dB) = 20\log\left|\dfrac{Z_{in}/Z_0 - 1}{Z_{in}/Z_0 + 1}\right| \\ Z_{in}/Z_0 = \sqrt{\mu/\varepsilon}\tanh\left|j(2\pi ft/c)\sqrt{\mu\varepsilon}\right| \end{cases}, \qquad 3\text{-}13$$

where Z_{in} is the impedance of the composites, Z_0 *is* the intrinsic impedance of free space, c is the light velocity, t is the thickness of composites, f is the frequency of the

incident EM wave, $\mu=\mu'-j\mu''$ is the complex permeability and $\varepsilon=\varepsilon'-j\varepsilon''$ is the complex permittivity. The values of complex of permittivity and permeability are taken from the results of VNA measurement.

To obtain impedance matching conditions of the single-layered absorber, the graphical map method is commonly used.[6, 44, 86, 87] In this study, another method proposed by Kim *et al.*[65] is used.

Firstly, based on Eq. 3-13, *RL* with various thickness *t* over 0.5-16.5 GHz is calculated using the data of ε and μ, as schematically illustrated in Fig. 3-13.

Secondly, for each thickness, there is a relative bandwidth of $W = f_{up} / f_{low}$, where f_{up} and f_{low} are the upper- and lower-frequency limits of the bandwidth for a given absorbing ability, such as -10 or -15 dB, respectively. Therefore, the dependence of *W* on the thickness *t* for each sample is obtained, as shown in Fig. 3-14.

Finally, based on the curve of *W*-*t*, the maximum relative bandwidth W_{max} and the corresponding thickness (or optimum thickness t_o) can be obtained.

For example, Fig. 3-13 shows the *RL*-*f* curves of each thickness. From this figure, we can obtain the curves of f_{up}-*t*, f_{low}-*t* and the corresponding *W*-*t*, as shown in Fig. 3-14. Thus, the maximum relative bandwidth W_{max} is 2.6 with an optimum thickness t_o of 3.1 mm and the corresponding bandwidth for absorption of more than 10 dB is from 4.7 to 12.3 GHz.

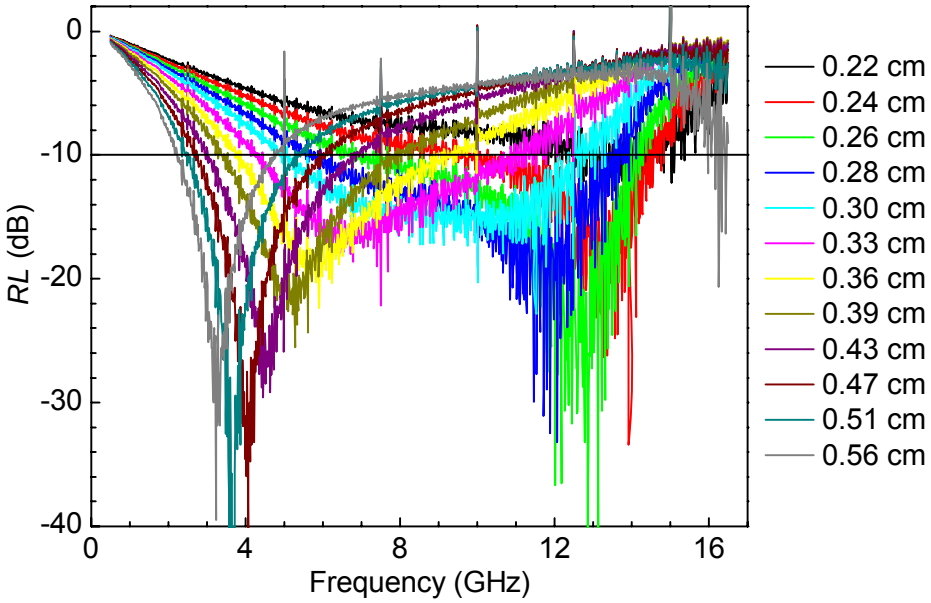

Fig. 3-13. Schematic illustration of absorbing performance for an assumed composite with various thicknesses.

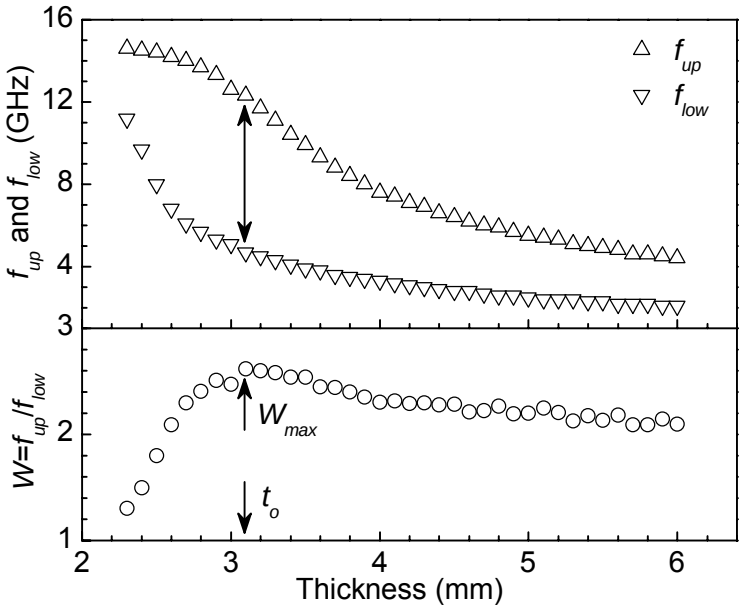

Fig. 3-14. The dependence of f_{up}, f_{low} and $W=f_{up}/f_{low}$ on thickness t for an assumed composite.

3.3.5 Fitting of permeability spectra

In general, for polycrystalline ferrites in an *ac* field, there are two different resonances, namely the natural resonance and the domain wall resonance. Correspondingly,

there are two types of susceptibility (permeability): gyromagnetic susceptibility and wall displacement susceptibility.[43, 88]

For the composite filled with randomly distributed barium ferrite particles with spherical shape, the gyromagnetic susceptibility $\chi(f)=\mu(f)-1$ can be described by the Kittle equation for natural resonance without an applied field,[42, 89]

$$\chi(f)=\frac{\chi_0\left(1+i\lambda f/f_R\right)}{\left(1+i\lambda f/f_R\right)^2-\left(f/f_R\right)^2}, \qquad 3\text{-}14$$

where χ_0 is the static gyromagnetic susceptibility, f_R is the intrinsic resonance frequency, and λ is the effective damping coefficient of composites. f_R is determined by the effective magnetic field, including the anisotropy field and demagnetizing field.

The domain wall resonance leads to the expression for the complex susceptibility of

$$\chi(f)=\frac{\chi_0}{1-\left(f/f_R\right)^2+i\left(f/f_{R1}\right)}, \qquad 3\text{-}15$$

where f_{R1} and f_R are the relaxation and intrinsic vibration frequencies, respectively. Eq. 3-15 is known as the Lorentz equation. In the case of $f_R >> f_{R1}$, Eq. 3-15 can be simplified as

$$\chi(f)=\frac{\chi_0}{1+i\left(f/f_{R1}\right)}. \qquad 3\text{-}16$$

This is the Debye equation.

Therefore, the complex permeability spectra can be expressed as

$$\mu(f) = \sum_{i}^{n} \chi_i(f) + B \,, \qquad 3\text{-}17$$

where B~1, n is the number of permeability contribution, and $\chi_i(f)$ can be expressed as Kittle, Lorentz or Debye equation.

The experimental permeability spectra $\mu(f_j)_{\exp}$ can be fitted by nonlinear least squares method with a target function ϕ,

$$\phi = \sum_{j=1}^{m} \frac{\left[\mu(f_j)_{\exp} - \mu(f_j)_{cal}\right]^2}{\Delta^2} \,, \qquad 3\text{-}18$$

where $\mu(f_j)_{cal}$ is the theoretical spectrum and Δ is the measurement error of permeability. The curve-fitting is over all measured frequencies. The subscript j represents the jth data.

CHAPTER 4: CoZn-SUBSTITUTED *W*-TYPE BARIUM HEXAFERRITE

In this chapter, CoZn-substituted *W*-type barium hexaferrites, $BaCo_xZn_{2-x}Fe_{16}O_{27}$ with x=0, 0.5, 0.7, 1.0, 1.5 and 2.0, were fabricated by solid-state reaction method. The crystal structure, static magnetic properties for bulk materials, including anisotropy field, saturation magnetization and coercive force, and high-frequency magnetic and absorbing properties for the composites filled with 35 vol% (volume concentration) of ferrite particles will be reported.

4.1 X-ray diffraction (XRD)

4.1.1 Patterns for powder

Figure 4-1 shows XRD patterns for powders of $BaCo_xZn_{2-x}Fe_{16}O_{27}$ with x=0, 0.5, 0.7, 1.0, 1.5 and 2.0. The standard position and intensity of X-ray diffraction lines for BaW are also given in Fig. 4-1, based on the JCPDS-International Centre for Diffraction Data (Nos. 19-0098 and 78-0135). All peaks belong to the phase of *W*-type barium ferrite and no impure phases are observed. Thus, all samples are single phase with *W*-type hexagonal structure.

Based on the results of XRD measurement, the crystal planes with strong diffraction and their corresponding *d*-spacing values can be determined. Using these *d*-spacing values for the crystal planes of (1 1 0), (1 0 10), (1 1 6), (2 0 4), (2 0 8), (2 1 10), (3 0 6), (3 0 7) and (2 2 0), lattice parameters *a* and *c* were calculated by least squares method. The calculated results are given in Fig. 4-2 and Table 4-1.

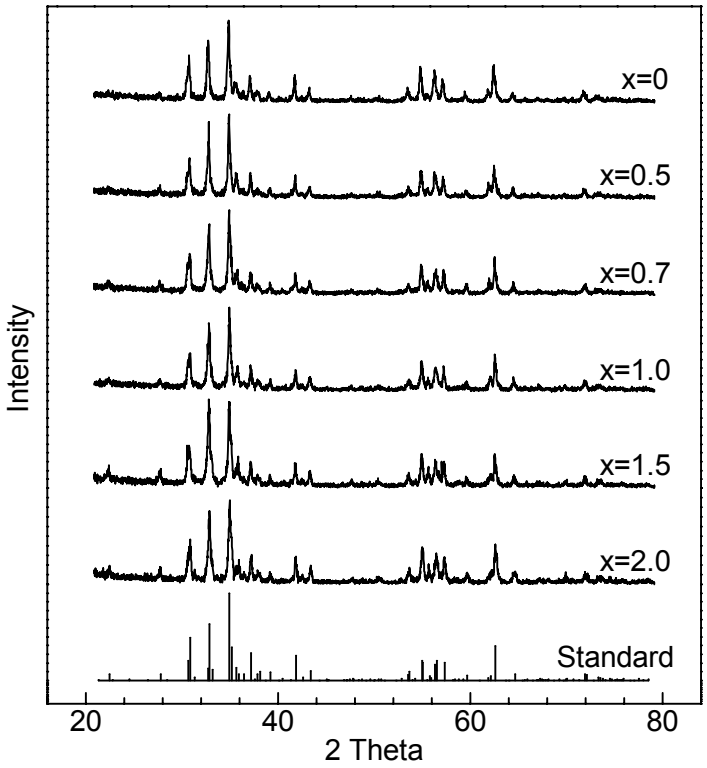

Fig. 4-1. X-ray diffraction patterns for powders of $BaCo_xZn_{2-x}Fe_{16}O_{27}$ with x=0, 0.5, 0.7, 1.0, 1.5 and 2.0.

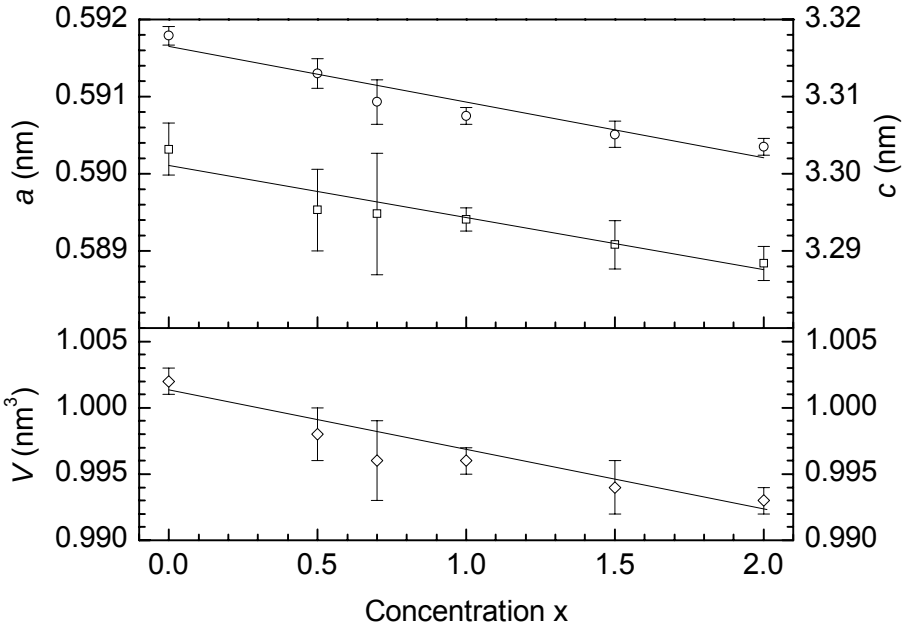

Fig. 4-2. The dependence of lattice parameters, *a* and *c*, as well as cell volume *V* on Co concentration x for $BaCo_xZn_{2-x}Fe_{16}O_{27}$ with x=0, 0.5, 0.7, 1.0, 1.5 and 2.0.

Table 4-1. Lattice parameters for $BaCo_xZn_{2-x}Fe_{16}O_{27}$ with various x.

x	*a* (nm)	*c* (nm)	*c*/*a*	*V* (nm^3)
0.0	0.5918 (1)	3.303 (3)	5.581 (4)	1.002 (4)
0.5	0.5913 (2)	3.295 (5)	5.572 (7)	0.998 (7)
0.7	0.5909 (3)	3.295 (8)	5.576 (11)	0.996 (10)
1.0	0.5908 (1)	3.294 (2)	5.575 (2)	0.996 (3)
1.5	0.5905 (2)	3.291 (3)	5.573 (3)	0.994 (5)
2.0	0.5904 (1)	3.288 (2)	5.569 (2)	0.993 (3)

It is obvious that the lattice parameters *a* and *c* decrease linearly from 0.5918 (1) to 0.5904 (1) nm, and from 3.303 (3) to 3.288 (2) nm, respectively, as $BaCo_xZn_{2-x}Fe_{16}O_{27}$ is changed from Zn_2W ($BaZn_2Fe_{16}O_{27}$) to Co_2W ($BaCo_2Fe_{16}O_{27}$). This is due to relatively small ionic radius of Co^{2+} (0.65 Å), as compared with that of Zn^{2+} (0.74 Å).[90] As a result, the cell volume of barium ferrite, *V*, decreases with the substitution of Co^{2+}. The ratio of *c*/*a* seems to decrease slightly with the Co concentration, except the sample with x=0.5.

4.1.2 Patterns for aligned samples

In order to verify the type of the magnetocrystalline anisotropy, XRD for aligned samples were also conducted. Some typical XRD patterns are shown in Fig. 4-3. For the aligned samples with x=0 and 0.5, the strong diffracted lines are found to be at 2θ angles of 21.5 º, 27.0 º. 32.2 º and 55.6 º, which correspond to the crystal planes of (0 0 8), (0 0 10), (0 0 12) and (0 0 20), respectively. Furthermore, the relative intensity of these lines increases from 4 %, 5 %, 12 % and 10 % for the unaligned samples to 50 %, 60 %, 100 % and 56 %, respectively. This implies that the grains are aligned along

c-axis ([0 0 1] direction). In addition, some weak lines at 2θ of 32.3 º and 34.6 º, corresponding the (1 0 10) and (1 0 11) plane, are also observed, because the directions of [1 0 10] and [1 0 11] only deviate by about 0.1 º from the *c*-axis. On the other hand, for the aligned samples with x ≥ 0.7, the intensity of the (*h k* 0) reflection increases dramatically, whereas the intensity of other reflections almost vanishes. This indicated that the grains are well aligned along the [1 1 0] direction.

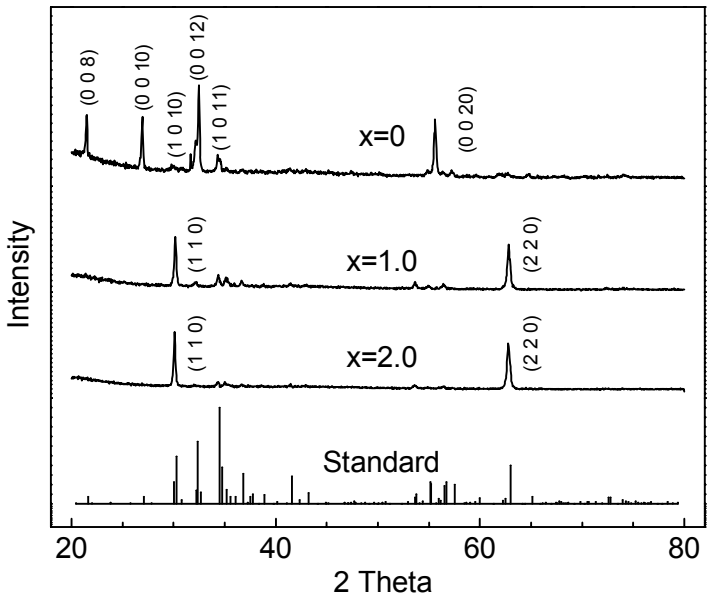

Fig. 4-3. Some typical XRD patterns for aligned samples of $BaCo_xZn_{2-x}Fe_{16}O_{27}$.

For an aligned sample, the easy magnetization direction should be along the applied magnetic field (normal to the surface of samples), due to free rotation of the particles during preparation. Therefore, the X-ray diffraction patterns of aligned samples show that the easy magnetization directions are along the *c*-axis for samples with x ≤ 0.5, while the easy directions are in the (0 0 1) plane or *c*-plane for samples with x ≥ 0.7.

4.2 Static magnetic properties

4.2.1 Coercivity H_c and saturation magnetization M_s

The magnetization curves and *M-H* loops were measured with applied fields of 0-80 kOe and between -30 and +30 kOe, respectively, at room temperature for all sintered samples using VSM. The demagnetizing corrections have been considered. The demagnetizing factor depends on the shape of samples. The sintered samples have a shape of cylinder with diameter of about 4 mm and thickness of 1.5-1.8 mm. Normally, the samples were measured along the direction perpendicular to the direction of thickness. Thus, the demagnetizing factors are about 0.1-0.2.

The magnetization curves are shown in Fig. 4-4 for all sintered samples. It is observed that the dependence of $M(H)$ on H is highly linear in the high-field region from 50 to 80 kOe. Hence, the values of M_s and χ_p were obtained on a linear least squares fitting. Let's take the sample with x=0.7 for example. There is a linear relationship between M and H in the range of 50-80 kOe, and the linear-fitted equation is given by $M(H) = 85.27 + 0.038H$, as shown in the inset of Fig.4-4. Based on Eq. 3-12, M_s and χ_p were determined to be 85.27 emu/g and 0.038 emu/g·kOe, respectively. With this method, the high-field susceptibility for samples with x=0, 0.5, 1.0, 1.5 and 2.0 are estimated at 0.053, 0.045, 0.029, 0.032 and 0.030 emu/g·kOe, respectively.

The saturation magnetization M_s, as a function of x, is plotted in Fig. 4-5. With the increase in Co substitution, M_s is found to increase first, reach a smooth maximum at x=0.7, and then decrease. This behavior can be explained as follows.

Zn^{2+} ions prefer tetrahedral sites ($4f_{IV}$ and 4e) with spin-down. Therefore,

nonmagnetic Zn ions occupying these sites decrease the negative magnetization, and thus leading to an increase in the total magnetization. On the other hand, Co^{2+} ions preferentially occupy the 6g site with spin-up and $4f_{VI}$ site with spin-down, which have the octahedral structure.[91] The occupancy of Co^{2+} at the 6g and $4f_{VI}$ sites can lead to an increase or decrease in the net magnetization, respectively.[92] Paoluzi *et al.* have indicated that the different distribution of Co^{2+} and Zn^{2+} at seven sites can give rise to discrepancy up to 20 % in the saturation magnetization.[93]

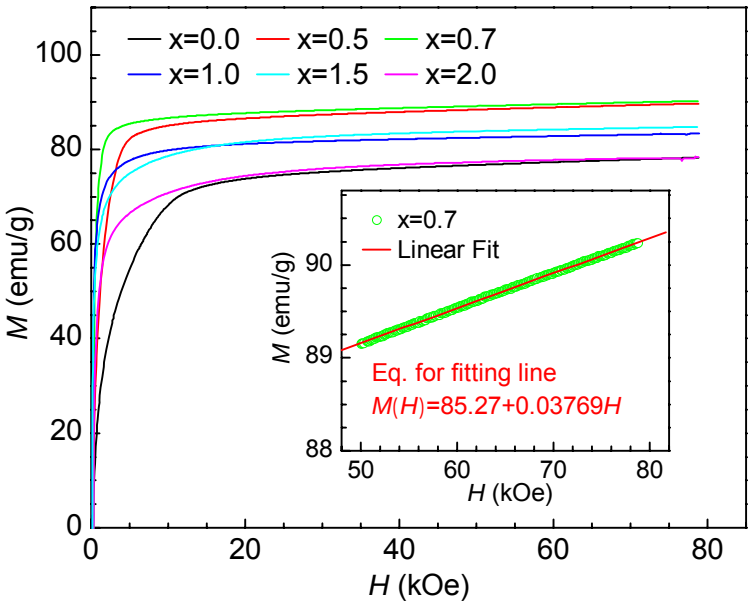

Fig. 4-4. Magnetization curves for all sintered samples. (Inset) Linear fitting result of magnetization curve in the range of 50-80 kOe for the sample with x=0.7.

Coercivity H_c was obtained from the *M*-*H* loop, as described in Section 2.4.3. The dependence of the coercivity H_c on the substituted amount x is shown in Fig. 4-5. With the increase in Co concentration, the coercivity reduces rapidly from 184 Oe for x=0 to about 15 Oe for x=0.7. The result is attributed to a decrease in the anisotropy field H_a, and a change in the anisotropy from *c*-axis to *c*-plane. With further substitution, the coercivity H_c increases slowly to 75 Oe for x=2.0. This is due to an

increase in the *c*-plane anisotropy. The change of magnetocrystalline anisotropy with the substitution will be reported in the following section.

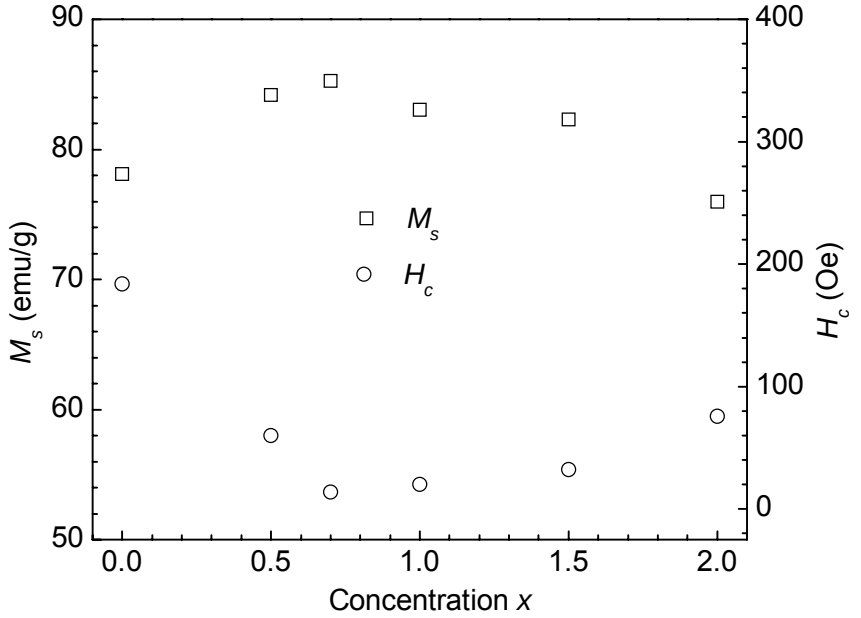

Fig. 4-5. The saturation magnetization M_s and coercivity H_c for $BaCo_xZn_{2-x}Fe_{16}O_{27}$ with various substituted amounts x.

4.2.2 Anisotropy field

For ferrites of $BaCo_xZn_{2-x}Fe_{16}O_{27}$, there are two types of anisotropy, *c*-axis anisotropy and *c*-plane anisotropy, which are associated with the easy magnetization along the *c*-axis and in the *c*-plane, respectively. For *c*-axis anisotropy, the magnetic field required for rotation of magnetization vectors from $[001]$ to $[00\bar{1}]$ direction is defined as the anisotropy field H_a. On the other hand, for *c*-plane anisotropy, there are two ways for magnetization vectors rotating from one to another easy magnetization direction, through the *c*-axis or in the *c*-plane. The corresponding magnetic fields required are defined as anisotropy fields H_θ (out-of-plane) and H_ϕ (in-plane), respectively.

As introduced in Chapter 3, the anisotropy field H_θ and H_a can be determined by two methods as follows.

Method A

The initial magnetization curves under applied fields of 0-80 kOe are measured by vibrating sample magnetometer (VSM) along two directions, which are parallel and perpendicular to the aligned direction, for all aligned samples. All samples are demagnetized before measurement. The demagnetizing corrections have been considered. Fig. 4-6 shows the magnetization curves, as an example, for the aligned sample with x=1.5. The field corresponding to the intersection of the two curves is the anisotropy field H_a for samples with *c*-axis anisotropy or H_θ for samples with *c*-plane anisotropy. The values of H_a and H_θ are shown by open circles in Fig. 4-7.

Method B

The anisotropy field H_a can also be obtained based on the law of approach to saturation (Eq. 3-9). For sintered samples, the relationship between M and $1/H^2$ can be determined from the magnetization curve of $M(H)$, as shown in Figs. 4-8a and 8b. It is found that there is a good linear relationship between $M(H)$ and $1/H^2$ within the range of H=11-20 kOe for x=0 and 4-11 kOe for x=0.5. Therefore, the terms of A/H and χ_p can be neglected. The value of B can be determined by the slope of the straight line. For the sample with x=0, the equation of the straight line is

$$M(H) = 75.50 - \frac{705.55}{H^2} = 75.50(1 - \frac{9.35}{H^2}).$$

Thus, with the value of B, the anisotropy field H_a can be calculated by $H_a = \sqrt{-15B} = \sqrt{-15 \times (-9.35)} = 11.8$ kOe. Similarly, the anisotropy field for x=0.5

can be obtained by $H_a = \sqrt{-15 \times (-1.12)} = 4.1$ kOe. Both values were shown by open squares in Fig. 4-7. It is clear that the values are consistent with the results obtained from the initial magnetization method (represented by the circles).

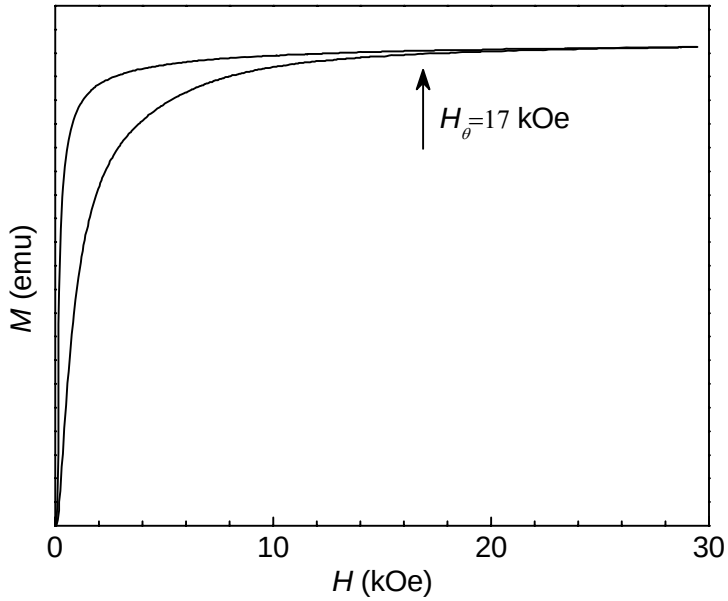

Fig. 4-6. The magnetization curves parallel and perpendicular to the alignment direction for the aligned sample of $BaCo_xZn_{2-x}Fe_{16}O_{27}$ with x=1.5.

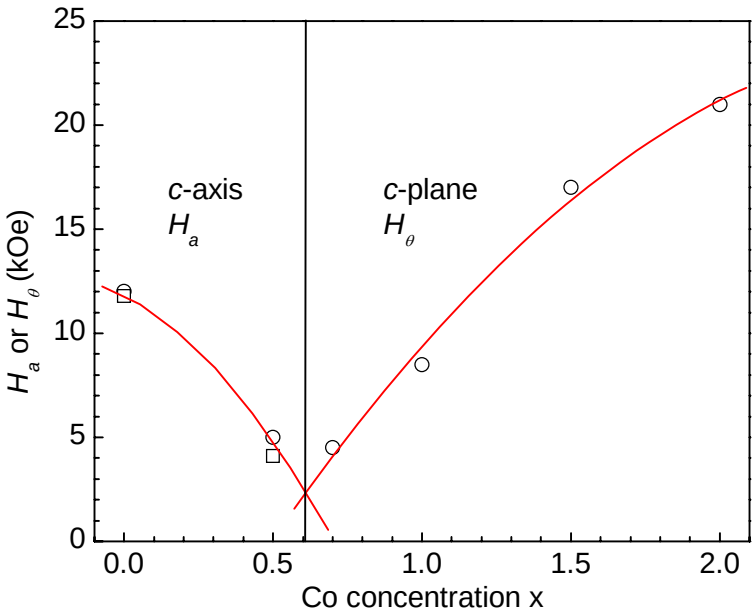

Fig. 4-7. Anisotropy field H_a or H_θ for $BaCo_xZn_{2-x}Fe_{16}O_{27}$ with various substituted amounts x. The open circles represent the values determined by initial magnetization curves for aligned samples and the open squares are values estimated by the magnetization curves for normal sintered samples.

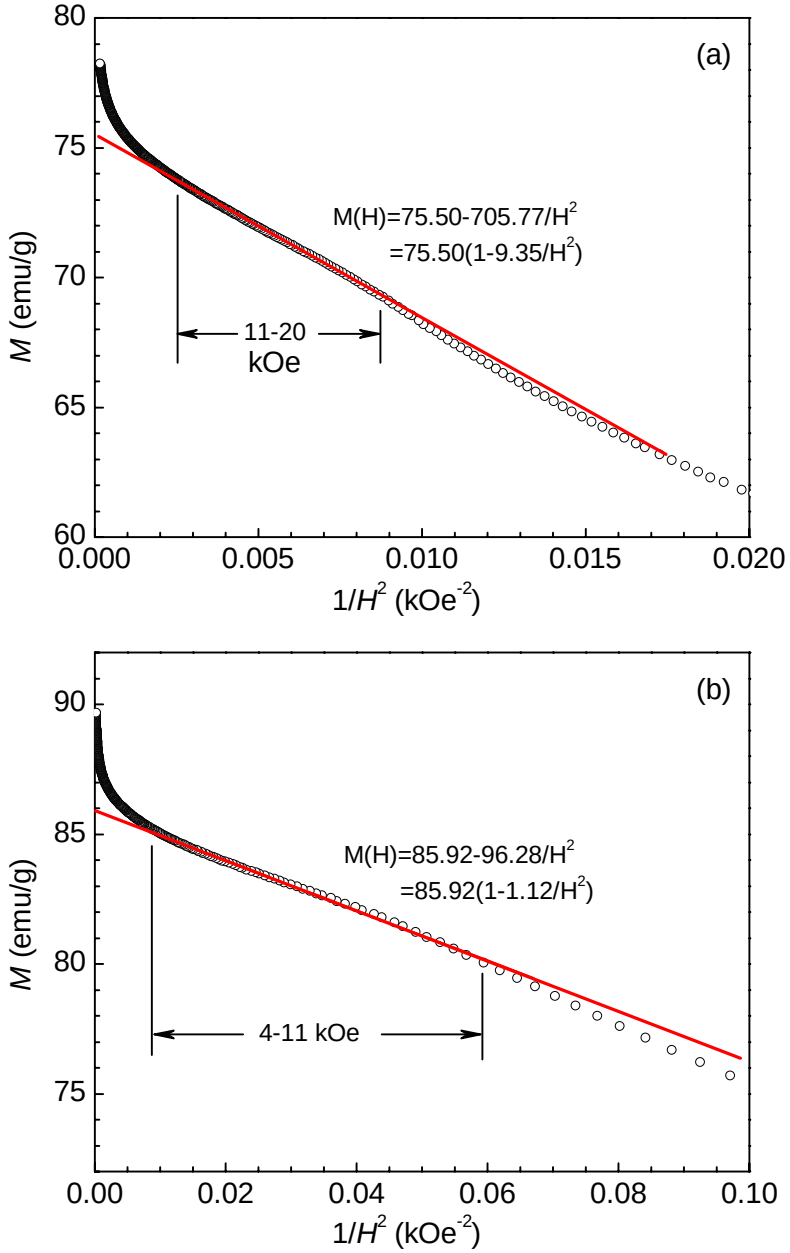

Fig. 4-8. The relationship between M and $1/H^2$ for the sintered samples of $BaCo_xZn_{2-x}Fe_{16}O_{27}$ with x=0 and 0.5. The straight lines are the linear-fitting results in the range of 11-20 kOe for x=0 and 4-11 kOe for x=0.5.

As the Co substitution increases, the value of H_a decreases rapidly from 12.0 (11.8) kOe for x=0 to 5.0 (4.1) kOe for x=0.5. Further Co substitution modifies the anisotropy from *c*-axis to *c*-plane. The value of H_θ increases from 4.5 kOe for x=0.7

to 21 kOe for x=2.0. It is known that, for *W*- and *Z*-type ferrites, most of divalent ions, such as Zn^{2+}, Fe^{2+} and Ni^{2+}, lead to easy *c*-axis anisotropy, but Co^{2+} can modify the anisotropy from *c*-axis to *c*-plane.[28, 94, 95, 96] Albanese *et al*.[30] have shown that Co^{2+} ions have negative contribution to the first order magnetocrystalline anisotropy constant K_1 and positive contribution to the second order anisotropy constant K_2. On the other hand, Zn^{2+} ions tend to contribute to *c*-axis anisotropy. Due to the competition between these two kinds of contribution, the anisotropy is modified from *c*-axis to *c*-plane with the increase in Co concentration.

4.3 Electromagnetic properties

4.3.1 Permittivity and permeability spectra

The complex permittivity ($\varepsilon = \varepsilon' - j\varepsilon''$) and permeability ($\mu = \mu' - j\mu''$) of the composites filled with 35 vol% ferrite powders were simultaneously characterized from 0.5 to 16.5 GHz using a VNA at room temperature. In addition, the complex permeability over 0.1-1.8 GHz was measured using an impedance/material analyzer.

The spectra of complex permittivity are shown in Fig. 4-9. It is obvious that the values of complex permittivity do not show observable dependence on the Co substituted amount x. For all composites, the real part ε' and imaginary part ε'' remain almost constant over the investigated frequency range. ε' varies slightly from 6.4 at 0.5 GHz to 5.9 at 16.5 GHz, while ε'' is about 0.3-0.5 over the whole frequency range.

The spectra of complex permeability over 0.1-16.5 GHz are shown in Fig. 4-10 for the composites with various substituted amounts x.

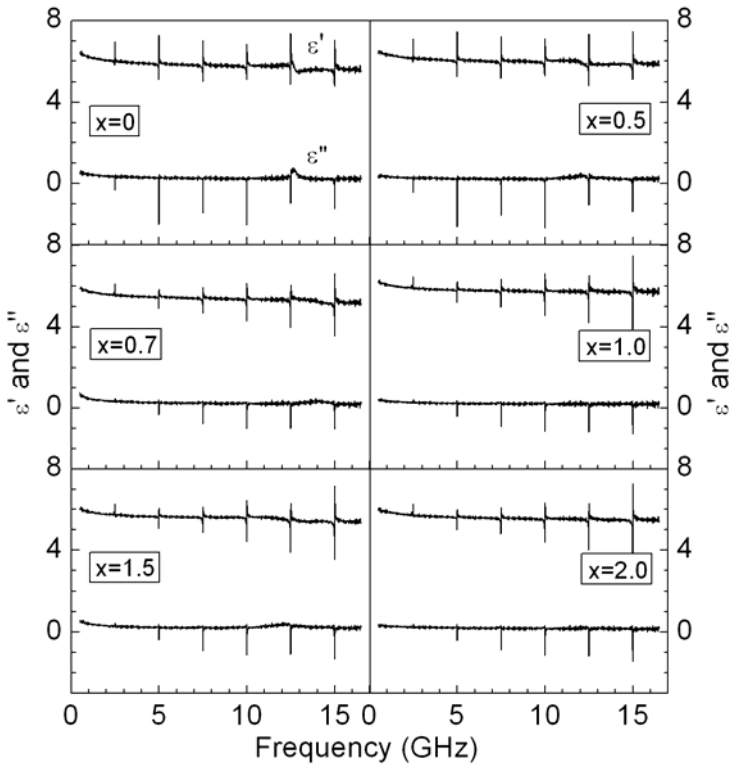

Fig. 4-9. The complex permittivity ε' and ε'' from 0.5 to 16.5 GHz for $BaCo_xZn_{2-x}Fe_{16}O_{27}$ composites with x=0, 0.5, 0.7, 1.0, 1.5 and 2.0.

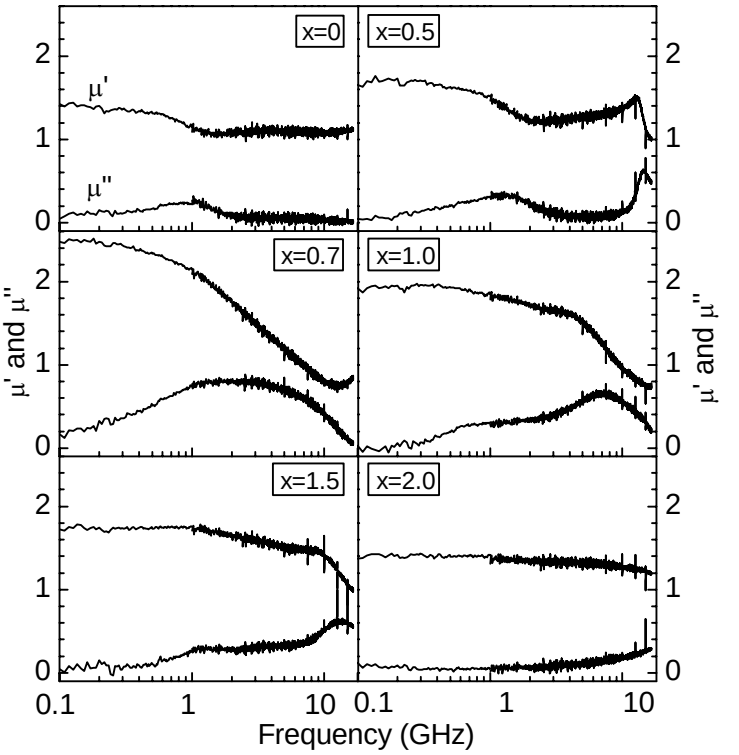

Fig. 4-10. The complex Permeability μ′ and μ″ from 0.1 to 16.5 GHz for $BaCo_xZn_{2-x}Fe_{16}O_{27}$ composites with x=0, 0.5, 0.7, 1.0, 1.5 and 2.0.

There are one obvious resonance peak for the samples of x=0 and 2.0, and two resonance peaks for the others. In general, for polycrystalline ferrites under an *ac* field, there are two types of resonance mechanism, natural resonance and domain wall resonance.[43] Many experiments and analyses have shown that the natural resonance is located at higher frequency than the domain wall resonance.[97] Hence, based on Fig. 4-10, the resonance mechanism for each peak can be identified. We define the frequency corresponding to the maximum value of μ" as the resonance frequency f_r. The resonance frequencies for domain wall and natural resonance were estimated and listed in Table 4-2, indicated as $f_{r,W}$ and $f_{r,N}$, respectively.

It is obvious that the domain wall resonance occurs at around 1 GHz for the composites with x=0-1.5 and disappears for the sample of x=2.0. The disappearance of the domain wall resonance should result from the Co substitution. It has been confirmed that Co ions can effectively suppress the motion of domain wall. Therefore, the domain wall resonance disappears for the sample with the maximum Co substitution. It should be noted that, although there is only one broad peak observable for the sample of x=0.7, based on the tendency of the peak shift, it is reasonable to regard this peak as the partial superposition of two resonance peaks.

Different from the domain wall resonance, the frequency of the natural resonance is greatly modified with the substituted amount x. For the sample of x=0 and 2.0, $f_{r,N}$ is beyond 16.5 GHz, which can not be exactly determined due to the limitation of investigated frequency. However, for the sample of x=0.7, the natural resonance frequency shifts to low frequency, and two resonances are partially overlapped with each other. Due to the superposition of two peaks, it is difficult to estimate the

resonance frequency $f_{r,N}$. In this case, the natural resonance is supposed to locate at about 2-3 GHz. The variation of the natural resonance frequency is induced by the change of anisotropy field. The detailed discussion about the relationship between the natural resonance frequency and the anisotropy field will be shown in the following section.

In addition, the values of $\mu_0^{'}$, $\mu_{\max,W}^{''}$ and $\mu_{\max,N}^{''}$ are also listed in Table 4-2. The real part of permeability at 0.1 GHz is defined as the static permeability $\mu_0^{'}$. $\mu_{\max,D}^{''}$ and $\mu_{\max,N}^{''}$ are the maximum values of imaginary permeability for domain wall and natural resonances, respectively. The static permeability $\mu_0^{'}$ is about 1.4 and 1.7 for the samples of x=0 and 0.5, respectively. When the anisotropy is modified from *c*-axis to *c*-plane at x=0.7, the value of $\mu_0^{'}$ increases greatly to 2.5. With further substitution, $\mu_0^{'}$ reduces to 1.7 at x=1.5. For most samples, the values of maximum imaginary permeability almost keep constant; $\mu_{\max,W}^{''}$ is about 0.3 and $\mu_{\max,N}^{''}$ is about 0.6. The exceptional case is the sample with x=0.7, which should be due to the partial superposition of the resonances.

Table 4-2. Some important parameters of dynamic magnetic property for $BaCo_xZn_{2-x}Fe_{16}O_{27}$ composites.

x	$\mu_0^{'}$	$\mu_{\max,W}^{''}$	$\mu_{\max,N}^{''}$	$f_{r,W}$ (GHz)	$f_{r,N}$ (GHz)
0.0	1.4	0.26	--	1.0	> 16.5
0.5	1.7	0.34	0.61	1.2	14.3
0.7	2.5	0.81		~ 2.0	
1.0	1.9	0.30	0.65	1.1	7.1
1.5	1.7	0.29	0.62	1.2	12.8
2.0	1.4	--	--	--	> 16.5

4.3.2 Relationship between natural resonance frequency and anisotropy field

In the above discussion, it has been mentioned that the natural resonance frequency is significantly modified with the substituted amount x. The variation of natural resonance frequency is mainly contributed by the change of anisotropy field. This can be understood qualitatively based on Snoek's theory.[98]

For hexaferrites, the natural resonance frequency f_r can be expressed as

$$f_r = \frac{\gamma}{2\pi} H_a \text{ and} \qquad 4\text{-}1$$

$$f_r = \frac{\gamma}{2\pi} \left(H_\theta H_\phi \right)^{1/2} \qquad 4\text{-}2$$

for *c*-axis and *c*-plane anisotropy, respectively. The gyromagnetic ratio $\gamma/2\pi$ is equal to 2.8 MHz/Oe. In general, the anisotropy field H_a^2 is larger than the product of H_θ and H_ϕ, since H_ϕ is about a few hundreds Oersted.[97] Therefore, normally, the samples with *c*-axis anisotropy have high natural resonance frequency. For composites with *c*-axis anisotropy, f_r is about 14.3 GHz for ferrite with x=0.5 and far beyond 16.5 GHz for x=0. Based on anisotropy fields of 5 and 12 kOe, the predicted f_r is 14.0 and 33.6 GHz, respectively, which is well consisted with the experimental results.

Furthermore, it is also found that the natural resonance frequency f_r varies linearly with the anisotropy field H_θ for composites with *c*-plane anisotropy, as shown in Fig. 4-11. In the figure, the symbols of up- and down-triangle represent the case for BaM and BaZ ferrites, reported by Li *et al.*.[99] The data points can be well fitted by a line with the equation of

$$f_r = 0.77223 H_\theta . \qquad 4\text{-}3$$

Therefore, it is reasonable to assume that the anisotropy field H_ϕ is proportional to the field H_θ with a proportional coefficient β. Thus, Eq. 4-2 can be rewritten as

$$f_r = \beta^{1/2} \frac{\gamma}{2\pi} H_\theta . \qquad 4\text{-}4$$

Comparing Eq. 4-4 with Eq. 4-3, $\beta = 0.076$ is roughly obtained. Therefore, the values of H_ϕ are estimated at 0.34, 0.65, 1.3 and 1.6 kOe for samples with x=0.7, 1.0, 1.5 and 2.0, respectively. Paoluzi *et al.*[93] have observed that the magnitude of the third order magnetocrystalline anisotropy constant increases with Co substitution for $BaCo_xZn_{2-x}Fe_{16}O_{27}$, which predicts an increase in anisotropy field H_ϕ.

In addition, based on $H_\theta = 21$ kOe for Co_2W, $f_r = 16.2$ GHz can be derived from Eq. 4-3, which is also consistent with the experimental result, as shown in Fig. 4-10.

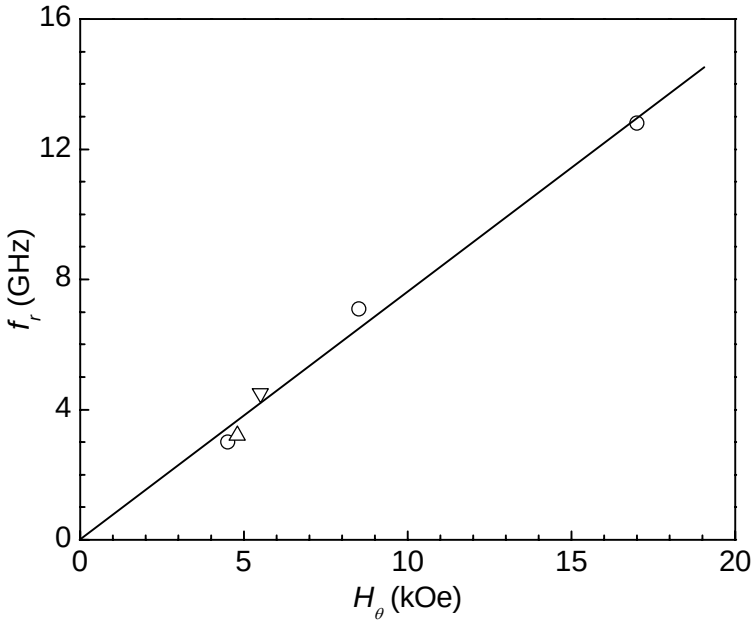

Fig. 4-11. The dependence of resonance frequency f_r on anisotropy field H_θ for composites of $BaCo_xZn_{2-x}Fe_{16}O_{27}$ with *c*-plane anisotropy. The symbols of up- and down-triangle are for BaM and BaZ ferrites. The straight line represents the linear fitting result with the function of $f_r = 0.77223 H_\theta$.

4.3.3 Fitting of complex permeability spectra

For polycrystalline ferrites in an *ac* field, the permeability is generally contributed by two different components, wall displacement permeability and magnetic moment rotation permeability.

According to the method of permeability spectra fitting (introduced in Section 3.3.5), the experimental permeability spectra are fitted over all measured frequencies. The measurement error is estimated as 5 % and the calculated Chi-square values are about 1.6-2.0. The curve-fitted results are shown in Fig. 4-12 and the fitted parameters are listed in Table 4-3. The calculated curves are fitted with the experimental data very well. The green lines are for domain wall resonance, the blue lines are for natural resonance, and the red lines represent the summation of these two components.

Based on the fitting curves and parameters for complex permeability, several important characteristics are observed for these composites.

(1). The static susceptibility χ_0 is greatly changed with Co substitution. For domain wall spectra, the values of χ_0 are 0.38, 0.45, 1.08, 0.34 and 0.26 for ferrites with x=0, 0.5, 0.7, 1.0 and 1.5. The contribution of wall displacement decreases with the increase in Co concentration from 0.7 to 1.5. For natural resonance, the values of χ_0 are 0.20, 0.63, 0.75 and 0.70 for ferrites with x=0.5, 0.7, 1.0 and 1.5.

(2). The dispersion type for natural resonance is modified as the anisotropy changes from *c*-axis to *c*-plane. For the composite with x=0.5, which is *c*-axis anisotropy, the damping coefficient λ is very small (0.16). Therefore, for this sample, the natural resonance is typical resonance-type. However, for other composites with *c*-plane

anisotropy, λ is about 0.7-0.9, which indicates a middle-type resonance.

(3). The intrinsic resonance frequency f_R is greatly changed with Co substitution. For natural resonance, the values of resonance frequency f_R are 14.9, 7.8, 9.5 and 17.1 GHz for the samples with x=0.5, 0.7, 1.0 and 1.5, respectively. For domain wall resonance, both f_R and f_{R1} increase with Co concentration, from 2.7 GHz and 0.64 GHz (x=0) to 4.0 GHz and 2.6 GHz(x=1.5), respectively.

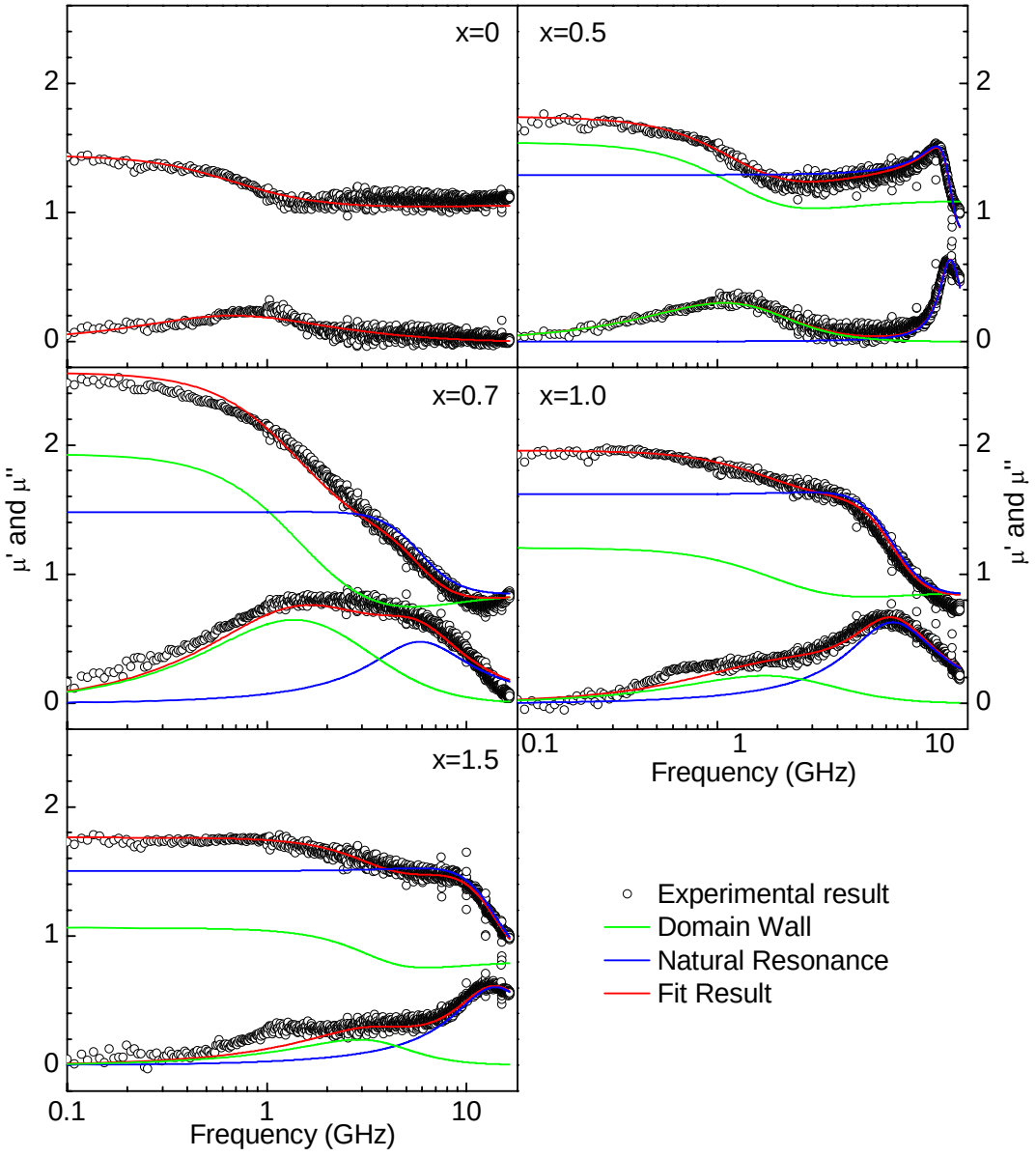

Fig. 4-12. The complex permeability spectra and their fitting curves for the composites of $BaCo_xZn_{2-x}Fe_{16}O_{27}$ with x varying from 0 to 1.5.

Table 4-3. The fitting parameters of the complex permeability spectra for composites of $BaCo_xZn_{2-x}Fe_{16}O_{27}$ with x varying from 0 to 1.5.

x	B	Domain Wall Resonance			Natural Resonance		
		$\chi_{0,W}$	f_R (GHz)	f_{R1} (GHz)	$\chi_{0,N}$	λ	f_R (GHz)
0	1.06	0.38	2.7	0.64	--	--	--
0.5	1.09	0.45	1.8	0.94	0.20	0.16	14.9
0.7	0.85	1.08	2.9	1.2	0.63	0.88	7.8
1.0	0.86	0.34	3.2	1.5	0.75	0.75	9.5
1.5	0.80	0.26	4.0	2.6	0.70	0.71	17.1

4.4 Microwave absorbing properties

The dependence of reflection loss (*RL*) on frequency has been calculated based on the metal-backed single-layer model. The method to predict the absorbing characteristics has been introduced in detail in Section 3.3.4.

With the experimental values of μ and ε for all composites of $BaCo_xZn_{2-x}Fe_{16}O_{27}$, *RL* at various *t* (varying from 1.0 to 6.0 mm at intervals of 0.1 mm) was calculated from a computer simulation. There is a poor absorbing ability for the samples of Co_2W and Zn_2W due to the low permeability; their calculated results will be neglected in the following discussion. Based on the calculated *RL* curves at various thickness, f_{up}, f_{low} and $W=f_{up}/f_{low}$ are determined for each thickness. Here, $RL \leq -10$ dB is regarded as ideal absorbing condition. Fig. 4-13 shows the dependence of f_{up}, f_{low} and W on thickness *t* for each composite. The absorbing properties with maximum relative bandwidth W_{max} are shown in Fig. 4-14.

For the sample of x=0.5, the frequency band for ideal absorption is about 13.5-16.5 GHz with *t* varying from 1.5 to 2.1 mm. Due to the limitation of measured frequency,

the absorption performance over 16.5 GHz is unknown and the upper-frequency limit, f_{up}, can not be estimated exactly. For simplicity, in this case, the value for f_{up} is taken as 16.5 GHz. Therefore, the maximum relative bandwidth W_{max} is about 1.25 and the optimum thickness t_o is 1.9 mm. As shown by the red line in Fig. 4-14, the minimal reflection loss RL_{min} is obtained as -19.3 dB. The frequency corresponding to RL_{min} is about 15.1 GHz, which is slightly larger than the natural resonance frequency of 14.3 GHz.

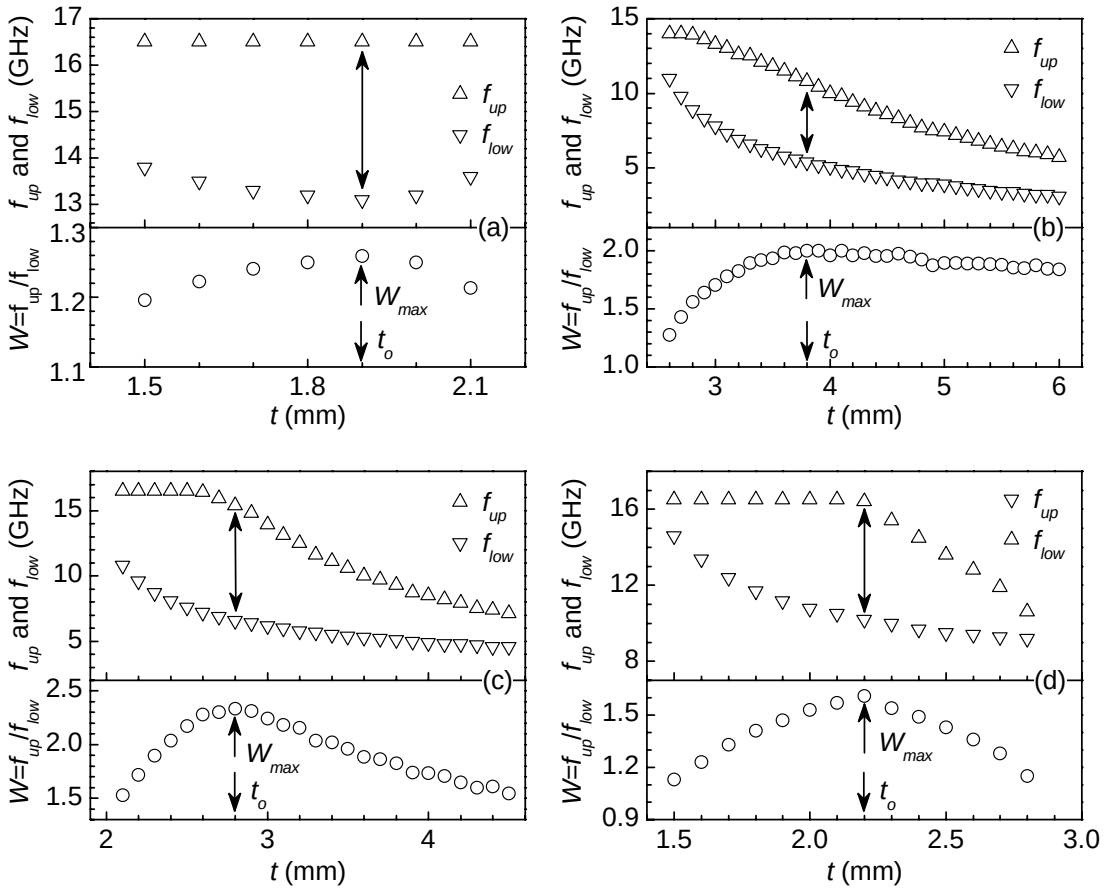

Fig. 4-13. The dependence of f_{up}, f_{low} and $W=f_{up}/f_{low}$ on thickness t for composites of $BaCo_xZn_{2-x}Fe_{16}O_{27}$: (a) x=0.5, (b) x=0.7, (c) x=1.0 and (d) x=1.5.

For the sample of x=0.7, with t varying from 2.6 to 6.0 mm, the frequency band for ideal absorption is changed greatly. The frequency band for more than 10 dB

absorption is 11.0-14.1 GHz at t=2.6 mm, and 3.1-5.7 GHz at t=6.0 mm. The maximum relative bandwidth W_{max} is 2.0 and the optimum thickness t_o is 3.8 mm. The corresponding f_{up} and f_{low} are 10.8 and 5.4 GHz, respectively. The minimum reflection loss RL_{min} is obtained as -31.1 dB and the corresponding frequency is 7.9 GHz.

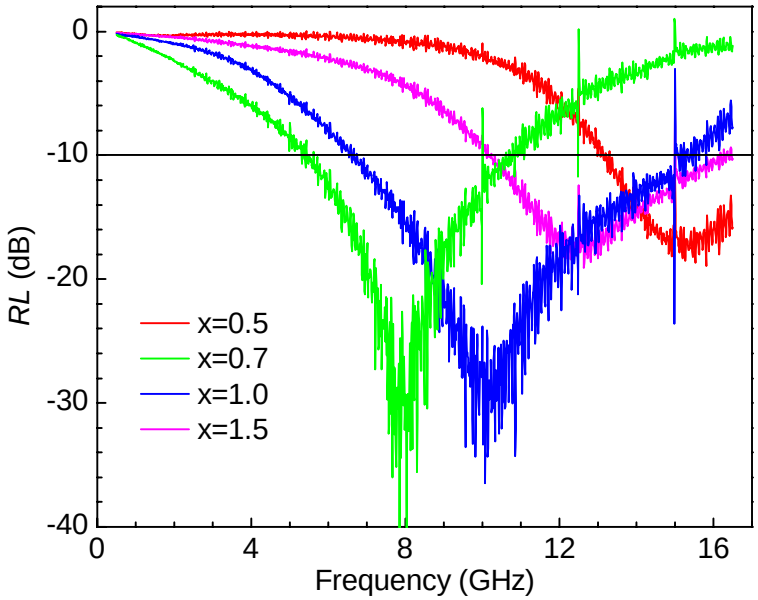

Fig. 4-14. Reflection characteristics at the optimum thickness t_o for composites of $BaCo_xZn_{2-x}Fe_{16}O_{27}$ with x=0.5, 0.7, 1.0 and 1.5.

Similar as the sample of x=0.7, the perfect absorbing frequency band is also changed significantly with the thickness t for x=1.0. As shown in Fig. 4-13c, the frequency band is changed from 10.9-16.5 GHz to 4.6-7.1 GHz with t increasing from 2.1 to 4.5 mm. The maximum relative bandwidth W_{max} is obtained as 2.33 at t=2.8 mm, the corresponding f_{up} and f_{low} are 15.4 and 6.6 GHz, respectively. The minimum reflection loss RL_{min} is obtained as -29.2 dB and the corresponding frequency is 10.2 GHz.

For the sample of x=1.5, with t varying from 1.5 to 2.6 mm, f_{up} and f_{low} are modified from over 16.5 to 12.8 GHz and from 14.6 to 9.4 GHz, respectively. At the optimum

thickness t_o=2.2 mm, the maximum relative bandwidth W_{max} is about 1.61 and the corresponding f_{up} and f_{low} are 16.4 and 10.2 GHz, respectively. As shown by the magenta line in Fig. 4-14, the minimal reflection loss RL_{min} is obtained as -17.6 dB. The frequency corresponding to RL_{min} is about 12.3 GHz.

With the above discussion, it is obvious that the composites of x=0.7 and 1.0 are potential candidates for EM materials with low reflectivity and broad bandwidth covering C-band (4-8 GHz) and X-band (8-12 GHz). The composites of x=0.5 and 1.5 are suitable for use in Ku-band (12-18 GHz).

4.5 Conclusions

CoZn-substituted BaW ferrites, $BaCo_xZn_{2-x}Fe_{16}O_{27}$ with x=0, 0.5, 0.7, 1.0, 1.5 and 2.0, have been synthesized by the solid-state reaction. The static and dynamic magnetic properties have been studied. The main results are listed as follows: (1). Co ions are able to modify the anisotropy of BaW ferrites from *c*-axis to *c*-plane at x=0.5-0.7. (2). The natural resonance frequency f_r is closely associated with the anisotropy fields. For *c*-plane anisotropy, as the Co concentration x increases from 0.7 to 2.0, the anisotropy field H_θ increases from 4.5 to 20 kOe, while the resonance frequency f_r shifts from about 2 to >16.5 GHz. Therefore, the desired f_r for EM materials can be achieved by controlling Co concentration. (3). For *c*-plane anisotropy, the static permeability $\mu_0^{'}$ and the maximum imaginary permeability $\mu_{\max}^{''}$ increase with Zn concentration. For composites with 35 vol% BaW ferrite powders, $\mu_0^{'}$ and $\mu_{\max}^{''}$ are 1.7 and 0.29 at Zn concentration of 0.5, while increase to 2.5 and 0.81 at Zn concentration of 1.3, respectively. (4). The predicted *RL* indicates that the composites of x=0.7 and 1.0 are the potential candidates for EM materials covering C-band and

X-band. The frequency bands for $RL \leq -10$ dB are from 5.4 to 10.8 GHz at thickness of 3.8 mm and from 6.6 to 15.4 GHz at thickness of 2.8 mm for composites of x=0.7 and 1.0, respectively.

CHAPTER 5: ABSORBING PERFORMANCE FOR COMPOSITES WITH VARIOUS FERRITE CONCENTRATIONS

In the previous chapter, it has been reported that hexaferrites of $BaCo_xZn_{2-x}Fe_{16}O_{27}$ with x=0.7 and 1.0 are potential candidates for EM absorbing materials. During that work, all composites were filled by 35 vol% of ferrite powders and 65 vol% of epoxy resin. In this chapter, the dependence of high-frequency electromagnetic and microwave absorbing properties on the ferrite volume concentration V_c will be reported in detail. The magnetic fillers are $BaCo_xZn_{2-x}Fe_{16}O_{27}$ (x=0.7 and 1.0) powders, and V_c is varied from 25 to 50 %.

5.1 EM property for epoxy resin

The composite samples were fabricated by mixing fine powders of ferrite with epoxy resin; thus, the electromagnetic property of composites is tightly dependent on the intrinsic property of magnetic fillers and the corresponding concentration. Meanwhile, the electromagnetic properties of epoxy resin also play an important role.

Figure 5-1 shows the complex permittivity and permeability spectra for epoxy resin. Ignore the abnormal peaks in permittivity spectra due to measurement error, the permittivity and permeability are almost independent of frequency in the whole testing range. As expected, the real and imaginary permeabilities are 1 and 0, respectively, due to nonmagnetic property. The measured values of real and

imaginary permittivity are about 3.4 and 0.4 at 0.5 GHz, while 2.9 and 0.2 at 16.5 GHz, respectively. The slight variation of complex permittivity with frequency may be induced by measurement uncertainty instead of the intrinsic property in materials. The reported values of ε' and ε'' for epoxy resin #618 is 2.95 and 0.12,[100] as indicated by red lines. It is obvious that the measured results and the reported values agree very well.

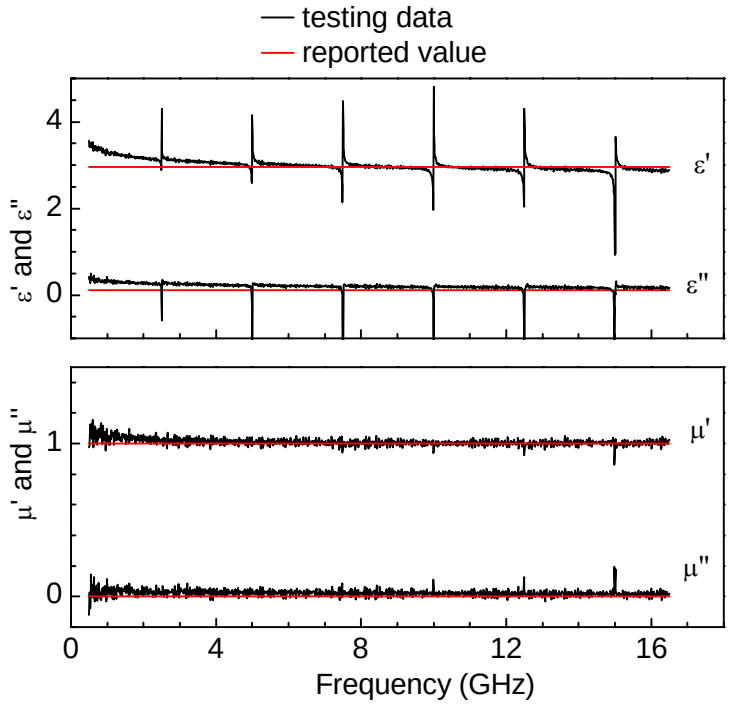

Fig. 5-1. The complex permittivity and permeability spectra for epoxy resin in the range of 0.5-16.5 GHz.

5.2 Effect of V_c on electromagnetic property

5.2.1 Permittivity spectra

Figure 5-2 shows the real and imaginary permittivity (ε' and ε'') spectra for composites of $BaCo_{0.7}Zn_{1.3}Fe_{16}O_{27}$ with ferrite volume concentration of V_c=25, 35, 40 and 50 %.

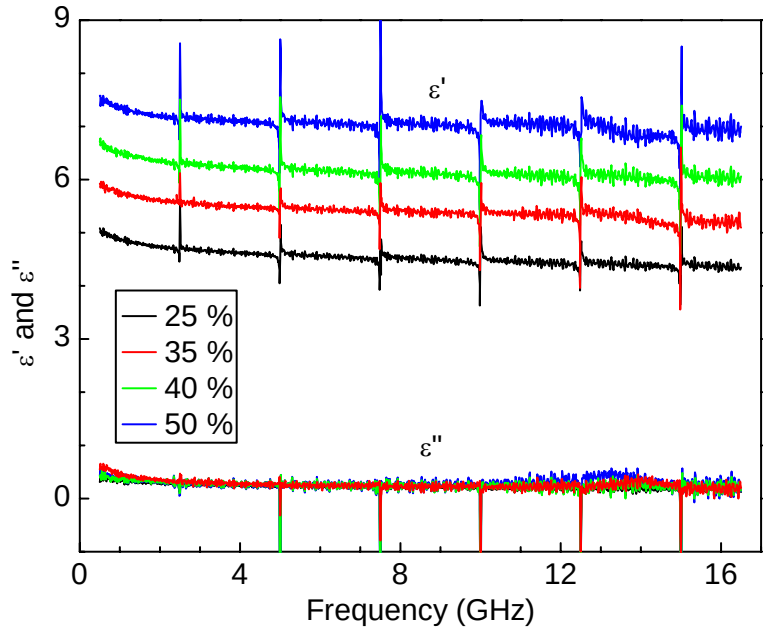

Fig. 5-2. The complex permittivity spectra for composites of $BaCo_{0.7}Zn_{1.3}Fe_{16}O_{27}$ with various volume concentration (V_c=25, 35, 40 and 50 %) in the range of 0.5-16.5 GHz.

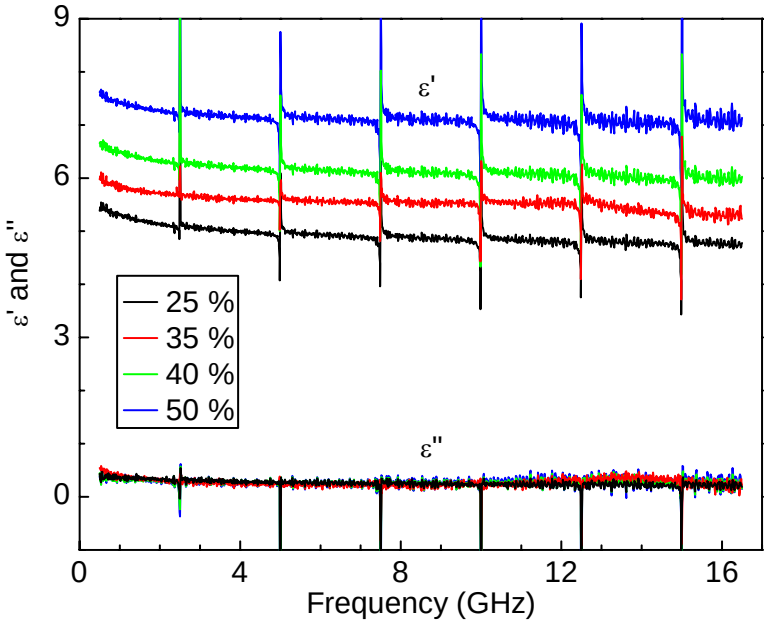

Fig. 5-3. The complex permittivity spectra for composites of $BaCoZnFe_{16}O_{27}$ with various volume concentration (V_c=25, 35, 40 and 50 %) in the range of 0.5-16.5 GHz.

For a given V_c, the complex permittivity remains almost constant over the investigated frequency of 0.5-16.5 GHz. For example, ε' varies slightly from 7.5 at 0.5 GHz to 6.9

at 16.5 GHz, while ε" is about 0.2-0.3 over the whole frequency range for the composite with V_c=50 %. On the other hand, as V_c decreases from 50 to 25 %, the real permittivity ε' decreases, while the imaginary part ε'' keeps almost constant. At the frequency of 0.5 GHz, the values of ε' are 7.5, 6.7 5.9 and 5.0 for V_c=50, 40, 35 and 25 %, respectively.

Figure 5-3 shows the permittivity spectra for composites of $BaCoZnFe_{16}O_{27}$ with various V_c. A similar behavior is observed in composites of $BaCo_{0.7}Zn_{1.3}Fe_{16}O_{27}$. For a specific V_c, the complex permittivity remains constant over the investigated frequency of 0.5-16.5 GHz. As V_c varies from 50 to 25 %, the real permittivity ε' decreases, while the imaginary part ε" keeps almost constant. At the frequency of 0.5 GHz, ε' is 7.5, 6.6, 5.9 and 5.5 for V_c=50, 40, 35 and 25 %, respectively.

5.2.2 Permeability spectra

The spectra of complex permeability are shown in Fig. 5-4 for composites of $BaCo_{0.7}Zn_{1.3}Fe_{16}O_{27}$ with ferrite volume concentration of V_c=25, 35, 40 and 50 %. Several high-frequency magnetic parameters are listed in Table 5-1. μ_0', the static permeability, is defined as the real permeability at 0.1 GHz, μ_{max}'' is the maximum imaginary permeability, and f_r is the corresponding frequency, which is named as resonance frequency. As discussed in Chapter 4, essentially, there should be two resonance peaks in the permeability spectra for BaW composites. However, due to the near location, these two peaks are overlapped and cannot be clearly distinguished from each other. For simplicity, they are regarded as one broad resonance peak, which is contributed by domain wall and natural resonances.

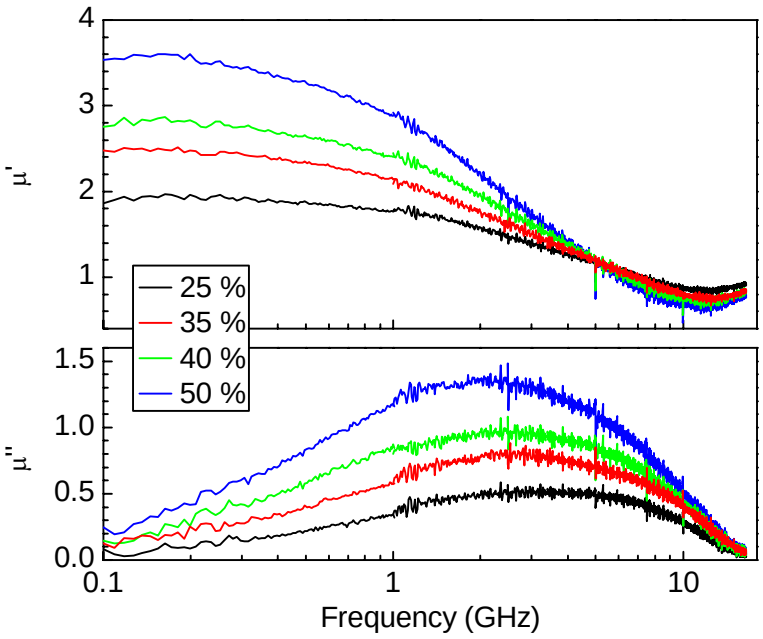

Fig. 5-4. The complex permeability spectra for composites of $BaCo_{0.7}Zn_{1.3}Fe_{16}O_{27}$ with various volume concentration (V_c=25, 35, 40 and 50 %) in the range of 0.1-16.5 GHz.

Table 5-1. Dynamic magnetic properties for composites of $BaCo_{0.7}Zn_{1.3}Fe_{16}O_{27}$ with various volume concentration V_c.

V_c (%)	25	35	40	50
$\mu_0^{'}$	1.9	2.4	2.8	3.6
$\mu_{max}^{"}$	0.5	0.8	1.0	1.4
f_r (GHz)	3.0	2.6	2.4	2.1

With increasing volume concentration V_c, both $\mu_0^{'}$ and $\mu_{max}^{"}$ are rapidly increased. As V_c changes from 25, 35, 40 to 50 %, $\mu_0^{'}$ increases from 1.9, 2.4, 2.8 to 3.6, and $\mu_{max}^{"}$, from 0.5, 0.8, 1.0 to 1.4, respectively. The corresponding resonance frequency f_r is slightly shifted to lower frequency, from 3.0, 2.6, 2.4 to 2.1 GHz.

The spectra of complex permeability are shown in Fig. 5-5 for composites of $BaCoZnFe_{16}O_{27}$ with various V_c. The values for high-frequency parameters are listed

in Table 5-2. Similarly, with increasing volume concentration V_c, both $\mu_0^{'}$ and $\mu_{max}^{''}$ rapidly increase. As V_c changes from 25 to 50 %, $\mu_0^{'}$ increases from 1.8 to 3.1 and $\mu_{max}^{''}$, from 0.5 to 1.2. The corresponding frequency f_r is shifted to lower frequency, from 7.2 to 5.7 GHz.

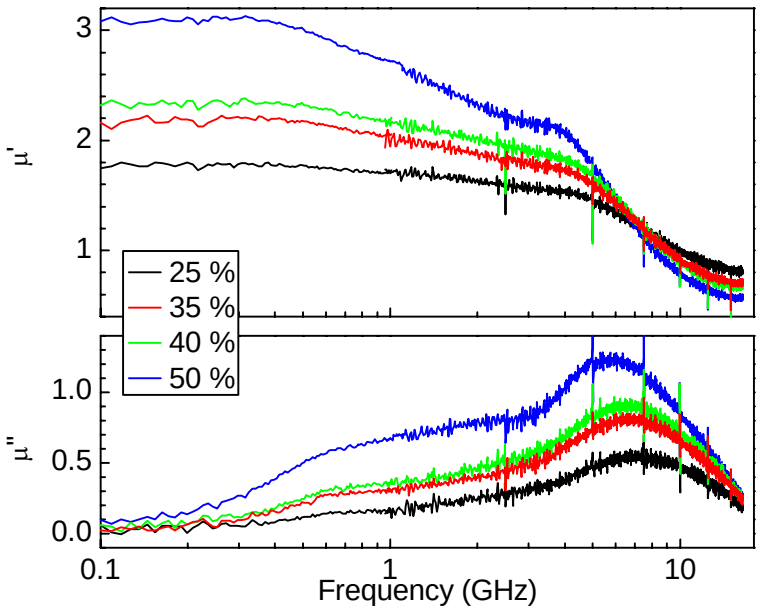

Fig. 5-5. The complex permeability spectra for composites of $BaCoZnFe_{16}O_{27}$ with various V_c (25, 35, 40 and 50 %) in the range of 0.1-16.5 GHz.

Table 5-2. Dynamic magnetic properties for composites of $BaCoZnFe_{16}O_{27}$ with various volume concentration V_c.

V_c (%)	25	35	40	50
$\mu_0^{'}$	1.8	2.2	2.4	3.1
$\mu_{max}^{''}$	0.5	0.8	0.9	1.2
f_r (GHz)	7.2	6.8	6.5	5.7

5.3 Effect of V_c on microwave absorption

5.3.1 Absorbing bandwidth

RL with various thickness *t* (varying from 1.0 to 6.0 mm at intervals of 0.1 mm) was calculated using the values of μ and ε for all composites of $BaCo_{0.7}Zn_{1.3}Fe_{16}O_{27}$. For $RL = -10$ dB, the dependence of upper- and lower-frequency limits (f_{up} and f_{low}), and relative bandwidth ($W=f_{up}/f_{low}$) on *t* is shown in Fig. 5-6.

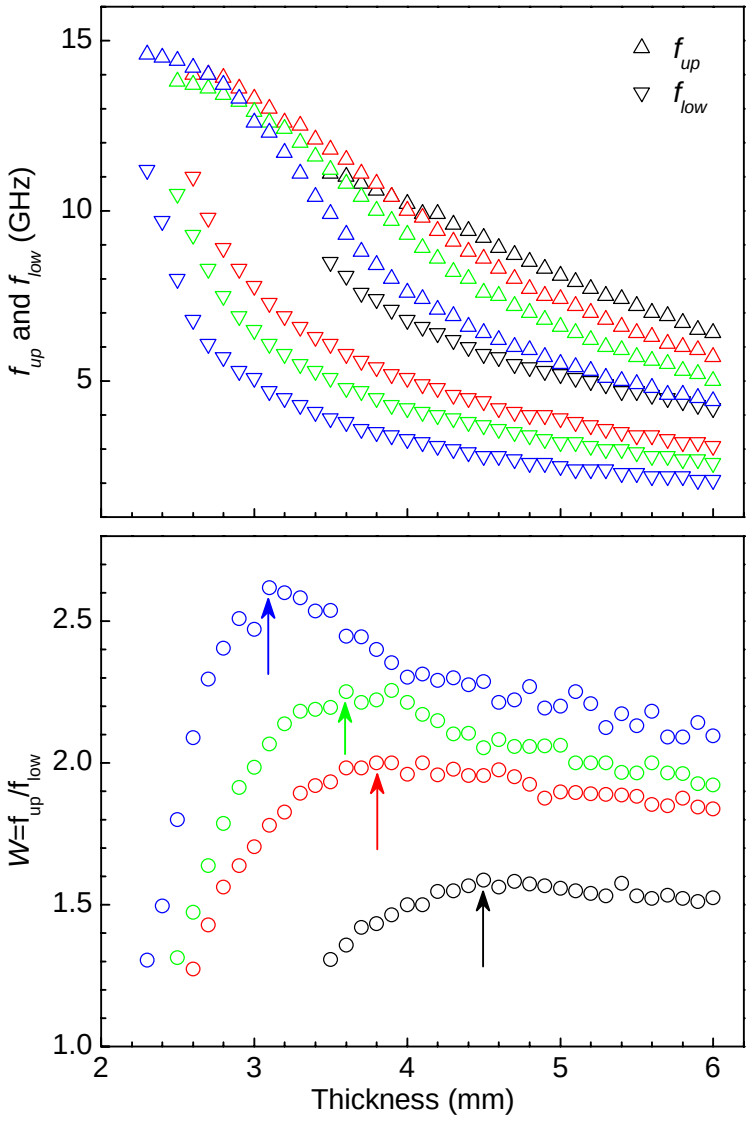

Fig. 5-6. The dependence of f_{up}, f_{low} and *W* on *t* for composites of $BaCo_{0.7}Zn_{1.3}Fe_{16}O_{27}$ with various V_c: black symbols are for V_c =25 %, red for 35 %, green for 40 % and blue for 50 %.

It is obvious that, for each composite, the upper- and lower-frequency limits, f_{up} and f_{low}, are shifted to lower frequency with the increase in thickness t. Let's take the composite with V_c=35 % for example. As thickness t changes from 2.6 to 6.0 mm, f_{up} and f_{low} rapidly decrease from 14.0 to 5.7 GHz and from 11.0 to 3.1 GHz, respectively.

Three characteristics are observed for the relative bandwidth W. (1) For the composite with a given V_c, W increases first, reaches a maximum and then decreases with increasing thickness of the composites. (2) The maximum relative bandwidth, W_{max}, is enhanced with the increase in V_c. W_{max} increases from 1.6 to 2.6 with the change of V_c from 25 to 50 %. (3) The thickness corresponding to W_{max}, optimum thickness t_o, decreases with V_c, from 4.5 mm at V_c=25 % to 3.1 mm at V_c=50 %.

Figure 5-7 shows the frequency dependence of the reflection loss at optimum thickness t_o for the composites with various V_c. In addition, according to the densities of ferrite particles (ρ_f=5.3 g/cm^3) and epoxy resin (ρ_e=1.1 g/cm^3), the optimum weight of unit area, m_o, can be calculated for the composite with a given V_c. based on the following equation,

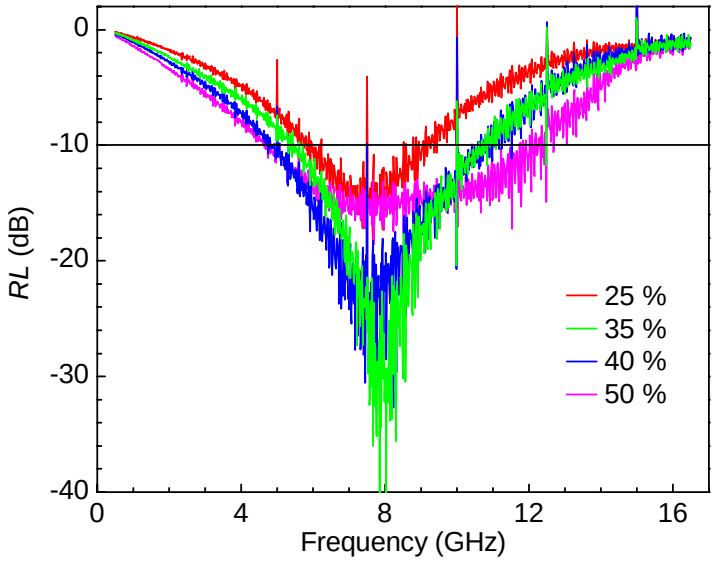

Fig. 5-7. Reflection characteristics at the optimum thickness for composites of $BaCo_{0.7}Zn_{1.3}Fe_{16}O_{27}$ with various V_c.

Table 5-3. The optimum thickness t_o, the upper- and lower-frequency limits, f_{up} and f_{low}, for absorption of more than 10 dB, and the maximum relative bandwidth of W_{max} for composites of $BaCo_{0.7}Zn_{1.3}Fe_{16}O_{27}$ with various V_c.

V_c (%)	f_{low} (GHz)	f_{up} (GHz)	W_{max}	t_o (mm)	m_o (g/cm^2)
25	5.8	9.2	1.59	4.5	0.97
35	5.4	10.8	2.00	3.8	0.98
40	4.8	10.8	2.25	3.6	1.00
50	4.7	12.3	2.62	3.1	0.99

$$m_o = \rho_c t_o = [\rho_f V_c + \rho_e (1 - V_c)] t_o , \qquad 5\text{-}1$$

where ρ_c is the density of composite. The calculated m_o, as well as f_{up}, f_{low} and W_{max}, is listed in Table 5-3. It can be seem that, with the change of V_c from 25 to 50 %, m_o slightly increases from 0.97 to 0.99 g/cm^2, while W_{max} is significantly improved from 1.6 to 2.6. Therefore, the composite with larger V_c shows better microwave absorbing performance.

Similarly, *RL* at various thickness *t* was calculated for the composites of $BaCoZnFe_{16}O_{27}$ with V_c=25, 35, 40 and 50 %. The dependence of f_{up}, f_{low} and relative bandwidth *W* on thickness *t* for each composite is shown in Fig. 5-8. The reflection properties with maximum relative bandwidth are shown in Fig. 5-9. The values of f_{up}, f_{low}, W_{max}, t_o and the corresponding m_o are listed in Table 5-4. The influence of V_c on the absorbing properties is almost same as the case of $BaCo_{0.7}Zn_{1.3}Fe_{16}O_{27}$. The increase in V_c contributes to the improvement of absorbing properties. For the composite with V_c=50 %, the maximum relative bandwidth is obtained as about 2.8 with f_{up} and f_{low} of 16.2 and 5.8 GHz, respectively. It should be noted that, for the composite with high V_c and small *t*, such as V_c=50 % and $t \leq 2.3$ mm, f_{up} is beyond 16.5 GHz and cannot be determined exactly. Thus, f_{up} is roughly regarded as 16.5 GHz.

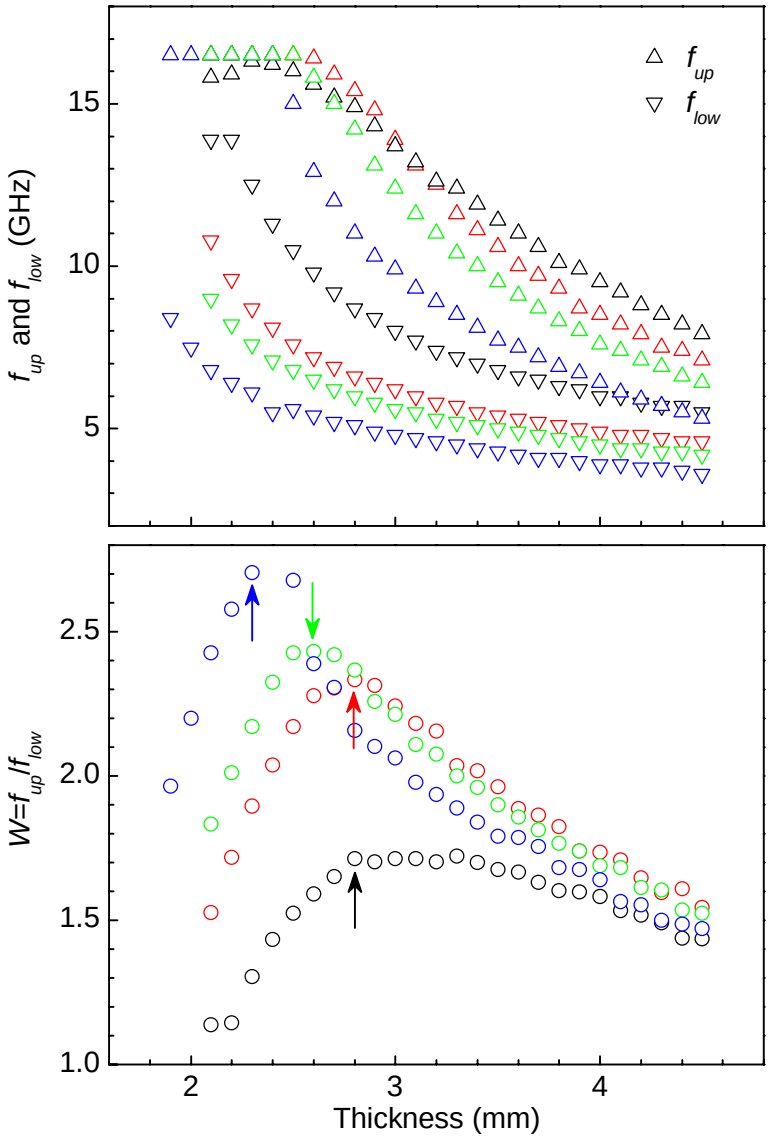

Fig. 5-8. The dependence of f_{up}, f_{low} and W on t for composites of $BaCoZnFe_{16}O_{27}$ with various V_c: black symbols are for V_c =25 %, red for 35 %, green for 40 % and blue for 50 %.

In addition, based on Tables 5-3 and 5-4, it is obvious that the composites of $BaCoZnFe_{16}O_{27}$ have better absorbing properties than those of $BaCo_{0.7}Zn_{1.3}Fe_{16}O_{27}$; the former have larger W_{max} and smaller m_o. Let's take the sample with V_c=25 % for example. W_{max} is about 1.6 with m_o of 0.97 g/cm^2 for $BaCo_{0.7}Zn_{1.3}Fe_{16}O_{27}$; while, for $BaCoZnFe_{16}O_{27}$, W_{max} is about 1.7 and m_o is 0.71 g/cm^2.

According to the above discussions, it can be concluded that the composites with a high ferrite volume concentration have more suitable properties for microwave absorption. However, the flexibility is worse with the increase in V_c, and it is very difficult to fabricate composites with ferrite concentration larger than 60 %. In the following study, the volume concentration of ferrite particles for all composites will be fixed as 50 %.

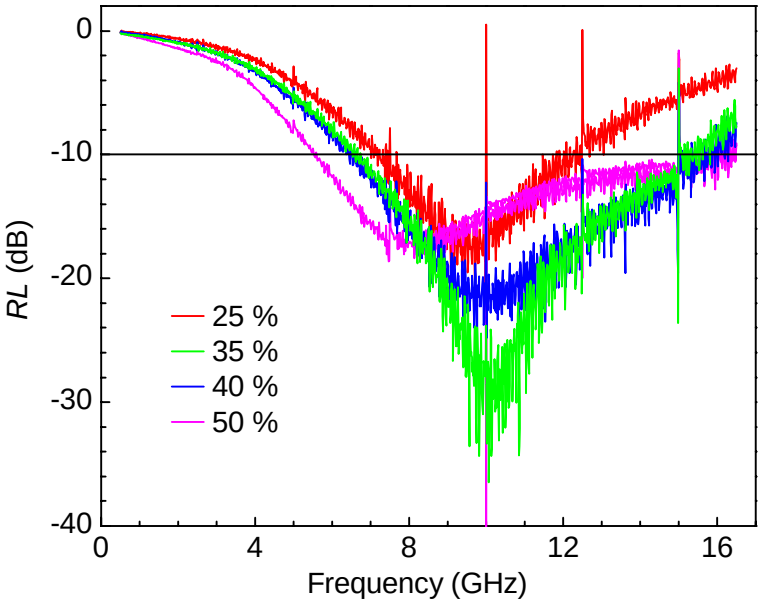

Fig. 5-9. Absorbing characteristics at the optimum thickness for composites of $BaCoZnFe_{16}O_{27}$ with various V_c.

Table 5-4. The optimum thickness t_o, the upper- and lower-frequency limits, f_{up} and f_{low}, for absorption of more than 10 dB, and the maximum relative bandwidth of W_{max} for composites of $BaCoZnFe_{16}O_{27}$ with various V_c.

V_c (%)	f_{low} (GHz)	f_{up} (GHz)	W_{max}	t_o (mm)	m_o (g/cm^2)
25	7.2	12.4	1.72	3.3	0.71
35	6.6	15.4	2.33	2.8	0.72
40	6.5	15.8	2.43	2.6	0.72
50	5.5	16.5	3.00	2.4	0.77

5.3.2 Matching property

Based on the calculated results of *RL* at various thickness *t*, the variations of the minimum reflection loss RL_{min} and the corresponding frequency $f_{RL\text{-}min}$ with thickness *t* for the composites of $BaCo_xZn_{2-x}Fe_{16}O_{27}$ are shown in Figs. 5-10 (x=0.7) and 5-11 (x=1.0). Here, t_m is the matching thickness, which is defined as the thickness at the minimum of RL_{min}. Once the matching thickness t_m is determined, the corresponding matching frequency f_m and the value of RL_{min} can be obtained from the curves of $f_{RL\text{-}min}$-*t* and RL_{min}-*t*, respectively. In Figs. 5-10 and 5-11, only one dip at t_m is found for the composites of x=0.7 with $V_c \leq 35$ % and x=1.0 with V_c=25 %, while double dips at t_{m1} and t_{m2} ($t_{m1}>t_{m2}$) for the others.

The existence of two matching frequencies f_{m1} and f_{m2} and matching thicknesses t_{m1} and t_{m2} has been verified by many researchers[85, 86] with the help of impedance matching solution map. Neito *et al.*[6] also pointed out that the matching frequency of ferrite absorber was higher than its resonance frequency.

Tables 5-5 and 5-6 list the values of t_m, f_m and RL_{min} for the composites of x=0.7 and 1.0, respectively. In addition, the resonance frequency, f_r, is also included in the table. The variation of the matching frequencies with ferrite volume concentration is shown in Fig. 5-12.

With the increase in V_c, the difference between the two matching frequencies f_{m1} and f_{m2} increases. For the composites of x=1.0, the matching frequencies f_{m1} decreases from 9.1 to 6.4 GHz, while f_{m2} increases from 14.7 to 16.5 GHz, as V_c varies from 35 to 50 %. For the composites of x=0.7, the difference between f_{m1} and f_{m2} is 4.9 and 9.1 GHz for V_c=40 and 50 %, respectively.

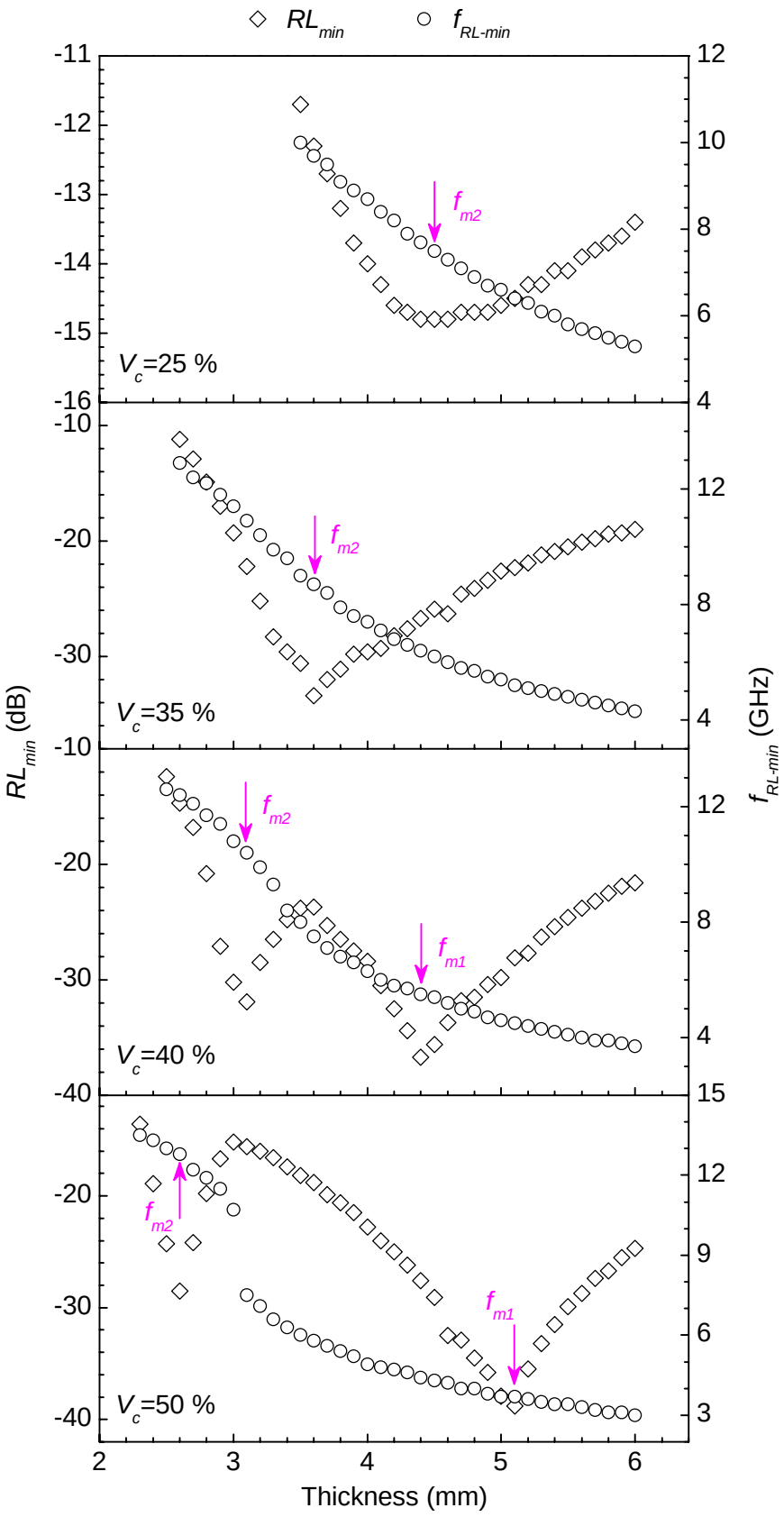

Fig. 5-10. The variations of the minimum reflection loss RL_{min} and the corresponding frequency $f_{RL\text{-}min}$ with sample thickness t for the composites of $BaCo_{0.7}Zn_{1.3}Fe_{16}O_{27}$.

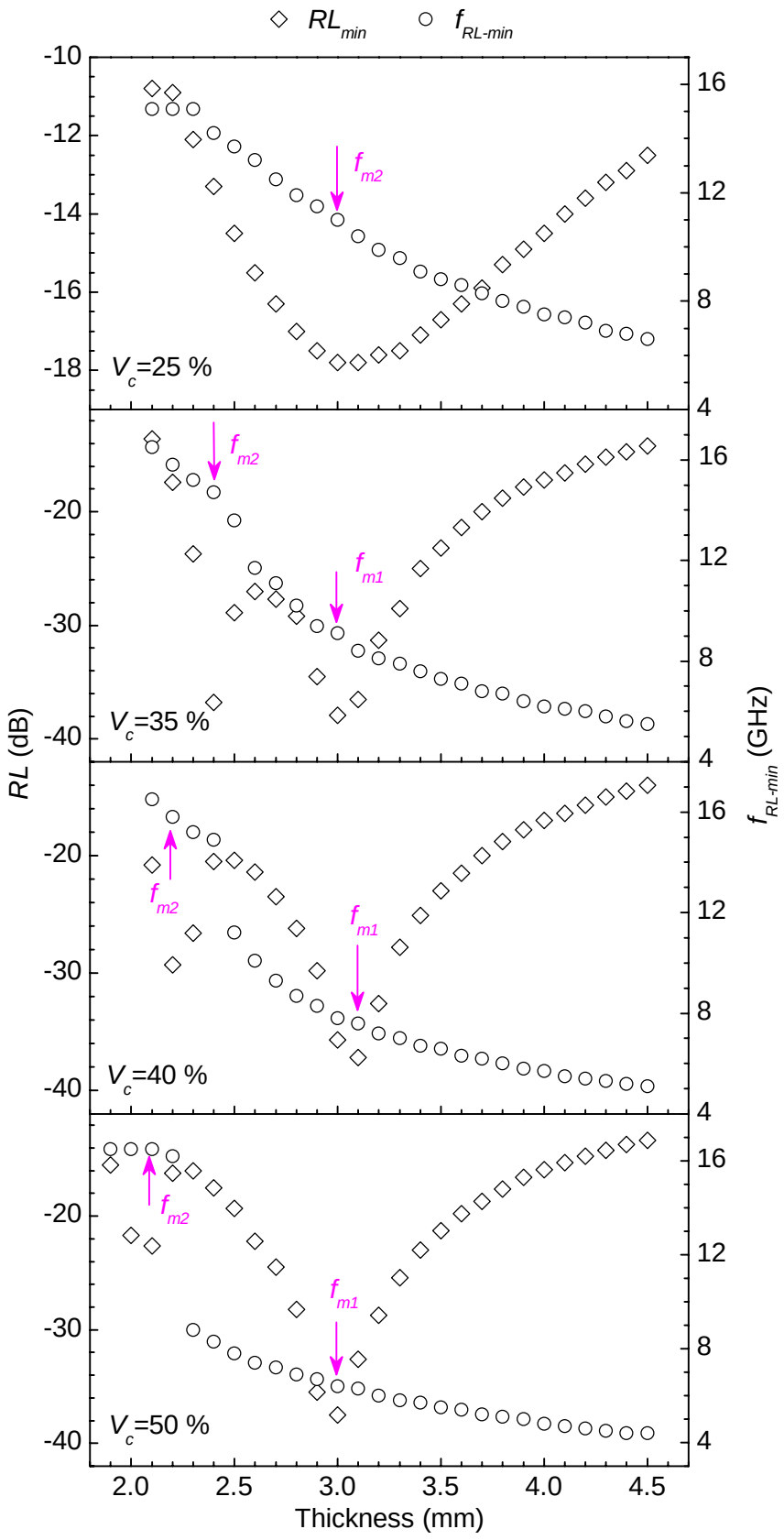

Fig. 5-11. The variations of the minimum reflection loss RL_{min} and the corresponding frequency $f_{RL\text{-}min}$ with sample thickness t for the composites of $BaCoZnFe_{16}O_{27}$.

Table 5-5. Matching thickness t_m, matching frequency f_m and the corresponding *RL* for composites of $BaCo_{0.7}Zn_{1.3}Fe_{16}O_{27}$ with various ferrite volume concentration.

V_c (%)	f_r (GHz)	First match			Second match		
		t_{m1} (mm)	f_{m1} (GHz)	*RL* (dB)	t_{m2} (mm)	f_{m2} (GHz)	*RL* (dB)
25	3.0	--	--	--	4.5	7.5	-14.8
35	2.6	--	--	--	3.6	8.7	-33.4
40	2.4	4.4	5.5	-36.7	3.1	10.4	-31.9
50	2.1	5.1	3.7	-38.8	2.6	12.8	-28.5

Table 5-6. Matching thickness t_m, matching frequency f_m and the corresponding *RL* for composites of $BaCoZnFe_{16}O_{27}$ with various ferrite volume concentration.

V_c (%)	f_r (GHz)	First match			Second match		
		t_{m1} (mm)	f_{m1} (GHz)	*RL* (dB)	t_{m2} (mm)	f_{m2} (GHz)	*RL* (dB)
25	7.2	--	--	--	3.0	11.0	-17.8
35	6.8	3.0	9.1	-37.9	2.4	14.7	-36.8
40	6.5	3.1	7.6	-37.2	2.2	15.8	-29.3
50	5.7	3.0	6.4	-37.5	2.1	16.5	-22.6

On the other hand, it is noticed that the first matching frequency f_{m1} is always close to the natural resonance frequency, and increases with the natural resonance frequency. The second matching frequency f_{m2} is far away from the resonance frequency. Therefore, it is reasonable to deduce that the first matching condition is associated with the magnetic resonance. The explanation for the second match is as follows.

It is well known that minimal reflection of the microwave power or matching condition occurs when the thickness *t* of the absorbers approximates an odd number multiple of a quarter of the propagating wavelength,

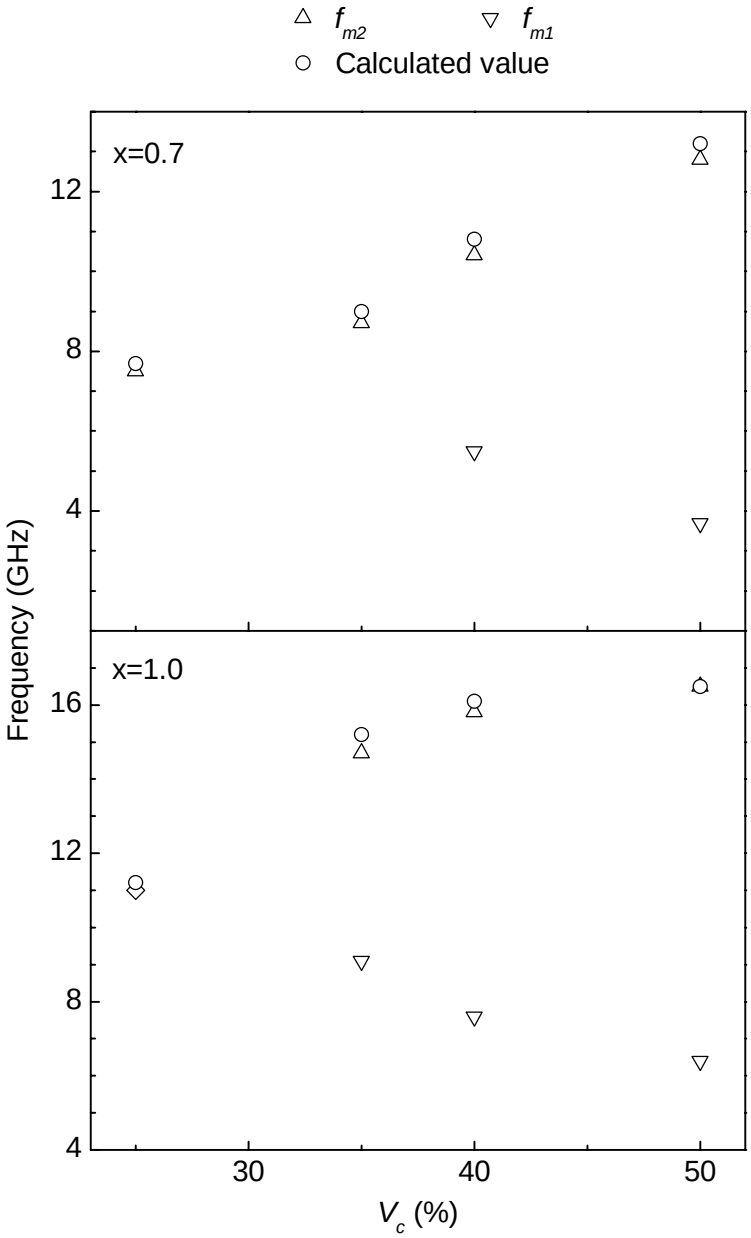

Fig. 5-12. Matching frequencies f_{m1} and f_{m2} for composites of $BaCo_xZn_{2-x}Fe_{16}O_{27}$ (x=0.7 and 1.0) with various ferrite volume concentration. The open circle represents the calculated value based on Eq. 5-2.

$$t = \frac{n\lambda_m}{4} = \frac{nc}{4f\,\mathrm{Re}\sqrt{\varepsilon\mu}}, \qquad 5\text{-}2$$

where t is the thickness of composite, λ_m is the EM wavelength in the composite

material, c is the light velocity, and $\mathrm{Re}\sqrt{\varepsilon\mu}$ is the real part of $\sqrt{\varepsilon\mu}$. n is a positive odd number and n=1 corresponds to the first dip of thickness loss, such as the second matching dip in Figs. 5-10 and 5-11. As shown in Figs. 5-2 and 5-3, for ferrite composites at microwave frequency, ε'' is much smaller than ε', thus $|\varepsilon| \approx \varepsilon'$. Therefore, the second matching frequency, f_{m2}, can be theoretically given by

$$f_{m2} = \frac{c}{4t_{m2}\sqrt{\varepsilon'}\,\mathrm{Re}\sqrt{\mu}}, \qquad 5\text{-}3$$

The calculated results of f_{m2} are plotted in Fig. 5-12 as open circles, which are well consistent with the experimental results.

In addition, for the composites of x=0.7 with V_c=25 and 35 % and x=1.0 with V_c=25 %, there is only one matching frequency, which is far from the resonance frequency. Hence, this match is assumed to result from thickness loss. The calculated values of f_m are also plotted in Fig. 5-12. The agreement of the calculated and experimental values confirmed this speculation. That is to say, for the composites with low volume concentration, magnetic loss is negligible and thickness loss is the major contribution of absorption.

5.4 Conclusions

The dependence of complex permittivity, permeability and microwave absorbing property on ferrite volume concentration V_c has been investigated for the composites of $BaCo_xZn_{2-x}Fe_{16}O_{27}$ with x=0.7 and 1.0. V_c varies from 25 to 50 %.

The complex permittivities, ε' and ε'', are frequency independent in 0.5-16.5 GHz. In the meantime, the value of ε' increases with the increase in V_c, while ε'' is almost

constant at various V_c. The dynamic magnetic properties are improved with the increase in V_c. For the composites of x=1.0, $\mu_0^{'}$ increases from 1.8 to 3.1, and $\mu_{max}^{''}$, from 0.5 to 1.2 with V_c changing from 25 to 50 %. The resonance frequency, f_r, shifts to lower frequency, from 7.2 to 5.7 GHz, as V_c changes from 25 to 50 %.

One or two impedance matching phenomena are observed. For the composites with two matching frequencies, the match at low frequency is contributed by magnetic loss and the other is produced by thickness loss. Thus, the first matching frequency is associated with the magnetic resonance frequency and the second one is independent of the resonance frequency. For the composites with low volume concentration, such as V_c=25 % for the composite of x=1.0, just one matching condition is observed. In this case, thickness loss is the major mechanism of absorption and magnetic loss is negligible.

With this work, it was found that composites filling with 50 vol% ferrite powders have excellent microwave absorbing performance with suitable flexibility and density. Therefore, the ferrite concentration for all composites investigated thereafter will be fixed as 50 vol%.

CHAPTER 6: EFFECT OF V_2O_5 DOPING ON MAGNETIC AND ABSORBING PROPERTIES FOR BaW

In Chapter 4, it has been reported that CoZn-substituted *W*-type barium ferrite is one of promising candidates for EM absorbing materials. A suitable amount of Co substitution can effectively modify the anisotropy from *c*-axis to *c*-plane. As the Co concentration increases from 0.7 to 2.0, the natural resonance frequency of composites can be controlled from 2 GHz to above 16.5 GHz. However, the values of complex permeability are still low.

To increase the complex permeability, the BaW ferrites ($BaCoZnFe_{16}O_{27}$) with various oxides doping, including CaO, CuO, MgO, Bi_2O_3, SiO_2, MnO_2, RuO_2, IrO_2, Nb_2O_5 and V_2O_5, have been investigated. The effect of various oxides doping was reported and analyzed in Appendix A of this thesis. It was found that the doping of V_2O_5 can significantly enhance the complex permeability. Therefore, in this chapter, we will focus on exploring the effect of V_2O_5 doping on the crystal structure, static and dynamic magnetic properties, and microwave absorbing properties for BaW.

6.1 Various amounts of V_2O_5 doping in $BaCoZnFe_{16}O_{27}$

6.1.1 Crystal structure

Figure 6-1 shows the XRD patterns for $BaCoZnFe_{16}O_{27}$ doped with 0, 0.5, 0.75, 1.0 and 1.5 wt% of V_2O_5. The standard position and intensity of the X-ray diffraction

lines for BaW are also given in the figure. All samples are found to be single phase; no other phases are detected. In addition, XRD for aligned samples was also carried out to identify the crystalline anisotropy and aligned status. The typical XRD pattern for aligned samples is shown in Fig. 6-1. The strong diffracted crystal planes are found to be (1 1 0) and (2 2 0). Therefore, the grains are well aligned along the [*i j* 0] directions. This indicated that all samples have *c*-plane anisotropy, which is consistent with the conclusion in Chapter 4.

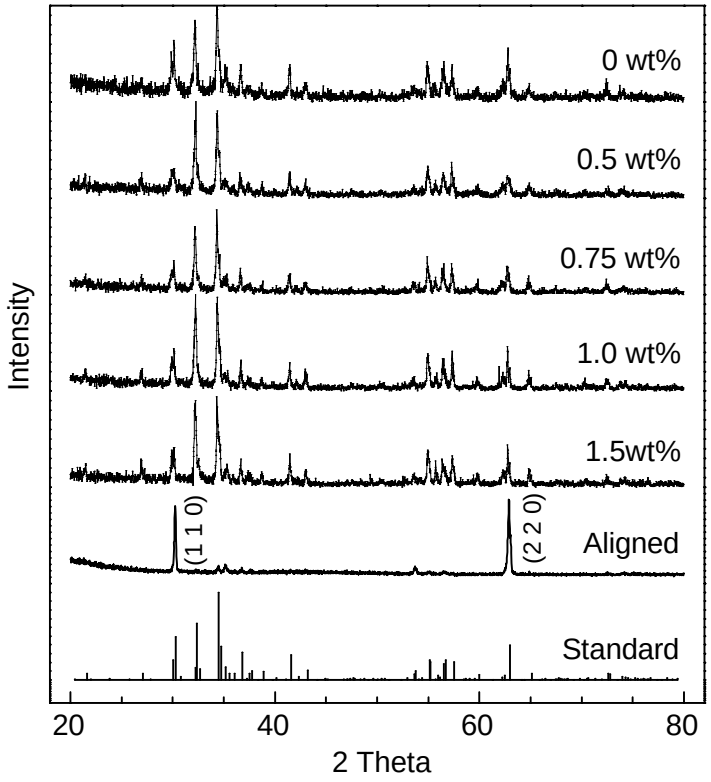

Fig. 6-1. XRD patterns for $BaCoZnFe_{16}O_{27}$ doped with various amounts of V_2O_5.

Using the *d*-spacing values for the crystal planes with strong diffraction, lattice parameters *a* and *c* are calculated by the least squares method. The values of lattice parameters *a* and *c*, cell volume *V* and parameter *c/a* are listed in Table 6-1. The parameters are almost constant, *a*=0.5925 (3) nm, *c*=3.304 (5) nm and *V*=1.004 (2)

nm^3 for the samples doped with different amounts of V_2O_5. Dependence on the doping amount of V_2O_5 is not obviously observed within experimental error for all parameters. Therefore, a small amount of V_2O_5 addition has no significant effect on the crystal structure.

In addition, Table 6-1 also lists the bulk density for all samples. ρ_A and ρ_m are the results measured by Archimedean and mass-volume method, respectively. For the undoped sample, the values of ρ_A and ρ_m are 4.98 g/cm^3 and 4.88 g/cm^3, respectively. With the increase in V_2O_5 addition, ρ_A keeps almost constant and is about 5.0 g/cm^3, while ρ_m greatly decreases, from 4.88 g/cm^3 for undoped sample to 3.05 g/cm^3 for the sample doped with 1.5 wt% of V_2O_5. This behavior has its origin in the high porosity in the V_2O_5 doped samples, which will be verified by SEM images. The density measured by the Archimedean method is for the particles and is not related to the porosity in the sintered samples.

Table 6-1. Lattice parameters and density for $BaCoZnFe_{16}O_{27}$ doped with various amounts of V_2O_5. ρ_A and ρ_m represent the results measured by Archimedean and mass-volume method, respectively.

V_2O_5 (wt%)	*a* (nm)	*c* (nm)	*V* (nm^3)	*c*/*a*	ρ_A (g/cm^3)	ρ_m (g/cm^3)
0	0.5922 (2)	3.304 (3)	1.003 (2)	5.579 (3)	4.98	4.88
0.5	0.5927 (4)	3.305 (5)	1.005 (3)	5.576 (5)	4.96	4.46
0.75	0.5928 (2)	3.309 (2)	1.007 (1)	5.582 (1)	5.02	3.79
1.0	0.5924 (2)	3.299 (2)	1.003 (1)	5.569 (1)	5.02	3.51
1.5	0.5923 (4)	3.304 (4)	1.004 (3)	5.578 (3)	4.97	3.05

6.1.2 SEM morphology

Figure 6-2 shows SEM images of the bulk material for the undoped and doped samples. It is found that the morphology for the samples doped with small amounts of V_2O_5 is completely different from the undoped case. For the undoped sample, the grains are cuboidlike in shape. The width and length of the grains are about 3 and 10 μm, respectively. They stack compactly and just a few intergranular pores can be observed.

However, for the samples doped with small amounts of V_2O_5, the particles are of hexagonal-plate shape and are well separated from each other. Grain boundaries are evident. The thickness of the grains is about 2 μm and average diameter is about 11 μm. It appears that the ratio of the thickness to diameter of the grains is slightly decreased with the increase in V_2O_5 doping amount. Large intergranular pores are clearly present. The porosity increases with the increase in V_2O_5 concentration, which leads to the decrease of density ρ_m.

These obvious changes originate from the liquid phase sintering. It appears that, during sintering, V_2O_5 with low melting point (690 ºC) exists around the ferrite grain surface as a wetting agent, effectively lowering the surface tension. This assists in the formation of the almost perfect hexagonal plate-like grains. The high intergranular porosity is due to the irregular alignment of hexagonal plates. Similar results have also been observed by Zhang *et al.*[101] and Hsiang *et al.*[102] in the case of Bi_2O_3 and glass additives, respectively.

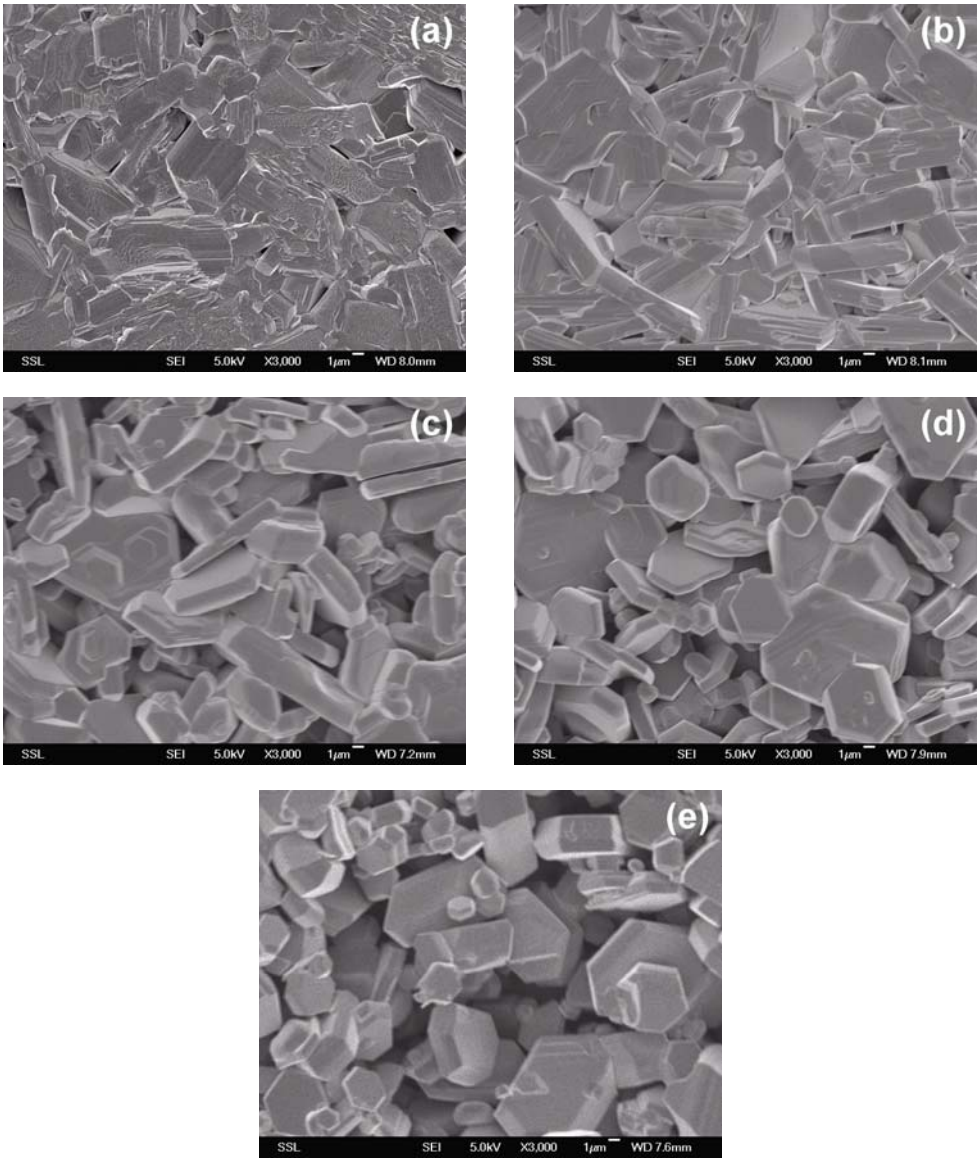

Fig. 6-2. SEM images for sintered samples of $BaCoZnFe_{16}O_{27}$ doped with various amounts of V_2O_5, (a) without doping, (b) 0.5 wt%, (c) 0.75 wt%, (d) 1.0 wt% and (e) 1.5 wt%.

Also, typical SEM images of the crushed powders are shown in Fig. 6-3. For the doped samples, the particles possess a fine-grained morphology. It means that intercrystalline fracture is predominant in the crush procedure. However, for the undoped sample, the particles do not have a definite shape, as transcrystalline fracture has lower energy than other fracture modes. It appears that, during sintering, the

liquid phase around the particles effectively decreases the strength of the intergranular cohesion. Therefore, the fracture mode is changed from transcrystalline to intercrystalline fracture due to the addition of V_2O_5.

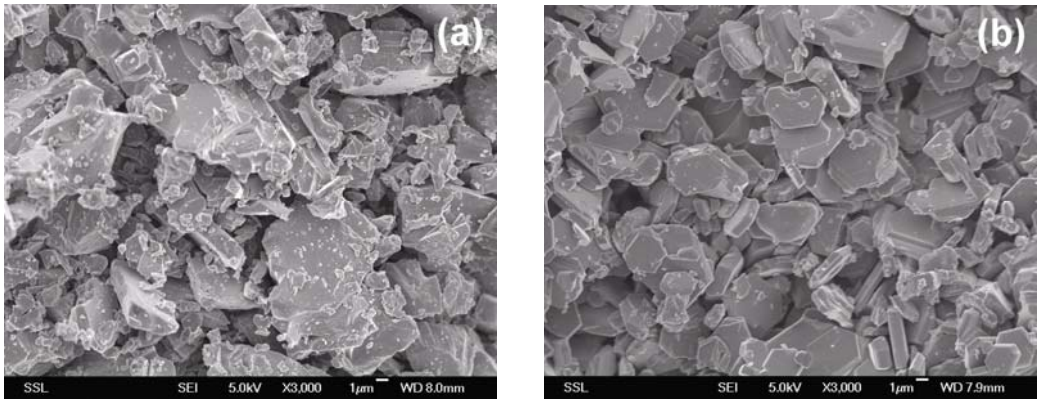

Fig. 6-3. Typical SEM images for powders of $BaCoZnFe_{16}O_{27}$ without and with V_2O_5 doping, (a) without doping, (b) doped with 1.0 wt%.

6.1.3 Static magnetic property

The magnetization curves and *M-H* loops were measured with applied fields of 0-14 kOe and between -14 and +14 kOe, respectively. The values of saturation magnetization M_s and coercivity H_c for all samples are plotted as function of the V_2O_5 doping amount in Fig. 6-4. In the given amounts of V_2O_5 addition, the saturation magnetization M_s remains almost constant, until the doping concentration is raised to 1.0 wt%, and then rapidly decreases at higher additive. The coercivity H_c decreases gradually from 29.2 to 18.2 Oe as doping of V_2O_5 varies from 0 to 1.5 wt%.

It is well known that, for soft magnetic material with multi-domain structure, the coercive H_c is mainly controlled by the movement of domain wall. The decrease of coercivity implies that domain wall moves easily. The mobilization of domain wall seems to be related to the liquid phase sintering of V_2O_5. Goldman[103] pointed out that

the intragranular pores, impurity distribution and other imperfections act as a dominant hindrance to the movement of the domain walls in ferrites. During sintering, V_2O_5 existed around particles in liquid phase, which may effectively clean grain boundaries, reduce inner stresses and decrease impurity distribution. Therefore, the domain wall moves easily, leading to a significant decrease in coercivity H_c.

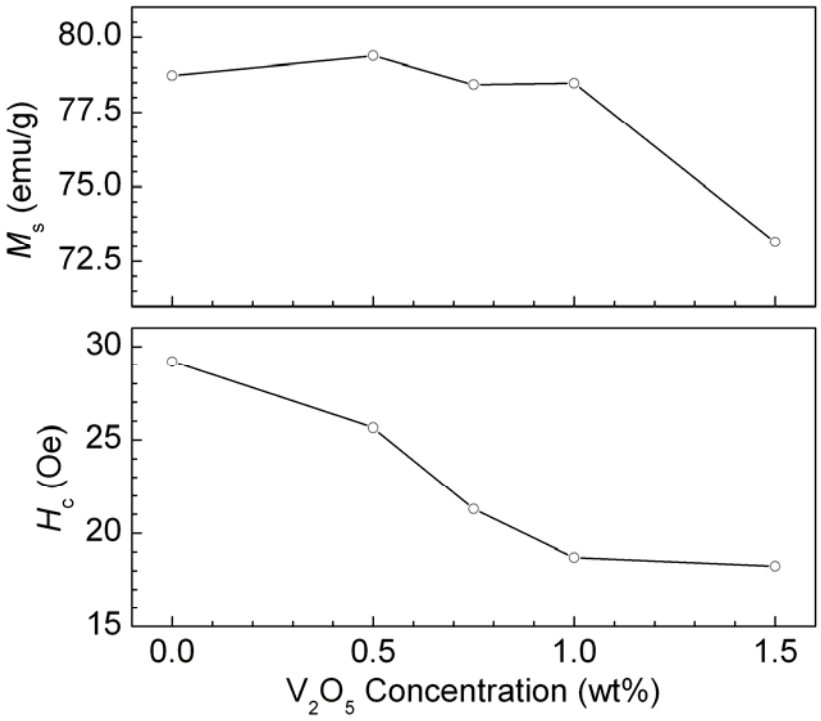

Fig. 6-4. The variation of M_s and H_c with the doping of various V_2O_5 for ferrites of $BaCoZnFe_{16}O_{27}$.

In addition, the anisotropy field H_θ was also estimated by the initial magnetization curves for aligned samples. The easy and hard magnetization curves, which are parallel and perpendicular to the alignment direction, respectively, were measured at room temperature. All samples were demagnetized before measurement. The maximum applied magnetic field is 14 kOe. The values of anisotropy field H_θ were estimated at 8.6, 8.2, 7.5, 9.0 and 8.0 kOe for the samples doped with 0, 0.5, 0.75, 1.0

and 1.5 wt% of V_2O_5. Therefore, doping of V_2O_5 does not have a noticeable effect on the anisotropy field H_θ. Fig. 6-5 shows the magnetization curves along two directions for the undoped and 1.0 wt% V_2O_5 doped samples for illustration.

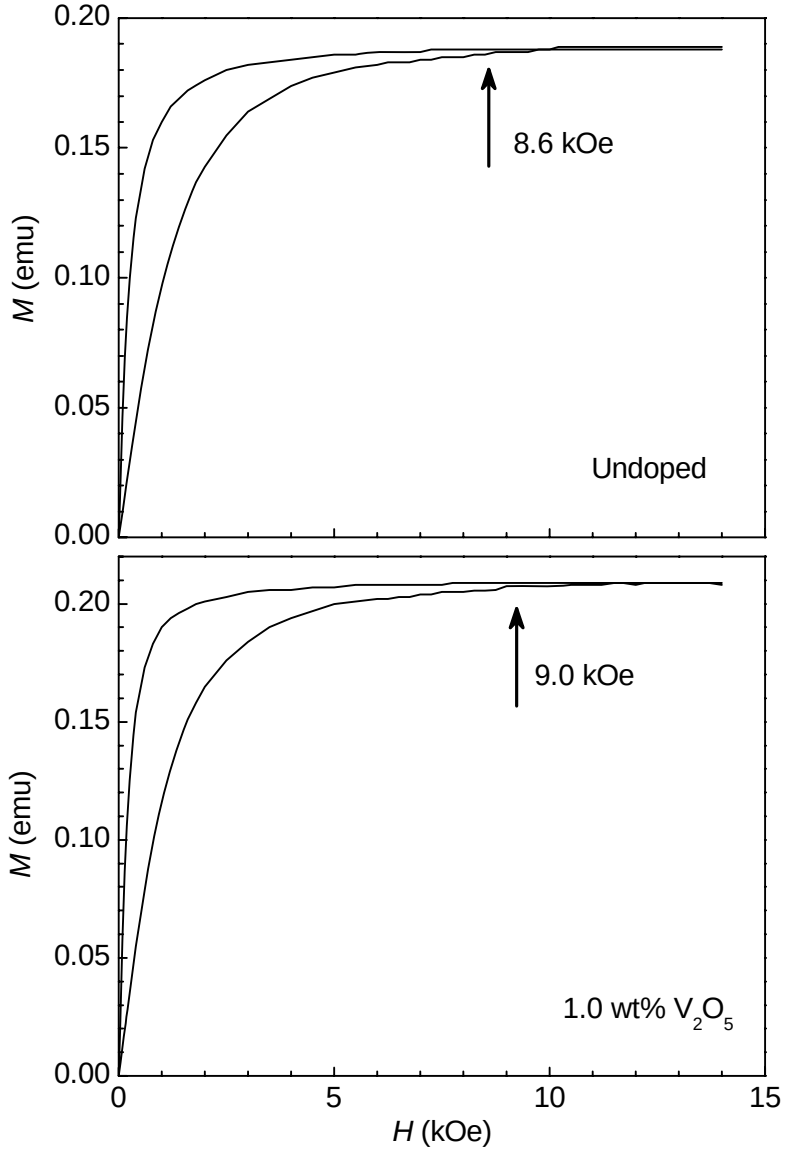

Fig. 6-5. The magnetization curves parallel and perpendicular to the alignment direction for the undoped and 1.0 wt% V_2O_5 doped aligned samples.

6.1.4 Dynamic magnetic property

The composites for all samples were fabricated by filling with 50 % (by volume) ferrite powders. The complex permittivity ε and permeability μ for all composites were measured from 0.5 to 16.5 GHz and from 0.1 to 16.5 GHz, respectively. The values of dielectric constant do not show observable dependence on the doping of V_2O_5. For all composites, the real part ε' and imaginary part ε'' remain almost constant over the investigated frequency range. ε' varies slightly from 7.4 at 0.5 GHz to 7.0 at 16.5 GHz, while ε'' is about 0.3 over the whole frequency range.

The spectra of complex permeability are shown in Fig. 6-6 for all composites. Some important dynamic parameters of the two resonances, namely domain wall and natural resonance, are also listed in Table 6-2. In the table, $\mu_0^{'}$ is the static permeability, $\mu_{\max,N(W)}^{''}$ and $f_{r,N(W)}$ are the maximum imaginary permeability and the resonance frequency of natural (domain wall) resonance, respectively. As compared with the undoped sample, three important characteristics of the permeability spectra are observed for the doped samples.

Firstly, the static permeability, $\mu_0^{'}$, significantly increases from 3.1 to 4.4, as the doping amount δ varies from 0 to 1.0 wt%, then slightly decreases to 4.2 for δ=1.5 wt%. The increase in $\mu_0^{'}$ may be attributed to the decrease in H_c.

Secondly, both the domain wall resonance and natural resonance are significantly enhanced with the increase in the doping amount of V_2O_5. For domain wall resonance, the maximum imaginary permeability $\mu_{\max,W}^{''}$ is about 0.6 at δ=0, and increases significantly to 1.3 at δ=1.0 wt%. For natural resonance, the maximum imaginary

permeability $\mu''_{max,N}$ also increases from 1.2 at δ=0 to 1.8 at δ=1.0 wt%.

Finally, the resonance frequency is about 0.6-0.7 GHz for the domain wall resonance. The natural resonance occurs at 6.0, 5.7, 4.7, 4.0 and 3.4 GHz for samples with δ=0, 0.5, 0.75, 1.0 and 1.5 wt%, respectively, shifting to lower frequency with the increase in the amount of V_2O_5 doping. This behavior will be explained in detail in Section 6.3.2, based on the demagnetizing effect.

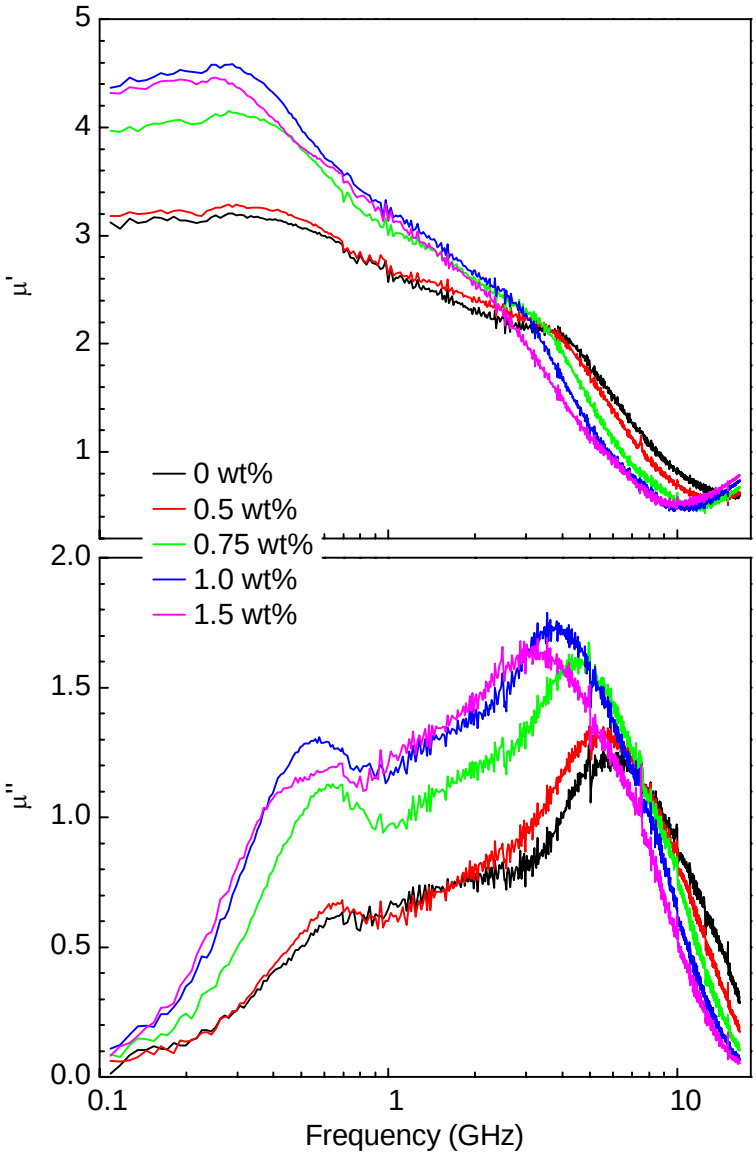

Fig. 6-6. Complex permeability μ' and μ'' from 0.1 to 16.5 GHz for composites of $BaCoZnFe_{16}O_{27}$ doped with various amounts of V_2O_5.

Table 6-2. Parameters of dynamic magnetic properties for $BaCoZnFe_{16}O_{27}$ doped with various amounts of V_2O_5.

V_2O_5 (wt%)	$\mu_0^{'}$	$\mu_{\max.W}^{''}$	$\mu_{\max.N}^{''}$	$f_{r.W}$ (GHz)	$f_{r.N}$ (GHz)
0	3.1	0.6	1.2	0.69	6.0
0.5	3.2	0.7	1.3	0.67	5.7
0.75	4.0	1.1	1.6	0.65	4.7
1.0	4.4	1.3	1.8	0.55	4.0
1.5	4.2	1.2	1.7	0.65	3.1

6.1.5 Microwave absorbing property

The reflection loss (*RL*) with various thickness *t* over 0.5-16.5 GHz was calculated using the data of ε and μ for the samples of $BaCoZnFe_{16}O_{27}$ doped with various amount of V_2O_5. Based on the calculated results, the upper- and lower-frequency limits, f_{up} and f_{low}, and the relative bandwidth $W = f_{up} / f_{low}$ are determined for each thickness.

The dependence of f_{up} and f_{low} on thickness *t* for each composite is shown in Fig. 6-7. The maximum relative bandwidth W_{max} is indicated by the arrow in the figure. The thickness corresponding to W_{max} is defined as the optimum thickness t_o. The dependence of *RL* on frequency at the optimum thickness t_o is shown in Fig. 6-8.

Based on Fig. 6-7, as the doping amount δ increases, the frequency band for $RL \le -10$ dB is shifted to lower frequency. f_{low} and f_{up} decrease from 5.5 to 3.5 GHz and 16.5 to 12.7 GHz, respectively, with the increase in δ from 0 to 1.5 wt%. On the other hand, the optimum thickness t_o increases from 2.4 to 3.2 mm, as the doping of V_2O_5 varies from 0 to 1.5 wt%. These two characteristics may be attributed to the

decrease in the natural resonance frequency with the doping of V_2O_5. To obtain broadband performance, $ft\sqrt{\mu\varepsilon}$ should remain constant. Therefore, as the resonance frequency decreases due to the doping of V_2O_5, the corresponding thickness of the composites will be increased.

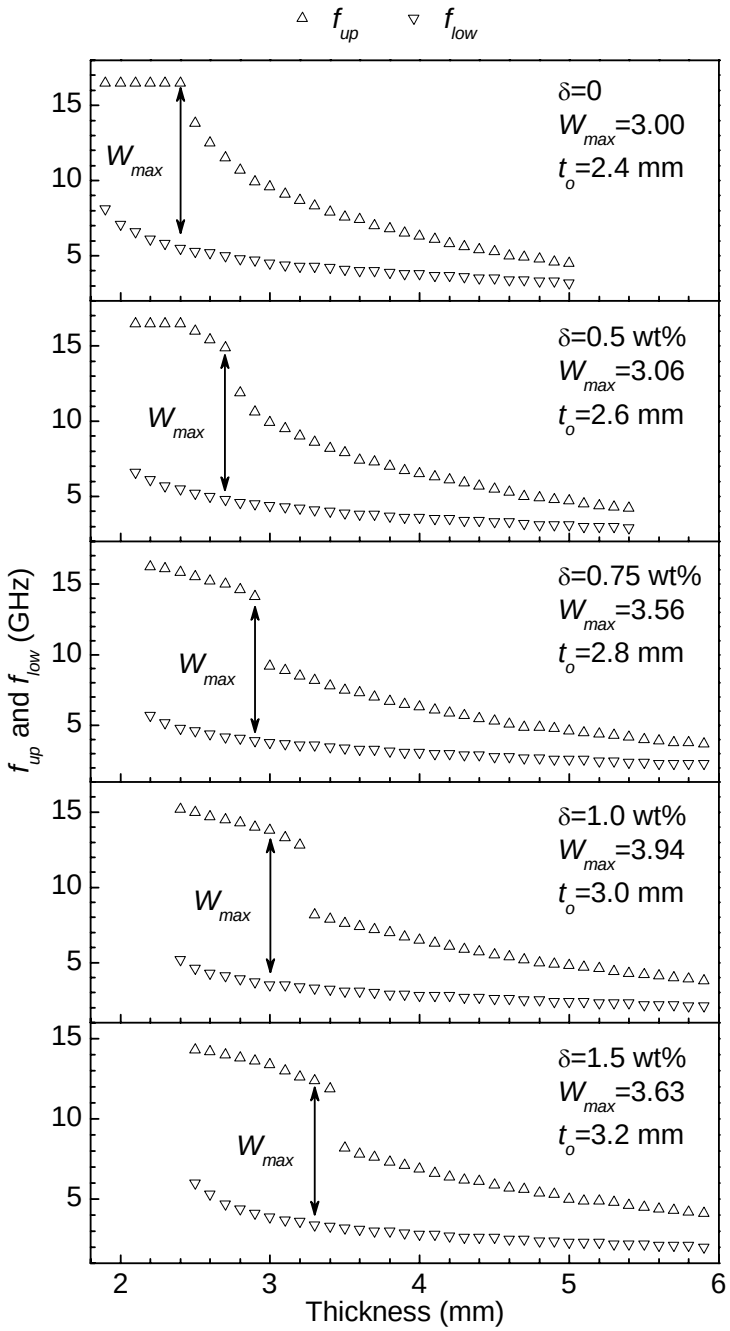

Fig. 6-7. The dependence of f_{up}, f_{low} and W for absorption of more than 10 dB on the thickness of $BaCoZnFe_{16}O_{27}$ composites doped with various amounts of V_2O_5.

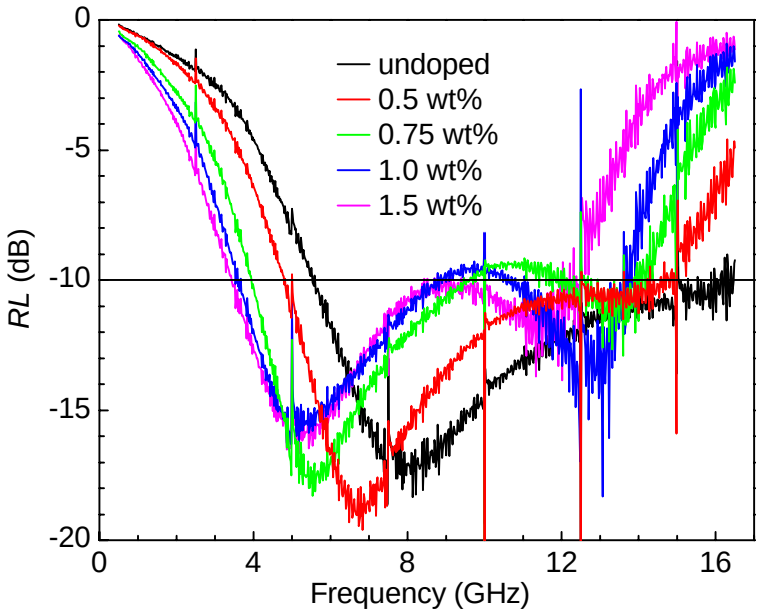

Fig. 6-8. Absorbing characteristics for composites of $BaCoZnFe_{16}O_{27}$ doped with various amounts of V_2O_5 at the optimum thickness t_o.

The maximum relative bandwidth W_{max} increases considerably from 3.0 to 3.9, as the doping amount δ varies from 0 to 1.0 wt%. The improvement mostly has its origin in the greatly enhancement in $\mu_0^{'}$ and $\mu_{\max}^{''}$ due to the V_2O_5 doping. However, for δ=1.5 wt%, the decreased $\mu_0^{'}$ and $\mu_{\max}^{''}$ lead to a relatively narrow bandwidth of W_{max}=3.6.

In addition, from Fig. 6-8, two dips in *RL-f* curves are observed for all composites. As discussed in Chapter 5, the dip at lower frequency is attributed to the magnetic loss and the other results from the quarter wavelength effect (thickness loss).

In summary, the composite doped with 1.0 wt% of V_2O_5 has very excellent absorbing property for use as EM materials with low reflectively and broadband at microwave frequency; the frequency band for $RL \le -10$ dB is from 3.5 to 13.8 GHz, covering C- and X-bands. The relative bandwidth reaches 3.9 with a thickness of 3.0 mm.

6.2 1.0 wt% of V_2O_5 doping in $BaCo_xZn_{2-x}Fe_{16}O_{27}$

6.2.1 Crystal structure and static magnetic property

In the above section, the studies on the composites of $BaCoZnFe_{16}O_{27}$ doped with 0-1.5 wt% of V_2O_5 have been introduced. It was found that the composite doped with 1.0 wt% of V_2O_5 has very excellent absorbing property. In this section, the work on 1.0 wt% of V_2O_5 doping in $BaCo_xZn_{2-}xFe_{16}O_{27}$ with x=1.3 and 1.5 will be reported. The work aims to seek the ideal EM absorbing materials suitable for different frequency bands. For simplicity, in following discussions, Co13W (Co13WV) and Co15W (Co15WV) will be used as the abbreviations of the undoped (doped) samples of $BaCo_xZn_{2-x}Fe_{16}O_{27}$ with 1.3 and 1.5, respectively.

The microstructure and static magnetic properties have been studied for all samples. The detailed analyses are similar as those of $BaCoZnFe_{16}O_{27}$. The pure phase with BaW hexagonal structure was confirmed by XRD for all samples. The lattice parameters (*a*, *c* and *V*), densities (ρ_A and ρ_m) and static magnetic parameters (M_s and H_c) are listed in Table 6-3.

Table 6-3. Lattice parameters, density and static magnetic parameters for BaW doped with 1.0 wt% of V_2O_5. ρ_A and ρ_m represent the results measured by Archimedean and mass-volume method, respectively.

	Lattice parameters			Density (g/cm^3)		Magnetic parameters	
	a (nm)	*c* (nm)	*V* (nm^3)	ρ_A	ρ_m	M_s (emu/g)	H_c (Oe)
Co13W	0.5921 (1)	3.305 (1)	3.010 (2)	4.97	4.77	70.7	35.3
Co13WV	0.5935 (3)	3.309 (4)	3.028 (6)	5.03	3.40	72.4	25.3
Co15W	0.5909 (1)	3.297 (2)	2.991 (2)	4.97	4.74	69.1	44.1
Co15WV	0.5923 (1)	3.310 (3)	3.017 (4)	4.98	3.37	71.2	33.0

6.2.2 Dynamic magnetic property

The electromagnetic properties of the composites filled with 50 % (by volume) ferrite powders are characterized from 0.5 to 16.5 GHz. There is no noticeable difference in dielectric properties, as compared with the composites investigated in the previous section. The real permittivity ε' is about 7.0-7.4, while the imaginary part ε'' is about 0.3 over the whole frequency range.

The spectra of complex permeability are shown in Fig. 6-9 for all composites. Some important high-frequency parameters are listed in Table 6-4. $\mu'_{0.5}$ is defined as the value of real permeability at the frequency of 0.5 GHz. Due to the weakness of domain wall resonance, it is difficult to determine the wall resonance frequency $f_{r,W}$ accurately, especially for the undoped samples. For Co13WV and Co15WV, $f_{r,W}$ is estimated at about 2.2 and 2.6 GHz, respectively, as indicated by the arrows in Fig. 6-9.

The natural resonance frequency $f_{r,N}$ is 9.1 and 12.5 GHz for composites of Co13W and Co15W, respectively. With the doping of V_2O_5, $f_{r,N}$ is shifted to lower frequency, which is 6.1 and 7.3 GHz for Co13WV and Co15WV, respectively. The decrease in $f_{r,N}$ is attributed to the change in the shape of the particles, from cuboid-like to hexagonal plate-like particles. The detailed discussion will be given in Section 6.3.2.

However, for the samples with V_2O_5 doping, the domain wall resonance is clearly observed and locates at about 2.0 GHz. Let's consider the imaginary permeability μ'' at 2.0 GHz as the contribution of domain wall resonance. The values of imaginary

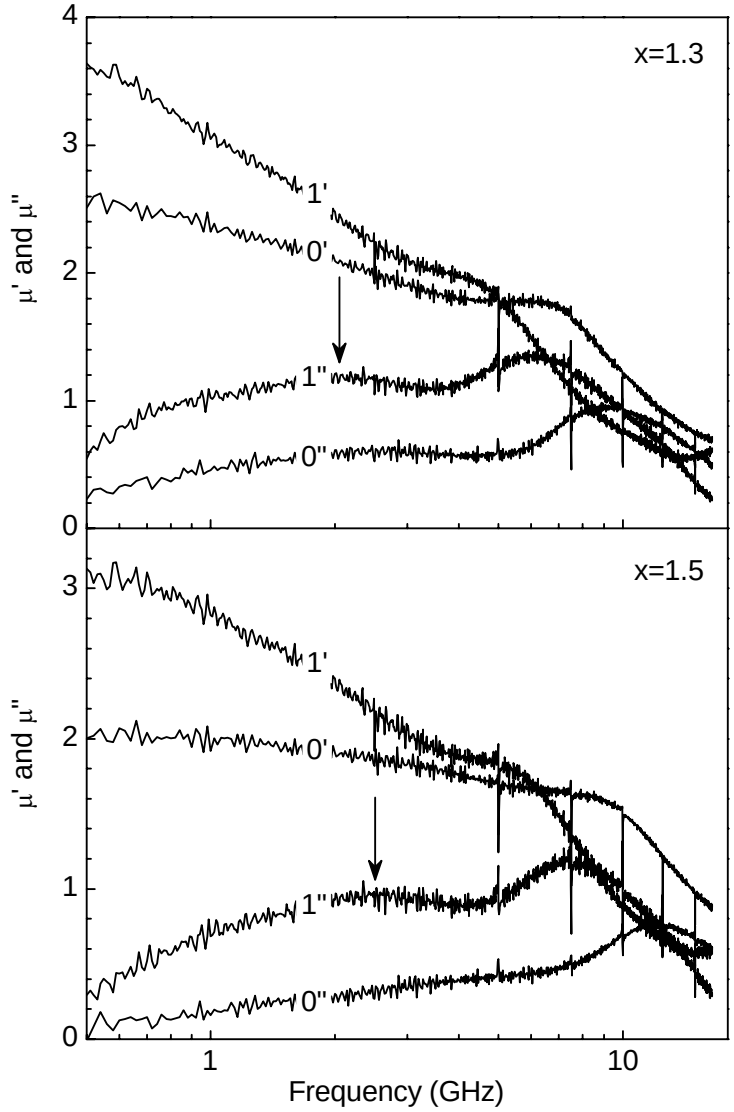

Fig. 6-9. The complex permeability spectra for undoped (indicated as 0' and 0") and doped (indicated as 1' and 1") samples of $BaCo_xZn_{2-x}Fe_{16}O_{27}$ with x=1.3 and 1.5.

Table 6-4. Dynamic magnetic properties for BaW with and without V_2O_5 doping. $\mu'_{0.5}$ and $\mu''_{0.5}$ are the real and imaginary permeability at 0.5 GHz, respectively. $f_{r,N}$ and $f_{r,W}$ are the resonance frequency for natural and domain wall resonances, respectively.

	$\mu'_{0.5}$	$\mu''_{0.5}$	μ''_{max}	$f_{r,N}$ (GHz)	$f_{r,W}$ (GHz)
Co13W Co13WV	2.5 3.6	0.2 0.6	0.9 1.4	9.1 6.1	- 2.2
Co15W Co15WV	2.0 3.1	0 0.4	0.8 1.2	12.5 7.3	- 2.6

permeability are significantly larger for the composites doped with V_2O_5 than the undoped ones. The difference of imaginary permeability between the doped and undoped samples is 0.9 and 0.5 for x=1.3 and 1.5, respectively. On the other hand, the natural resonance is also strengthened. With 1.0 wt% of V_2O_5 doping, the maximum imaginary permeabilities $\mu''_{\max}$ increase from 0.9 to 1.4 for x=1.3 and from 0.8 to 1.2 for x=1.5, increasing by about 40 %.

In addition, the real permeability at 0.5 GHz $\mu'_{0.5}$ greatly increases for composites doped with 1.0 wt% of V_2O_5. As compared with the undoped samples, $\mu'_{0.5}$ increases by about 50 %.

6.2.3 Microwave absorbing property

Figure 6-10 shows the frequency dependence of the reflection loss at optimum thickness t_o for each sample. The values of f_{up}, f_{low}, t_o and the corresponding $W_{\max}$ are listed in Table 6-5. In addition, the results of $BaCoZnFe_{16}O_{27}$ composites without and with doping of 1.0 wt% V_2O_5 are also shown in this segment for comparison. Similarly, Co10W and Co10WV will be used as the abbreviations of the undoped and doped samples of $BaCoZnFe_{16}O_{27}$, respectively.

The maximum relative bandwidth $W_{\max}$ of composites doped with V_2O_5 increases considerably, as compared with the corresponding composites without the doping. As shown in Table 6-5, for the composite of Co15W, the lower and upper bands, f_{low} and f_{up}, are 9.4 and 16.1 GHz, respectively, and $W_{\max}$ is 16.1/9.4=1.7. For the corresponding composite doped with V_2O_5, f_{low} and f_{up} are 6.3 and >16.5 GHz,

respectively, and W_{max} is larger than 2.6. Due to the doping, the maximum relative band width W_{max} is increased by more than 53 %. This reveals a good EM material with low reflectivity and broad bandwidth at X- and Ku-bands. Similar enhancement is also observed in the samples of x=1.0 and 1.3 as well. For the composite of Co13WV, f_{low} and f_{up} are 5.0 and 15.7 GHz, respectively, and W_{max} is 3.1. For the composite of Co10WV, f_{low} and f_{up} are 3.5 and 13.8, respectively, and W_{max} is 3.9. As compared with Co13W and Co10W, W_{max} is increased by about 50 % and 30 %, respectively.

It has been introduced that large complex permeability is necessary for magnetic materials with excellent absorbing ability. Due to the doping of V_2O_5, $\mu_0^{'}$ (or $\mu_{0.5}^{'}$) and $\mu_{max}^{''}$ are significantly enhanced, leading to a large magnetic resonance loss. On the other hand, for doped samples, two minima in the reflection loss, $RL_{min,1}$ at lower frequency and $RL_{min,2}$ at high frequency, are observed. The minimum at low frequency is associated with the magnetic resonance loss and the other is related to the thickness of the composites. In this case, the total reflection loss can be considered as an overlap of two components, the magnetic resonance loss and the quarter wavelength effect. However, for the undoped samples, especially for Co13W and Co15W, there is only one minimum $RL_{min,1}$ in *RL-f* curves in the frequency range of 0.5-16.5 GHz. The dip is related to the magnetic resonance loss. Therefore, besides the magnetic resonance loss, the thickness of composites makes an extra contribution on the reflection loss. The overlap of the contributions leads to a considerably increased bandwidth W_{max}.

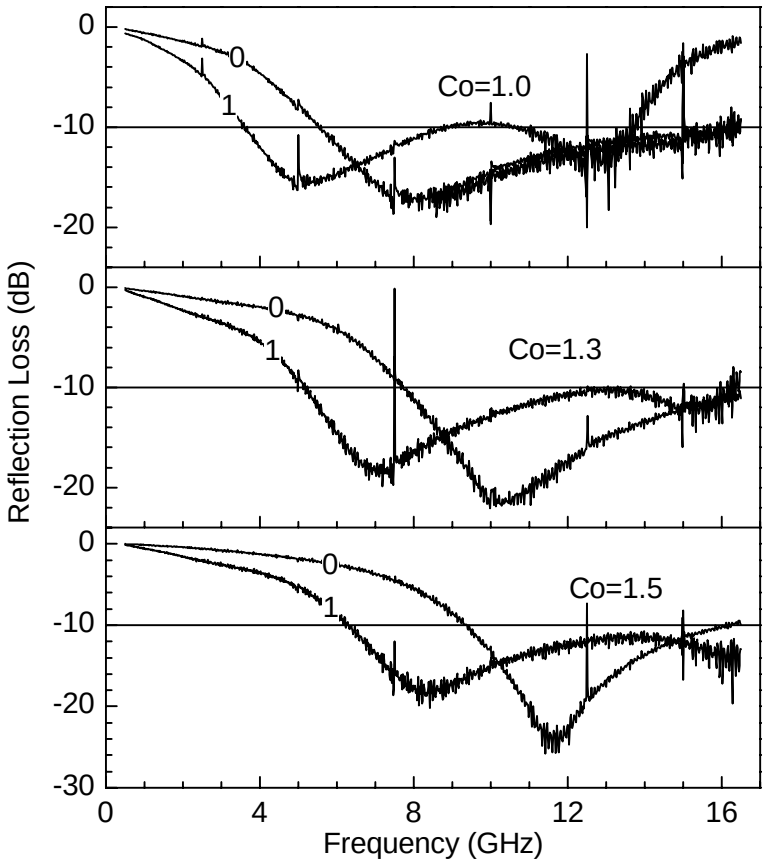

Fig. 6-10. Absorbing characteristics for undoped (marked by 0) and doped (marked by 1) $BaCo_xZn_{2-x}Fe_{16}O_{27}$ composites with x=1.0, 1.3 and 1.5 at the optimum thickness.

Table 6-5. The optimum thickness t_o, the upper- and lower-limits of frequency, f_{up} and f_{low}, of bandwidth for absorption of more than 10 dB, and the relative bandwidth of $W = f_{up} / f_{low}$ for undoped and doped $BaCo_xZn_{2-x}Fe_{16}O_{27}$ composites with x=1.0, 1.3 and 1.5.

	f_{low} (GHz)	f_{up} (GHz)	$W_{\max}$	t_o (mm)
Co10W Co10WV	5.5 3.5	16.5 13.8	3.0 3.9	2.4 3.0
Co13W Co13WV	7.7 5.0	16.5 15.7	2.1 3.1	2.0 2.6
Co15W Co15WV	9.4 6.3	16.1 ≥16.5	1.7 ≥2.6	1.9 2.2

6.3 Discussion

6.3.1 Static permeability

It has been shown that the static permeability $\mu_0^{'}$ greatly increases with a small amount of V_2O_5 doping. The increase in $\mu_0^{'}$ possibly has an origin in the decrease in H_c.

In the rotation model for magnetic moment, the permeability is related to the in-plane anisotropy field H_ϕ, i.e. $\mu \propto M_s / H_\phi$,[97] for particles with *c*-plane anisotropy. The values of H_ϕ has been estimated at about 600 Oe for $BaCoZnFe_{16}O_{27}$. However, when the domain wall is present, an enhanced permeability from reversible wall movement is obtained from a small value of coercivity H_c (less than 30 Oe) by $\mu \propto M_s / H_c$.[88] The dependence of $\mu_0^{'}$ on the ratio of saturation magnetization to coercivity, M_s / H_c, is indeed observed, as shown in Fig. 6-11. As the doping of V_2O_5 varies from 0 to 1.0 wt%, M_s is almost constant, while coercivity H_c decreases by about 36 %, from 29.2 Oe at δ=0 to 18.7 Oe at δ=1.0 wt%. Therefore, the doping of V_2O_5 leads to a significant decrease in coercivity, thus increasing the static permeability $\mu_0^{'}$.

Corresponding to the natural and domain wall resonances, the static permeability $\mu_0^{'}$ consists of two components, gyromagnetic permeability and wall displacement permeability. The increase in $\mu_0^{'}$ is mostly contributed by the enhancement of wall permeability.

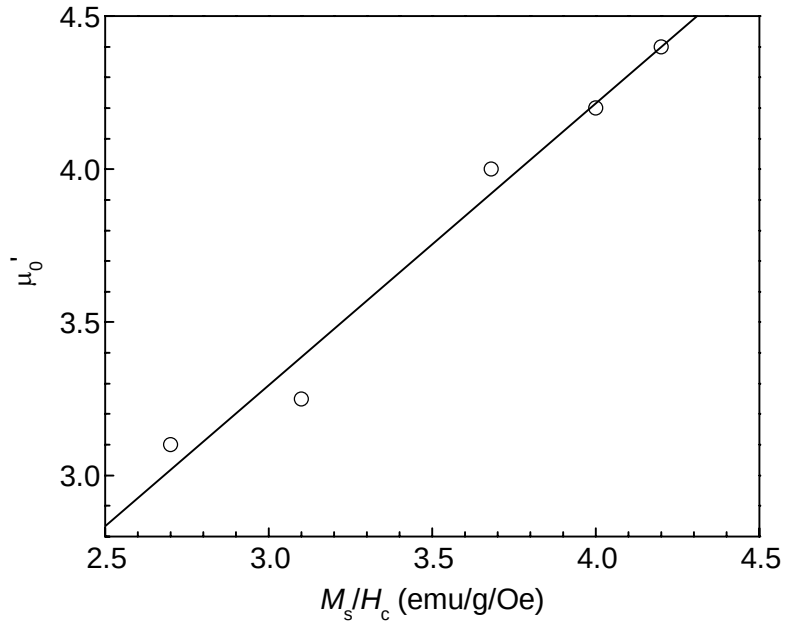

Fig. 6-11. The relationship between M_s/H_c and $\mu_0^{'}$ for $BaCoZnFe_{16}O_{27}$ doped with various amounts of V_2O_5.

Based on Figs. 6-6 and 6-9, at the frequency of natural resonance, the value of the real permeability for V_2O_5 doped samples is almost same as the corresponding undoped samples. However, at low frequency, such as 0.5 GHz, the real permeability $\mu_{0.5}^{'}$ of doped composites is significantly larger than those without doping. For example, $\mu_{0.5}^{'}$ is about 4.2 for the sample of Co10WV, while only 3.0 for Co10W. On the other hand, the real permeability can be approximately considered as linear relation with frequency in the range of 0.5-3.0 GHz for all samples. The slope is much larger for the doped composites than those without doping. Let's take the samples of x=1.5 as an example. The slope is about 0.4 for the 1.0 wt% of V_2O_5 doped sample, while it is close to zero for the corresponding undoped sample. All of these characteristics show that the increase of static permeability $\mu_0^{'}$ mainly results from the enhancement of wall displacement.

6.3.2 Natural resonance frequency

It has been observed that the natural resonance is shifted to lower frequency due to the doping of small amount of V_2O_5. In general, the natural resonance frequency is related to the anisotropy field and demagnetizing field. In Section 6.1.3, it has been confirmed that doping of V_2O_5 does not have a noticeable effect on the anisotropy field. Therefore, it seems that the decrease of natural resonance frequency is not induced by the anisotropy field. Now, let's consider the demagnetizing effect or shape of particles effect on resonance frequency.

The universal resonance frequency f_r is given by[104]

$$f_r = \frac{\gamma}{2\pi M_s \sin\theta}\left[\left(\frac{\partial^2 F}{\partial\theta^2}\right)\left(\frac{\partial^2 F}{\partial\phi^2}\right)-\left(\frac{\partial^2 F}{\partial\theta\partial\phi}\right)^2\right]^{1/2} \qquad 6\text{-}1$$

for the precession of the magnetization vector around a stable direction, i.e. the direction of $\partial F/\partial\theta = 0$ and $\partial F/\partial\phi = 0$. In Eq. 6-1, θ and ϕ are the polar and azimuth angles associated with the direction of magnetization vector M, respectively, and F is the free energy.

In the rotation model, the free energy F includes two parts, demagnetizing energy E_d and magnetocrystalline anisotropy energy E_a, and is given by

$$F = E_d + E_a = \frac{1}{2}M_s^2\left(N_x \sin^2\theta\cos^2\phi + N_y \sin^2\theta\sin^2\phi + N_z\cos^2\theta\right)$$
$$+\left(K_1\sin^2\theta + K_2\sin^4\theta + K_3\sin^6\theta\cos 6\phi\right), \qquad 6\text{-}2$$

where N_x, N_y and N_z are the demagnetizing factors along the x, y and z-axis, respectively, and K_1, K_2 and K_3 are the first, second and third order magnetocrystalline

anisotropy constants, respectively.

In the expression of the anisotropy energy E_a, the first two terms are related to the out-of-plane anisotropy field H_θ, and the third term is the six-fold energy term associated with the in-plane anisotropy field H_ϕ. H_θ and H_ϕ are given by

$$H_\theta = \frac{2(K_1 + 2K_2)}{M_s} \text{ and}$$

$$H_\phi = \frac{36K_3}{M_s},$$

respectively. Substituting Eq. 6-2 into Eq. 6-1, the resonance frequency can be expressed as[105]

$$f_r = \frac{\gamma}{2\pi}\left[H_\theta + (N_x - N_z)M_s\right]^{1/2}\left[H_\phi + (N_x - N_y)M_s\right]^{1/2} \quad 6\text{-}3$$

for *c*-plane anisotropy.

For spherical particles, due to the demagnetizing factors of $N_x = N_y = N_z = 1/3$, the resonance frequency f_r is given by

$$f_r = \frac{\gamma}{2\pi}\left(H_\theta H_\phi\right)^{1/2}. \quad 6\text{-}4$$

For particles with disk shape, the demagnetizing factors are approximately $N_x = N_y = 0$ and $N_z = 1$, assuming the disk is perpendicular with the *z*-axis. Therefore, the resonance frequency f_r is given by

$$f_r = \frac{\gamma}{2\pi}\left[(H_\theta - M)H_\phi\right]^{1/2}. \quad 6\text{-}5$$

It has been previously confirmed that the magnetocrystalline anisotropy field H_θ is not

modified with the doping of V_2O_5. In Chapter 4, it has been reported that, for BaW ferrite of $BaCoZnFe_{16}O_{27}$, the out-of-plane anisotropy field H_θ is about 8.5 kOe and the in-plane anisotropy field H_ϕ is about 0.65 kOe. For the undoped sample, as shown in the SEM images for the crushed powders, the particles in composites have no definite shape. As it is difficult to accurately estimate the demagnetizing factors, for simplicity, spherical particles are assumed. Based on Eq. 6-4, the natural resonance frequency is estimated at $f_r = 2.8\sqrt{8.5 \times 0.65} = 6.6$ GHz, which is consistent with the experimental result of 6.0 GHz for undoped composites.

For the sample doped with 1.0 wt% V_2O_5, the particles in composites possess the morphology of perfect hexagonal-plate grains, thus f_r can be roughly calculated by Eq. 6-5. Refer to the results of VSM, the saturation magnetization M_s is 78.5 emu/g. The density measured by Archimedean method ρ_A is 5.02 g/cm^3. Base on the conversion magnetic unit, $M_s = 78.5 \times 5.02$ emu/cm^3 $= 78.5 \times 5.02 \times 4\pi$ Oe = 5.0 kOe. Hence, the natural resonance frequency is given by $f_r = 2.8\sqrt{(8.5 - 5.0) \times 0.65} = 4.2$ GHz, which also agrees well with the experimental result of 4.0 GHz.

In addition, from the SEM images, it appears that the ratio of the thickness to diameter of the grains is decreased by doping with V_2O_5. This implies the increase in the demagnetizing factor N_z and decrease in the demagnetizing factors N_x and N_y for hexagonal-plate particles. Consequently, the resonance frequency f_r decreases with the doping of V_2O_5.

6.4 Conclusions

Two series of composites, $BaCoZnFe_{16}O_{27}$ doped with various amounts of V_2O_5 (δ

varying from 0 to 1.5 wt%) and $BaCo_xZn_{2-x}Fe_{16}O_{27}$ (x=1.3 and 1.5) doped with 1.0 wt% of V_2O_5 have been investigated. The main conclusions are listed as follows:

(1). According to the investigation on $BaCoZnFe_{16}O_{27}$ doped with various amounts of V_2O_5, it is found that the composite with 1.0 wt% of V_2O_5 has the most excellent dynamic magnetic property and EM absorbing ability.

(2). Due to the small amount of V_2O_5 doping, both the static permeability $\mu_0^{'}$ and the maximum imaginary permeability $\mu_{max}^{''}$ are greatly enhanced. The large value of $\mu_0^{'}$ is contributed to the decrease of H_c.

(3). By doping with V_2O_5, perfect hexagonal-plate grains are formed, leading to a decrease in the natural resonance frequency due to the large demagnetizing effect.

(4). The bandwidth for absorption of more than 20 dB is from 3.5 to 13.8 GHz for Co10WV, from 5.0 to 15.7 GHz for Co13WV, and from 6.3 to >16.5 GHz for Co15WV. As compared with the undoped samples of Co10W, Co13W and Co15W, the maximum relative bandwidth increases by 30 %, 48 % and more than 53 %. Therefore, the composites of $BaCo_xZn_{2-x}Fe_{16}O_{27}$ $(1.0 \le x \le 1.5)$ with 1.0 wt% V_2O_5 doping are suitable candidates for EM materials used in C-, X- and Ku-bands.

(5). The great enhancement of W_{max} results from the increased contribution of magnetic loss due to large permeabilities ($\mu_0^{'}$ and $\mu_{max}^{''}$) and the additional contribution of thickness loss.

CHAPTER 7: CoZn-, NiCo- AND ZnNi-SUBSTITUTED *Y*-TYPE BARIUM FERRITES

In this work, $BaCo_xZn_{2-x}Fe_{12}O_{22}$ (CoZn-Y) and $BaZn_xNi_{2-x}Fe_{12}O_{22}$ (ZnNi-Y) with x varying from 0 to 2.0 at intervals of 0.4 have been prepared and studied systematically. In addition, $BaNi_xCo_{2-x}Fe_{12}O_{22}$ (NiCo-Y) with x=0.8, 1.0, 1.2 and 1.5 were also investigated. All samples were fabricated by a two-step solid-state reaction method as stated in Chapter 3. The microstructure, static magnetic properties, microwave electromagnetic and absorbing properties will be reported in this chapter.

7.1 XRD patterns for powder and aligned samples

XRD results from powder samples confirm that all samples are pure *Y*-type ferrites. Fig. 7-1 shows some typical XRD patterns for the powders of CoZn-, NiCo- and ZnNi-Y ferrites. The standard XRD pattern of BaY is also given in the figure based on JCPDS International Center for Diffraction Data (Nos. 19-0100 and 44-0206). The XRD results indicate that all studied ferrites are single phase with *Y*-type hexagonal structure.

The lattice parameters, *a* and *c*, of each sample are obtained by fitting the strong diffraction lines of the crystal planes of (1 1 0), (1 1 3), (1 0 13), (0 1 14), (1 1 9), (0 2 10), (2 1 13) and (2 2 0) with least squares method. Fig. 7-2 shows the parameters *a* and *c*, and unit-cell volume *V* of all samples. The values of these parameters are also listed in Table B-1, which is included in Appendix B.

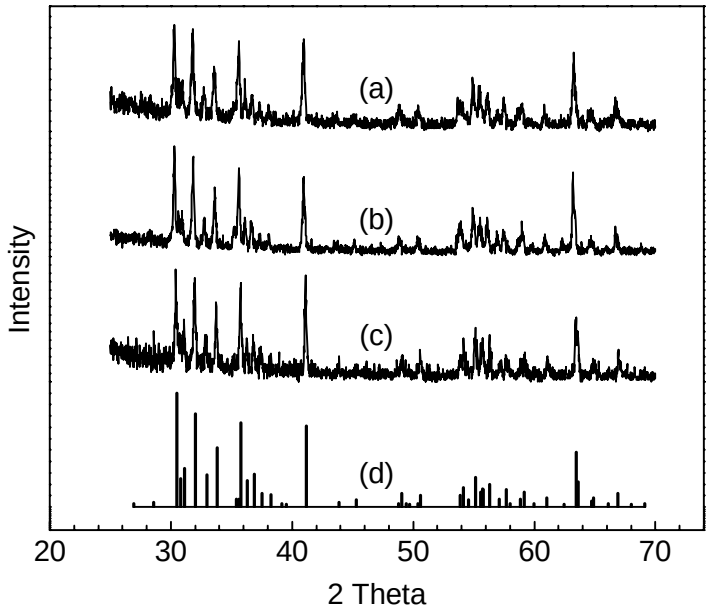

Fig. 7-1. Some typical X-ray diffraction patterns for $Ba_2Co_xZn_{2-x}Fe_{12}O_{22}$, $Ba_2Ni_xCo_{2-x}Fe_{12}O_{22}$ and $Ba_2Zn_xNi_{2-x}Fe_{12}O_{22}$ ferrites: (a) Co_2Y; (b) Ni_2Y; (c) Zn_2Y; (d) Standard pattern.

It is found that the lattice parameter *a* decreases gradually from 0.5892 to 0.5876 nm as Me_2Y is changed from Zn_2Y to Co_2Y, and continuously decreases to 0.5861 nm for Ni_2Y. The substitution of Zn for Ni leads to an increase in lattice parameter *a* from 0.5861 nm for Ni_2Y to 0.5890 nm for Zn_2Y. The same behavior is observed for the lattice parameter *c* and unit cell volume *V*. The minimum and maximum values of *V* are 3.882 nm^3 (Ni_2Y) and 3.958 nm^3 (Zn_2Y), respectively. It is known that the radii of Zn^{2+}, Co^{2+} and Ni^{2+} are 0.74 Å, 0.65 Å and 0.63 Å, respectively.[106] When the ions with smaller radii (such as 0.63 Å for Ni^{2+}) are substituted by the larger ions (such as 0.74 Å for Zn^{2+}), the lattice of crystal will be expanded, thus leading to the increase in the lattice parameters.

It should be noted that, although these three series of samples were fabricated separately, the lattice parameters and cell volume for Zn_2Y in two series (CoZn-Y and NiZn-Y) are consistent with each other within the experimental uncertainty.

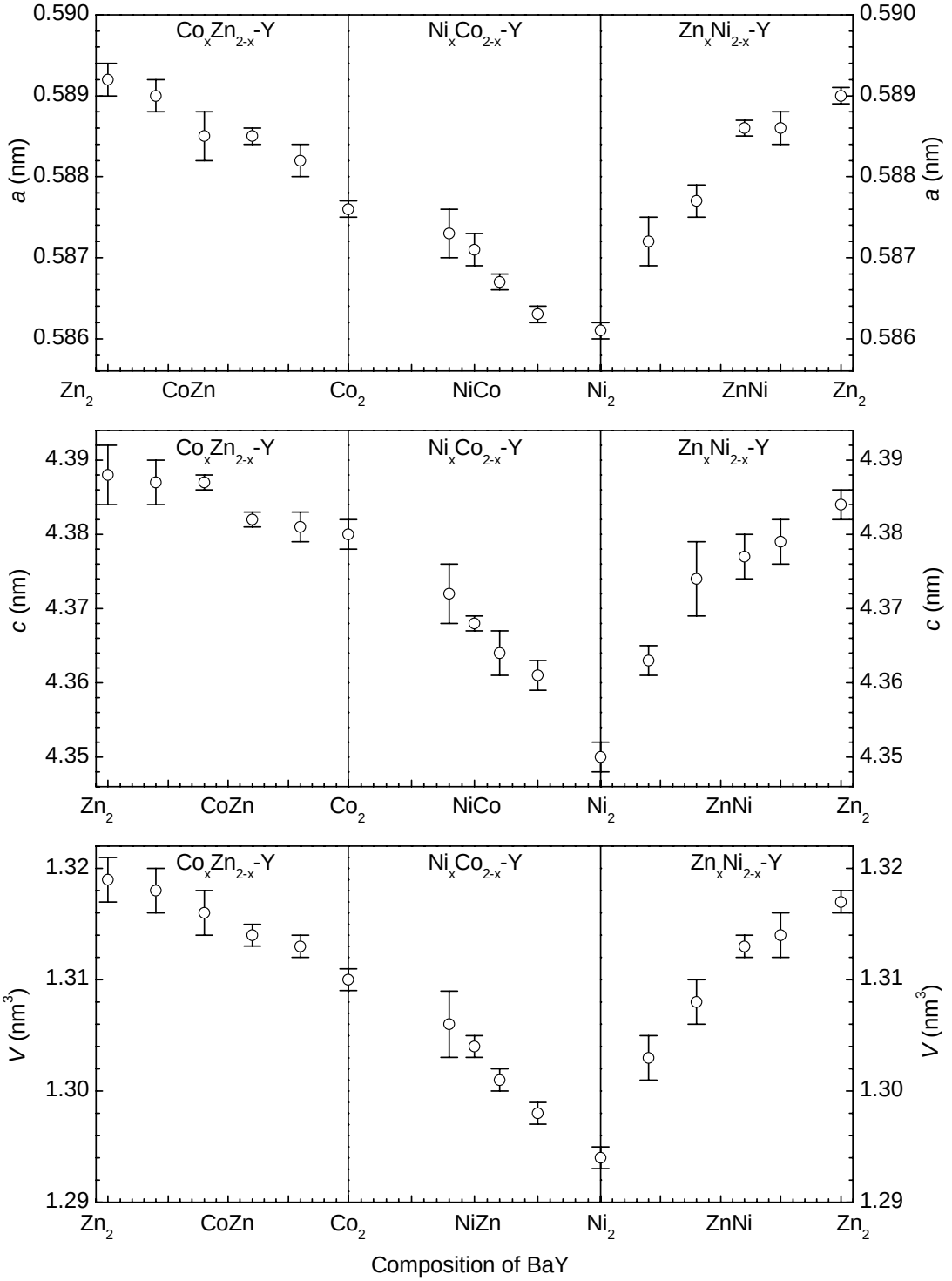

Fig. 7-2. Influence of ions substitution on lattice parameters *a* and *c*, and unit-cell volume *V* for BaY with various composition.

In order to identify the magnetocrystalline anisotropy, XRD was carried out for all aligned samples. Some typical XRD patterns are shown in Fig. 7-3 for the aligned

samples of Co_2Y, Ni_2Y and Zn_2Y as examples. For all aligned samples, the strong diffracted lines are found to be at 2θ angles of 30.5 °, 54.2 ° and 63.4 °, which are corresponding to the crystal planes of (1 1 0), (3 0 0) and (2 2 0). That is to say, the intensity of the (*h k* 0) reflection increases dramatically, whereas the others are almost vanished. Therefore, all samples are *c*-plane anisotropy at room temperature and well aligned along easy magnetization direction.

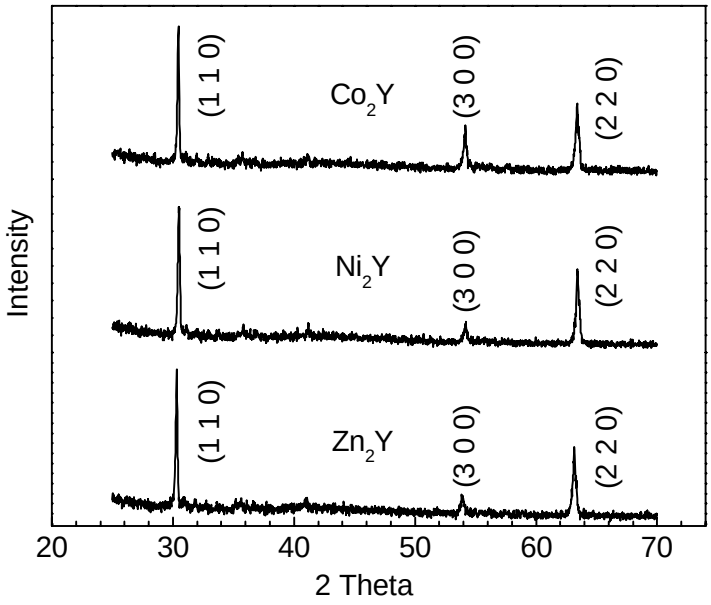

Fig. 7-3. Typical X-ray diffraction patterns for magnetically aligned samples of Co_2Y, Ni_2Y and Zn_2Y.

7.2 Static magnetic properties

7.2.1 Saturation magnetization and coercivity

The magnetization curves were measured at room temperature for all sintered samples. The applied magnetic field is 0-14 kOe and the demagnetizing corrections have been considered. The value of magnetization at the maximum applied field (14 kOe) is defined as the saturation magnetization M_s. Some typical magnetization curves are

shown in Fig. 7-4. The exact values of M_s for all samples are shown in Fig. 7-5 and Table B-2 (Refer to Appendix B).

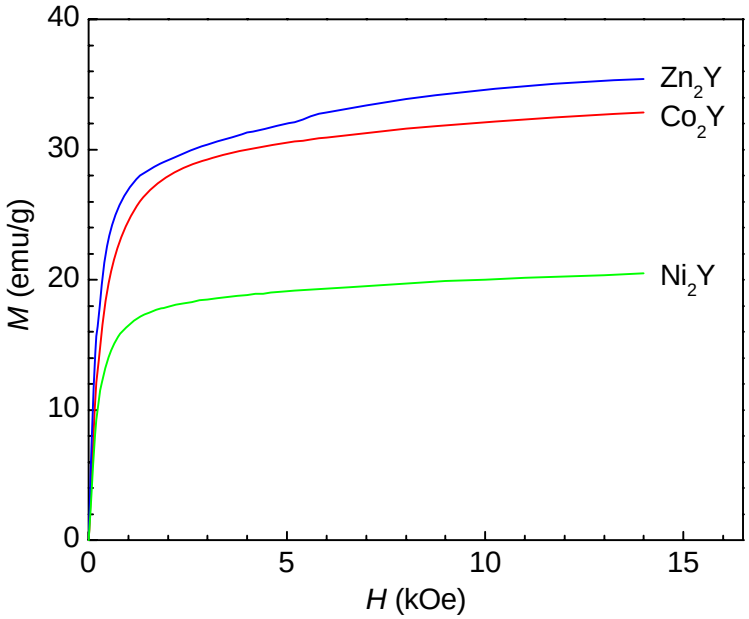

Fig. 7-4. Typical magnetization curves for sintered samples of Co_2Y, Ni_2Y and Zn_2Y.

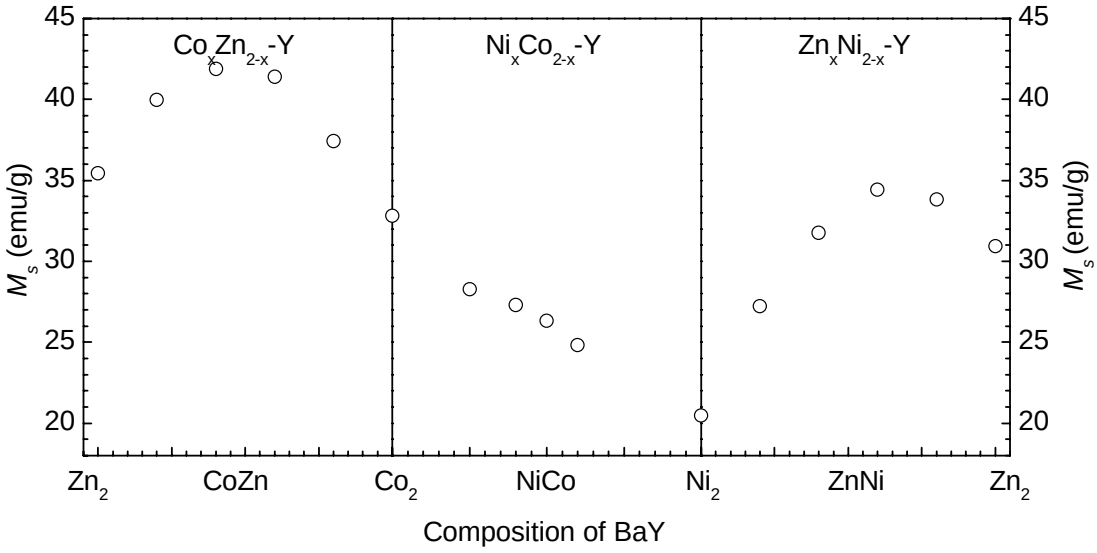

Fig. 7-5. Saturation magnetization M_s for CoZn-, NiCo- and ZnNi-substituted BaY with various substituted amounts.

For the series of Zn-substituted BaY, $Ba_2Co_xZn_{2-x}Fe_{12}O_{22}$ and $Ba_2Zn_xNi_{2-x}Fe_{12}O_{22}$, with the increase in Zn concentration, M_s is found to increase first, reach a smooth

maximum, and decrease thereafter. The maximum values of M_s, 41.9 emu/g and 34.4 emu/g, are obtained at Zn=1.2 for CoZn- and NiZn-substituted BaY systems. Similar results have been reported by Bai *et al.*[53] and Lee *et al.*.[107] In addition, Albanese *et al.* also pointed out that replacing the Zn ions by two valence ions of Cu^{2+}, Ni^{2+}, Co^{2+}, *etc.* will change the static magnetic properties.[30]

The observed variation of M_s is related with two factors: (1). Ion distribution at various sites, and (2). Decrease in Curie temperature due to Zn substitution.

It is known that Fe^{3+}, Co^{2+} and Ni^{2+} are magnetic ions, and the numbers of Bohr magnetons are 5 μB, 3 μB and 2 μB, respectively, while Zn^{2+} is a kind of nonmagnetic ion.[108] The saturation magnetization of BaY ferrite at 0 K strongly depends on the distribution of these ions among the six different sublattice sites ($3a_{VI}$, $6c_{VI}$, $3b_{VI}$, $18h_{VI}$, $6c_{IV}$ and $6c_{IV}$*). It has been known that the $6c_{VI}$, $6c_{IV}$ and $6c_{IV}$* sites are spin-down, while the others are spin-up. The magnetic ions occupying the spin-up sites will provide positive magnetization, while the ions locating at the spin-down sites give negative magnetizations (the direction of magnetization is opposite to the applied magnetic fields). Nonmagnetic ions Zn^{2+} locating at $6c_{VI}$, $6c_{IV}$ and $6c_{IV}$* sites lead to a decrease in the negative magnetization, and thus increase net or total magnetization. It was reported that in the series of CoZn-Y, and the saturation magnetization M_s increases linearly with Zn concentration at low temperature (77 K), and Zn_2Y has the highest saturation magnetization.[107, 109] In addition, Co^{2+} and Ni^{2+} ions preferentially occupy the octahedral sites with spin-up. As Zn^{2+} concentration increases, the concentration of magnetic ions (Co^{2+} or Ni^{2+}) decreases, which leads to a decrease in magnetization.

On the other hand, nonmagnetic ion substitution for magnetic ion will weaken the super exchange interaction, thus lead to the reduction of the Curie temperature T_c. T_c for Zn_2Y is as low as about 130 ˚C, while relatively high T_c of 340 ˚C and 390 ˚C are reported for Co_2Y and Ni_2Y, respectively. Lee *et al.*[107] also indicated that T_c decreases linearly with increasing Zn concentration in CoZn-Y series. Therefore, near room temperature, the saturation magnetization M_s will decrease more rapidly for the samples with higher Zn concentration on account of the effect of thermal agitation. Hence, M_s does not continuously increase with Zn content. Instead, it decreases when Zn concentratin is larger than 0.8.

For CoNi-substituted BaY, M_s almost linearly decreases as $Ba_2Ni_xCo_{2-x}Fe_{12}O_{22}$ is changed from Co_2Y to Ni_2Y. The values of M_s are about 32.8, 26.3 and 20.5 emu/g for Co_2Y, NiCoY and Ni_2Y ferrites. This variation has its origin in the lower moment for Ni^{2+} (2 μB) than that for Co^{2+} (3 μB). Therefore, M_s decreases with the substitution of Co^{2+} by Ni^{2+}.

M-H loops for all sintered samples were measured at room temperature. The applied field is between -14 and +14 kOe. Some typical *M-H* loops in the applied filed of -0.5 kOe to +0.5 kOe are shown in Fig. 7-6. The values of H_c for all samples are shown in Fig. 7-7 and Table B-2 (Refer to Appendix B). It is obvious that H_c is strongly dependent on the ions substitution.

The coercivity H_c for Zn_2Y is about 7.0 Oe, which is the smallest value among all samples. With the substitution of Co^{2+} or Ni^{2+} for Zn^{2+}, H_c increases greatly. For the ferrites with terminal compositions of $Ba_2Co_2Fe_{12}O_{22}$ and $Ba_2Ni_2Fe_{12}O_{22}$, H_c is 39.1 and 36.6 Oe, respectively.

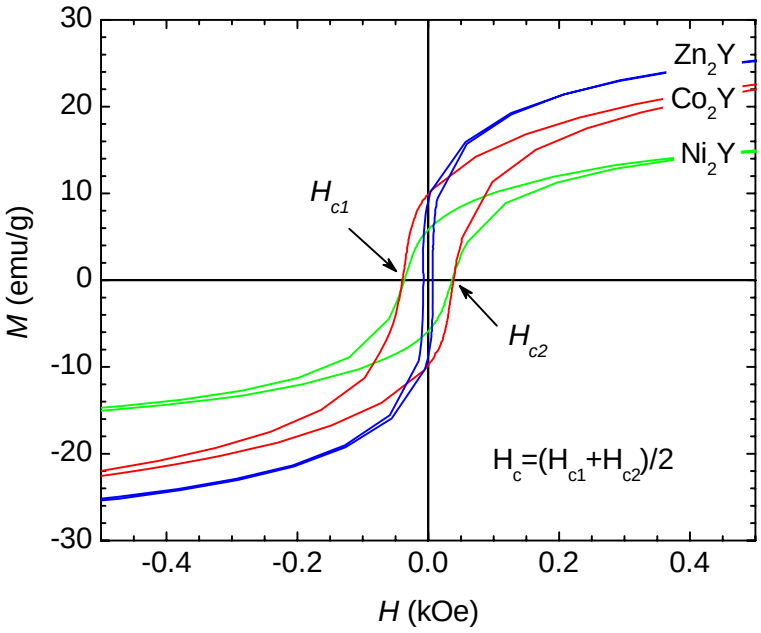

Fig. 7-6. *M-H* loops for the sintered samples of Co_2Y, Ni_2Y and Zn_2Y.

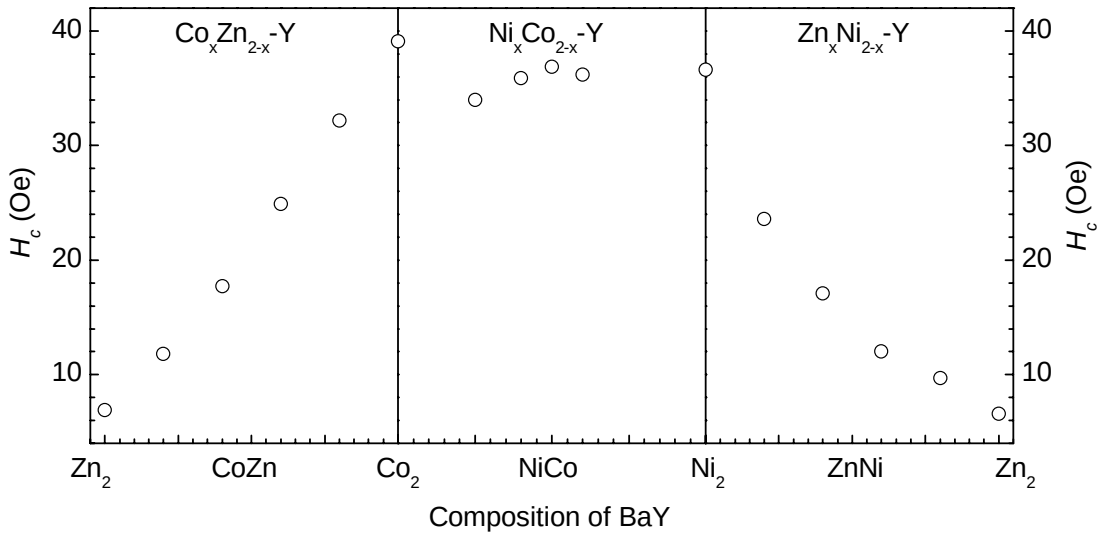

Fig. 7-7. Coercivity H_c for CoZn-, NiCo- and ZnNi-substituted BaY with various substituted amounts.

For *Y*-type barium ferrites, the in-plane anisotropy field H_ϕ is usually very small (about 0.5 Oe for Zn_2Y at room temperature[110]). Thus, the coercivity H_c is mainly controlled by magnetization rotation. Co^{2+} or Ni^{2+} substituting for Zn^{2+} will enhance

magnetic planar anisotropy, which will make the rotation of the magnetic moment more difficult. It is reported that H_ϕ is about 200 Oe for Co_2Y,[95] 400 times larger than Zn_2Y. Therefore, coercive force H_c increases as the Co or Ni content increases.

7.2.2 Anisotropy field

To obtain the out-of-plane anisotropy field H_θ, the easy and hard magnetization curves, which are corresponding to the direction of parallel and perpendicular to the alignment direction, were measured at room temperature for aligned samples. All samples were demagnetized before testing. The maximum applied magnetic field is 14 kOe. Fig. 7-8 shows the typical magnetization curves along two directions for the samples of Co_2Y and Zn_2Y. For Zn_2Y, the easy and hard magnetization curves are joined together at certain magnetic field; the field corresponding to the intersection of two curves is defined as the anisotropy field H_θ, which is about 9.2 kOe. However, for Co_2Y, a field of 14 kOe is insufficient to induce magnetic saturation along the hard magnetization direction due to the large out-of-plane anisotropy field; hence, two magnetization curves are disconnected. In this case, it is assumed that the dependence of *M(H)* on *H* is linear in the high-field region, thus H_θ is estimated roughly by extrapolating the measured curves, as shown in Fig. 7-8.

Figure 7-9 shows the results of H_θ for each sample. The values are also listed in Table B-2, which is included in Appendix B. It should be noted that, due to the small magnetic field applied, there is a possibly large experimental error for the absolute value of H_θ. However, the dependence of H_θ on composition is believable. In addition, the values are also consistent with the results obtained from ferromangnetic resonance (FMR).[30]

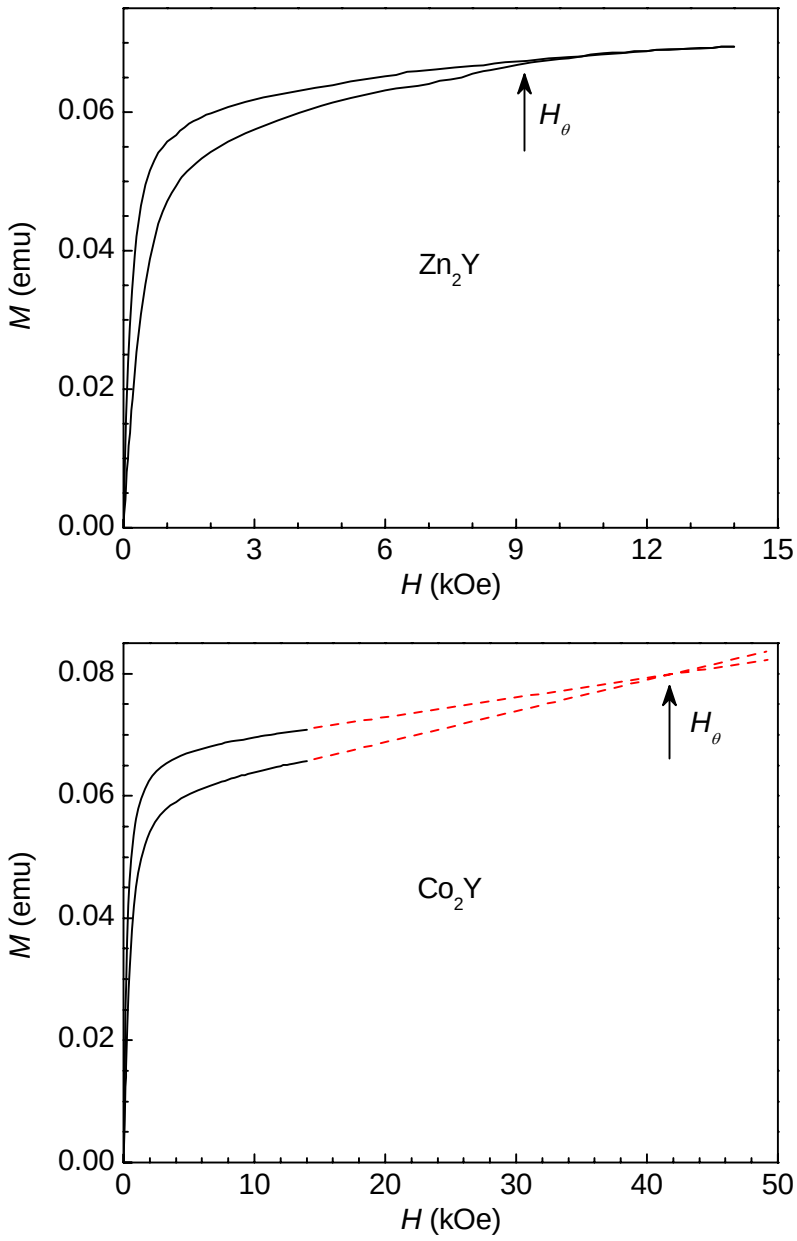

Fig. 7-8. The magnetization curves parallel and perpendicular to the alignment direction for the aligned samples of Zn_2Y and Co_2Y.

All CoZn-, NiCo- abd ZnNi-substituted BaY ferrites have *c*-plane anisotropy. Co^{2+} ions have much larger contribution to magnetocrystalline anisotropy than Ni^{2+} and Zn^{2+} ions.[30] Therefore, the anisotropy field H_θ is much larger for Co_2Y than for Ni_2Y and Zn_2Y. With the substitution of Zn or Ni for Co, the value of H_θ decreases rapidly from about 41.5 kOe for Co_2Y to 9.0 kOe for Zn_2Y or to18.0 kOe for Ni_2Y. On the

other hand, Ni_2Y and Zn_2Y have almost the same magnetocrystalline anisotropy; the values of K_1+2K_2 are about -0.9×10^5 J/m^3 and -1.0×10^5 J/m^3 for Ni_2Y and Zn_2Y, respectively.[111] However, the saturation magnetization M_s at room temperature for the former is much smaller than the one for the latter, which are 20.47 and 30.94 emu/g, respectively. It is well known that H_θ is related not only to the anisotropy constants, but also to the saturation magnetization by the relation of $H_\theta = -\frac{2(K_1+2K_2)}{M_s}$. Hence, as compared with Zn_2Y, smaller M_s leads to a larger anisotropy field H_θ for Ni_2Y.

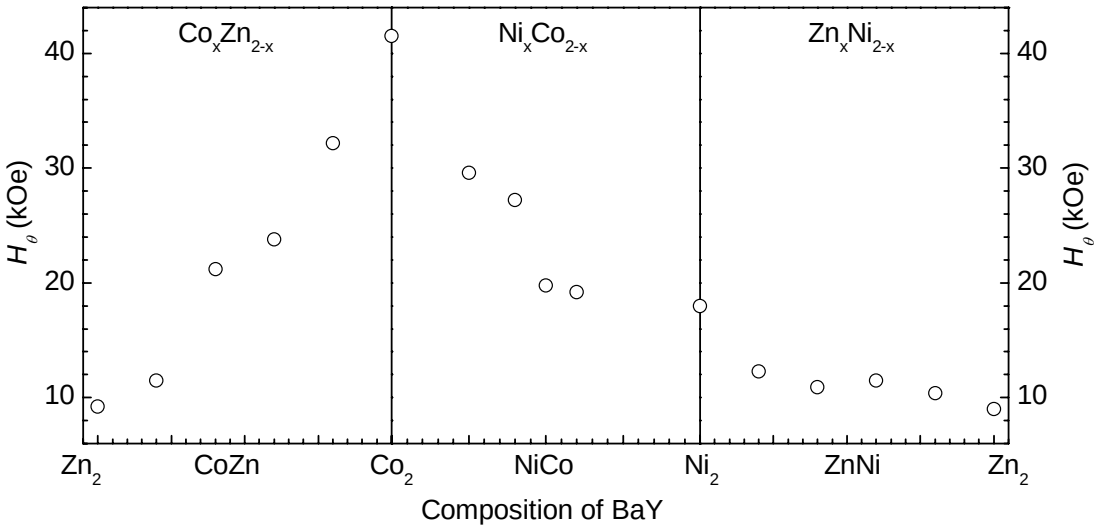

Fig. 7-9. Anisotropy field H_θ for *Y*-type ferrites with different composition, $Ba_2Co_xZn_{2-x}Fe_{12}O_{22}$ (x=0, 0.4, 0.8, 1.2, 1.6 and 2.0), $Ba_2Ni_xCo_{2-x}Fe_{12}O_{22}$ (x=0.5, 0.8, 1.0 and 1.2) and $Ba_2Zn_xNi_{2-x}Fe_{12}O_{22}$ (x=0, 0.4, 0.8, 1.2, 1.6 and 2.0).

7.3 Electromagnetic properties

7.3.1 Complex permittivity and permeability spectra

The dielectric properties of composites filled with 50 vol% of BaY ferrite powders were characterized from 0.5 to 16.5 GHz. The values of complex permittivity (ε' and

ε") do not show observable dependence on the composition of the ferrites. Furthermore, for each composite, the complex permittivity almost remains constant over the investigated frequency range. For all composites, the real permittivity ε' is about 7.2, while the imaginary part ε" is about 0.3 over the whole frequency range. The typical complex permittivity spectra are shown in Fig. 7-10 for composites of Co_2Y, Ni_2Y and Zn_2Y.

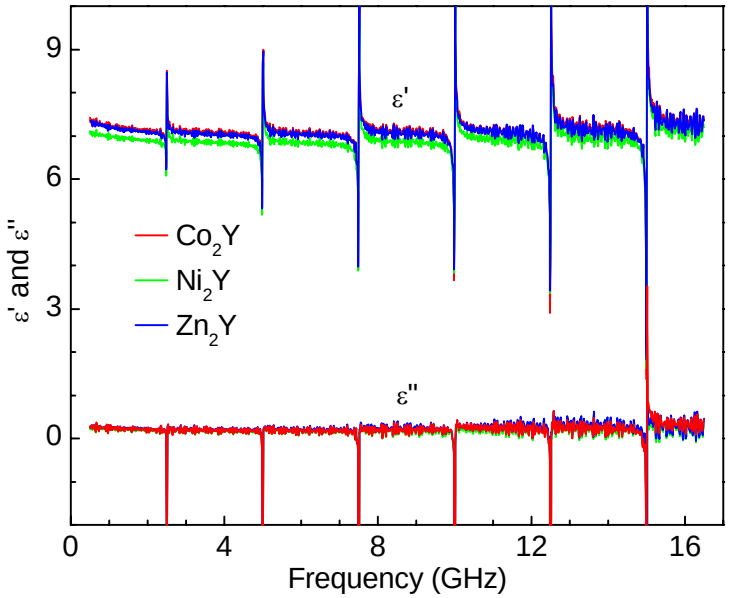

Fig. 7-10. Typical complex permittivity spectra in the frequency of 0.5-16.5 GHz for Co_2Y, Ni_2Y and Zn_2Y.

The dynamic magnetic properties for composites of CoZn-, NiCo- and ZnNi-substituted BaY ferrite powders were characterized from 0.01 to 16.5 GHz. The permeability spectra for all samples are shown in Fig. 7-11. Several important high-frequency parameters are listed in Table B-3 (Refer to Appendix B). The static permeability, $\mu_0^{'}$, is defined as the real permeability at 0.01 GHz. f_{r1}, f_{r2} and f_{r3} are the resonance frequencies ($f_{r1} > f_{r2} > f_{r3}$). Based on the Fig. 7-11 and Table B-3,

three obvious characteristics can be observed.

Firstly, the number of resonance peaks is changed with the substitution. For most of the composites, such as the series of CoNi-Y, there are two obvious resonance peaks, namely P_1 and P_2. This is completely consistent with the case for *W*-type ferrites, which has been discussed in the above three chapters. However, for the Zn-contained BaY (especially for high Zn concentration ferrites, such as Zn_2Y), a third peak (P_3) is visible, which is located around 0.1 GHz. Therefore, it is necessary to verify the resonance mechanism for these peaks. The detailed discussion will be presented in the next section.

Secondly, resonance frequencies f_{r1} and f_{r2} are greatly shifted with the substitution, while f_{r3} almost keeps constant (~0.1 GHz) with the variation of composition. Take the series of CoZn-Y for example. With the substitution of Co for Zn, both f_{r1} and f_{r2} are shifted to higher frequency. For the composite of Zn_2Y, P_1 and P_2 are overlapped; thus only one resonance peak is observable, which is located at about 1.7 GHz. However, for the composite of Co_2Y, f_{r1} is beyond 16.5 GHz and f_{r2} is about 7.1 GHz.

Finally, the values of $\mu_0^{'}$ and $\mu_{\max}^{''}$ are also significantly changed with the substitution of Zn for Co or Ni. For the composites of CoZn-Y, with the increase in Zn^{2+} from 0 to 2.0, $\mu_0^{'}$ increases from 1.6 to 4.7, and $\mu_{\max}^{''}$ increases from 0.38 to 1.6. Similarly, for the series of ZnNi-Y, $\mu_0^{'}$ and $\mu_{\max}^{''}$ are 2.6 and 4.8 for Ni_2Y and Zn_2Y, respectively, and the corresponding $\mu_{\max}^{''}$ are 0.84 and 1.6.

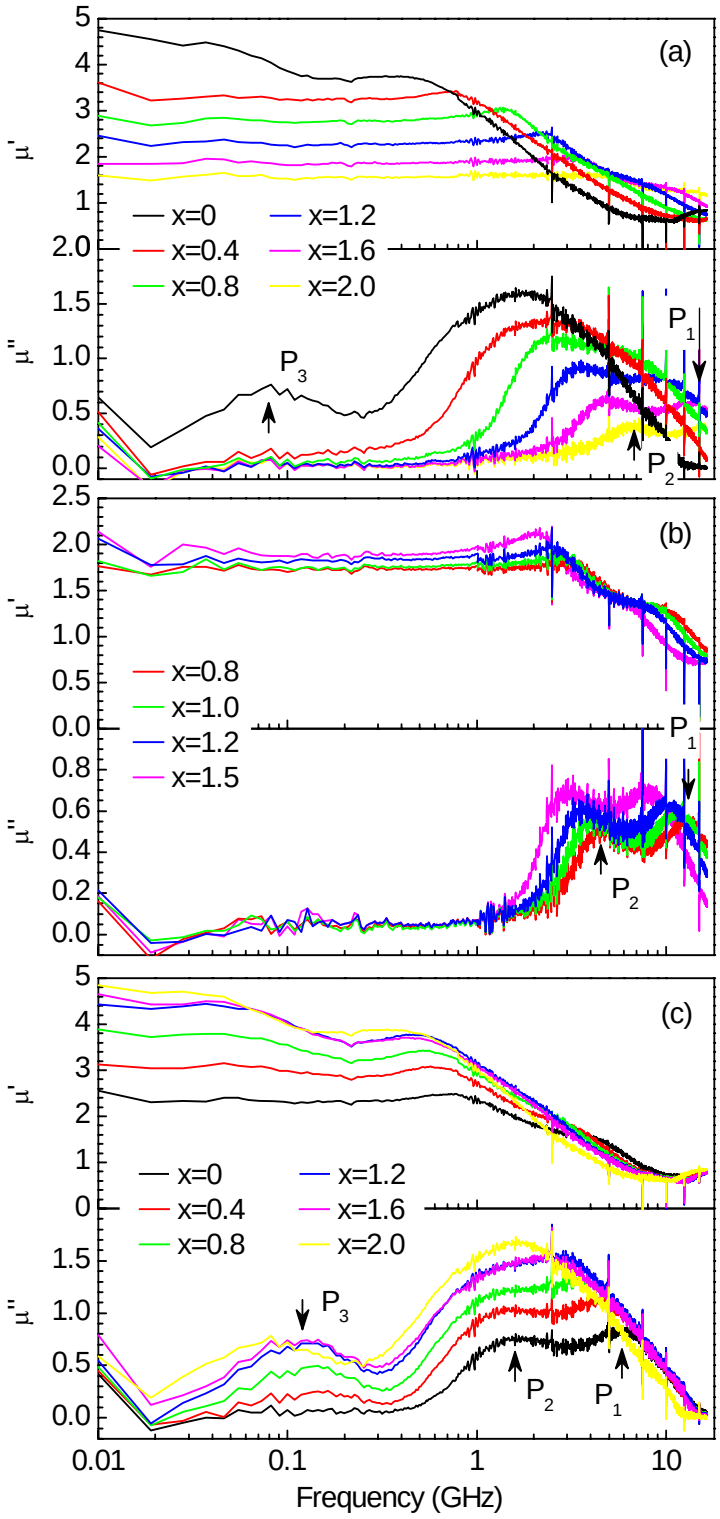

Fig. 7-11. The complex permeability spectra in the frequency of 0.01-16.5 GHz for: (a). CoZn-, (b). NiCo- and (c). ZnNi-substituted BaY.

7.3.2 Identification of resonance mechanisms

In order to identify the type of resonance, natural resonance or domain wall resonance, single domain particles for the ferrites of $Ba_2Zn_xNi_{2-x}Fe_{12}O_{22}$ with x=0.8 and 2.0 were prepared by the high energy ball-mill. Based on SEM morphologies, most of particles have a size below 1 μm, which reaches the critical diameter of domain (about 0.6-1.0 μm) for hexaferrites.[112] Hence, for the composites filled with these ferrite particles, the domain wall resonance will not occur.

The composite samples were prepared by mixing 50 vol% of the ball-milled ferrite powders with epoxy resin. The complex permeability spectra are shown in Fig. 7-12. For comparison, the permeability spectra for composites with original particles are also included in this figure. There are three resonance peaks for the samples without ball-milling. However, for the composites with ball-milled powders, the resonances peaks at low frequency (P_2 and P_3) vanish, while the peak at high frequency (P_1) is still observable. Hence, it can be concluded that P_1 is contributed by natural resonance, and P_2 and P_3 originate from domain wall resonance.

In fact, J. Verwell has addressed the possibility of two domain wall resonances for some specific ferrite materials.[113] He pointed out that, in the case of spinel, the abnormal wall resonance usually occurs at the low-frequency side of the spectrum, between 1 kHz and 1 MHz. For example, the abnormal wall resonance occurs at 100 kHz and 1 MHz for $Y_3Fe_5O_{12}$ and $Y_3Si_{0.05}Fe_{0.95}O_{12}$, respectively. Some similar investigation has been conducted by other researchers.[38, 49, 53, 107] Kwon *et al.*[38] investigated the complex permeability of NiZn-substituted BaY ferrites from 200 MHz to 14 GHz. It was not surprised that they could not observe the third resonance

peak located at about 100 MHz, which is beyond the measured range. Bai *et al.*[53] reported the dynamic magnetic property for CuZn-Y in the range of 1 MHz-1 GHz. As the measured maximum frequency is too low (1 GHz), they didn't notice the existence of natural resonance peak over 1 GHz. Thus, they made an abrupt conclusion that the peaks at 70 MHz and about 1 GHz were contributed by domain wall and natural resonances, respectively. In fact, both peaks they observed result from domain wall resonance. Based on the results of this work, the natural resonance should be larger than 2 GHz.

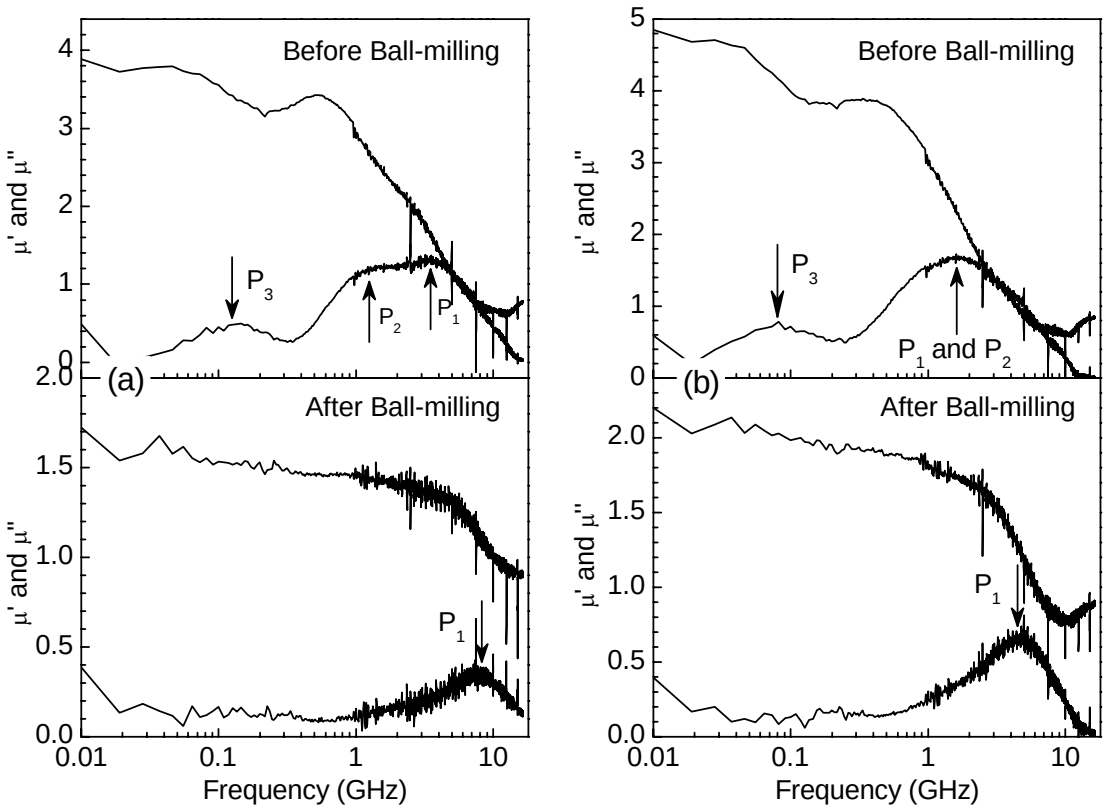

Fig. 7-12. The complex permeability spectra in the frequency of 0.01-16.5 GHz for composites mixed with the ferrites powders before and after ball-milling: (a) $Ba_2Zn_{0.8}Ni_{1.2}Fe_{12}O_{22}$ and (b) $Ba_2Zn_2Fe_{12}O_{22}$.

The mechanism for the abnormal wall resonance has been developed by Clogston.[114] It is supposed that the magnetic energy levels of the magnetic ions depend on the

orientation of the magnetization. For each orientation there will be an equilibrium Boltzmann distribution. In a moving wall, the magnetization changes its direction, and hence the energy levels, so that the equilibrium distribution changes. A thermally activated redistribution will occur in a finite relaxation time τ, causing the magnetization to lag behind the applied field. The maximum loss will occur at the frequency defined by $2\pi\tau/f$ =1.

7.3.3 Relationship between resonance frequency and anisotropy field

Based on Fig. 7-11, it is obvious that the resonance frequency f_{r1} is strongly dependent on the ions substitution. In the above section, it has been confirmed that f_{r1} is the frequency of natural resonance.

With the substitution of Co or Ni for Zn, f_{r1} is significantly shifted to high frequency. For example, f_{r1} is located around 2 GHz for Zn_2Y, while 6.1 GHz and beyond 16.5 GHz for Ni_2Y and Co_2Y, respectively. For the series of $Ba_2Ni_xCo_{2-x}Fe_{12}O_{22}$, f_{r1} is decreased with the increase in x. As discussed in Chapter 4, the frequency of natural resonance is tightly related with the anisotropy field H_θ. Fig. 7-13 shows that, to a good approximation, a linearly relation between natural resonance frequency f_{r1} and anisotropy field H_θ is given by

$$f_{r1} = \frac{\gamma}{2\pi}\beta^{1/2}H_\theta$$

where β is the proportional coefficient of H_ϕ to H_θ. From the slope of the fitting line, it is obtained that $\frac{\gamma}{2\pi}\beta^{1/2} = 0.389$. Hence, β is roughly estimated at $\beta = 0.019$, which

is much smaller than 0.076 for CoZn-substituted BaW. This implies that, for the same H_θ, the in-plane anisotropy field H_ϕ for BaY ferrites is much smaller than BaW ferrites. More importantly, similar to the BaW ferrites, the natural resonance frequency for BaY is closely related with the anisotropy field H_θ. Thus, the natural resonance frequency can be effectively controlled by the suitable Co^{2+} concentration, which benefits for design of EM materials used in various frequency bands.

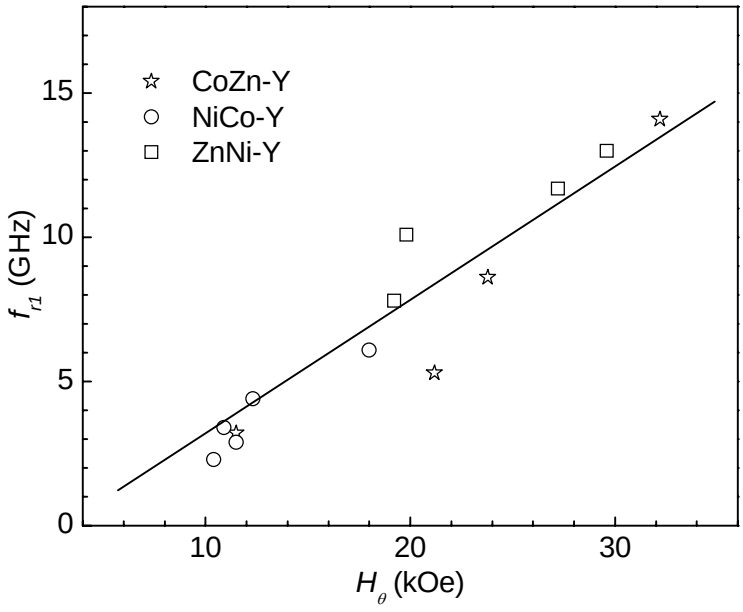

Fig. 7-13. The dependence of natural resonance frequency f_{r1} on anisotropy field H_θ for CoZn-, NiCo- and ZnNi-substituted BaY.

7.4 Reflection properties

The absorption characteristics of all composites were calculated with the data of μ and ε based on the metal-backed single-layer model. Fig. 7-14 shows the frequency dependence of the reflection loss at optimum thickness t_o for each sample. The values of t_o, f_{low}, f_{up} and the corresponding $W_{\max}$ are listed in Table B-4 (Refer to Appendix B).

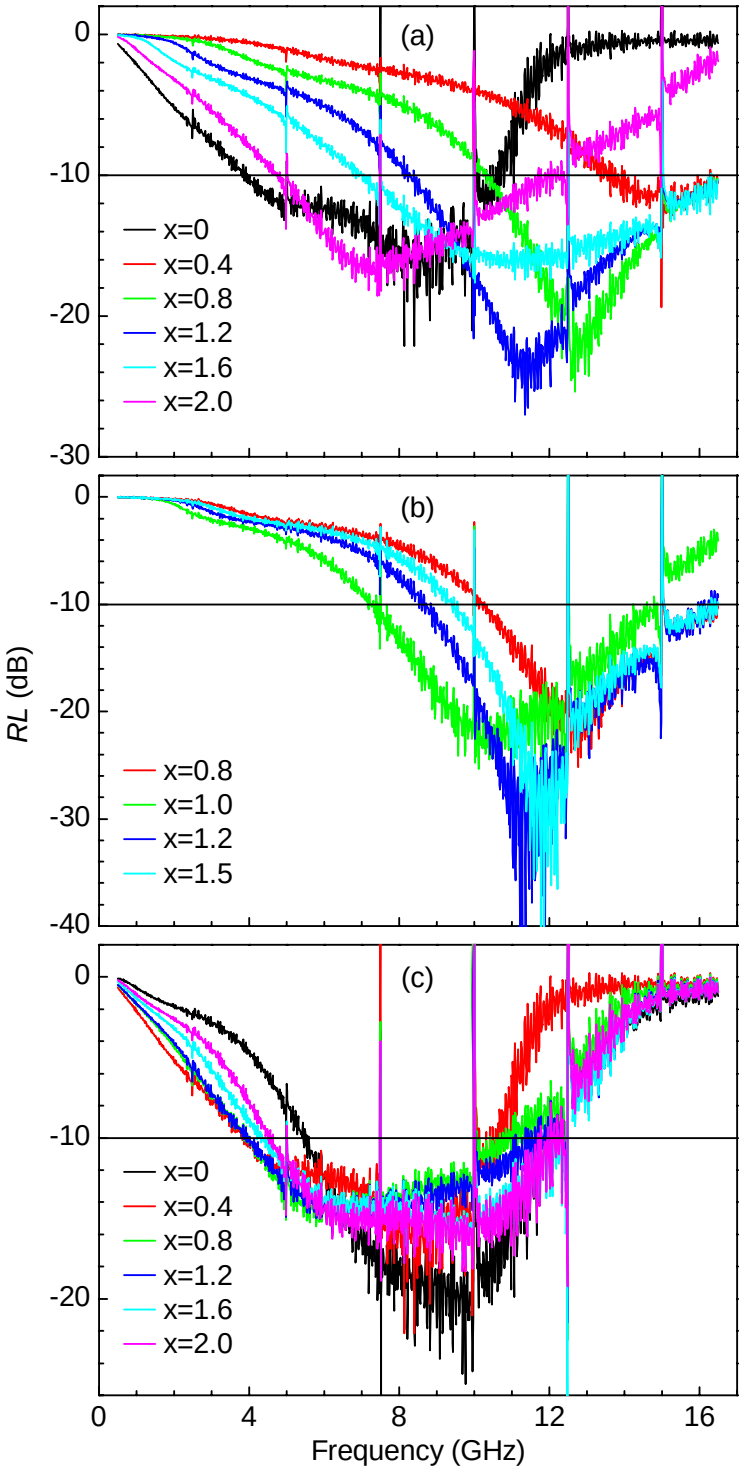

Fig. 7-14. Reflection characteristics for BaY composites at the optimum thickness. (a) $Ba_2Co_xZn_{2-x}Fe_{12}O_{22}$, (b) $Ba_2Ni_xCo_{2-x}Fe_{12}O_{22}$, and (c) $Ba_2Zn_xNi_{2-x}Fe_{12}O_{22}$.

Based on Fig. 7-14 and Table B-4, it can be deduced that the absorbing frequency band is greatly changed with the various ions substitution. Let's take CoZn-

substituted BaY for example. With the substitution of Co^{2+} for Zn^{2+}, the frequency band for -10 dB reflection loss is modified from 3.5-9.9 GHz for Zn_2Y to 13.6-16.5 GHz for Co_2Y. The frequency band for -10 dB absorption for Ni_2Y is 5.4-12.1 GHz. It seems that the composites with high Zn^{2+} concentration are suitable for C-band, while those with high Co^{2+} concentration are for Ku-band, and those with high Ni^{2+} concentration are suitable for middle frequency band, such as X-band. These are good EM materials with low reflectivity and broad bandwidth at various frequency bands.

In addition, ZnNi-substituted BaY has better absorbing property for use as EM materials with broad absorption bandwidth. Especially for the composite of $Ba_2Zn_{1.2}Ni_{0.8}Fe_{12}O_{22}$, the bandwidth for absorption of more than 10 dB is from 3.9 to 11.8 GHz, which covers the C- and X-bands. The corresponding relative bandwidth is larger than 3 and the optimum thickness is about 3.3 mm.

7.5 Conclusions

Y-type hexaferrites with series of $Ba_2Co_xZn_{2-x}Fe_{12}O_{22}$, $Ba_2Ni_xCo_{2-x}Fe_{12}O_{22}$ and $Ba_2Zn_xNi_{2-x}Fe_{12}O_{22}$ (x varying from 0 to 2.0) have been prepared by the solid-state reaction method. The microstructure, static and dynamic magnetic properties, and microwave absorbing properties have been studied systematically.

For CoZn- and ZnNi-substituted BaY ferrites, with the increase in Zn concentration, the saturation magnetization M_s first increases, reaches a maximum and then decreases. This characteristic may be related with two factors: (1). The distribution of Zn^{2+} ions among the six various sites in BaY structure, and (2). The decrease in Curie temperature due to Zn^{2+} substitution. For CoNi-substituted BaY ferrites, the slight decrease in M_s with Ni substitution is attributed to the smaller magnetic moment for

Ni^{2+} (2 μB) than for Co^{2+} (3 μB) ions.

Co_2Y has the maximum anisotropy field H_θ of about 40 kOe, and H_θ rapidly decreases with the substitution of Zn for Co. This behavior originates from the large contribution of Co^{2+} to the magnetocrystalline anisotropy. In the series of ZnNi-Y, the slight decrease in H_θ is associated with the decrease in M_s with Zn substitution.

It was found that Zn substitution has a contribution to large permeabilities $\mu_0^{'}$ and $\mu_{\max}^{''}$, while Co substitution can effectively shift the natural resonance to high frequency. Among all investigated composites, Co_2Y has the highest natural resonance frequency of over 16.5 GHz and Zn_2Y has the maximum $\mu_0^{'}$ of about 4.7.

Three magnetic resonance peaks for composites of BaY are observed. The resonance mechanism for each peak has been identified. It was found that the highest frequency peak is for natural resonance and the other low frequency peaks are contributed by domain wall resonance. In addition, the linear relationship between the natural resonance frequency and anisotropy field has also been verified, which is very useful for the design of EM materials in various frequency bands.

The predicted *RL* shows that the composite of $Ba_2Zn_{1.2}Ni_{0.8}Fe_{12}O_{22}$ has the best absorbing property for use as EM materials. The bandwidth for absorption of more than 10 dB is from 3.9 to 11.8 GHz, and the relative bandwidth is over 3 at a thickness of 3.3 mm. On the other hand, the absorbing frequency band is changed greatly with the various ions substitution. The composites with high Zn^{2+} concentration are suitable for C-band, while those with high Ni^{2+} concentration are suitable for X-band, and those with high Co^{2+} concentration are for Ku-band.

CHAPTER 8: CONCLUSIONS AND SUGGESTIONS FOR FUTURE WORK

8.1 Conclusions

The main aim of the work presented in this thesis was to develop barium hexaferrites for microwave absorbing application. In view of the perfect static magnetic property of BaW, CoZn-substituted *W*-type barium hexaferrites, $BaCo_xZn_{2-x}Fe_{16}O_{27}$ with x varying from 0 to 2.0, were first investigated for microwave absorption. The results showed that the resonance frequency and microwave absorbing bandwidth are modified with the increase in Co substitution. This variation can be explained by the change of magnetocrystalline anisotropy, which results from the large contribution of *c*-plane anisotropy of Co^{2+} ions.

In practical applications, composites mixed by ferrite powders and polymer are usually used instead of ferrites. Thus, the effect of ferrite concentration on electromagnetic and microwave absorbing properties were discussed. Based on the results of the investigation on $BaCo_xZn_{2-x}Fe_{16}O_{27}$ (Chapter 4), the ferrites with x=0.7 and 1.0 were found to be suitable candidates for microwave absorbing materials, so these compounds were chosen for mixing with epoxy resin. The ferrite volume concentration was varied from 25 to 50 %. The results showed that the composite filling with 50 vol% of ferrite has excellent microwave absorbing performance with suitable flexibility and density. Therefore, the ferrite concentration for all composites investigated thereafter was fixed as 50 vol%.

For ferrites with excellent absorbing ability, high permeability is demanded. Hence, in order to enhance the permeability, the effect of various oxides doping for BaW were systematically investigated. The results showed that V_2O_5 is the most promising candidate for enhancing microwave absorbing performance. Thus, $BaCoZnFe_{16}O_{27}$ doped with various amounts of V_2O_5 (0-1.5 wt%) were systematically investigated. With small amounts of V_2O_5 doping, the permeability increases and the resonance frequency shifts to the low frequency. The large permeability results from the significant decrease of coercivity and the shift of f_r is induced by the change of crystal shape. In addition, $BaCo_xZn_{2-x}Fe_{16}O_{27}$ ferrites (x=1.3 and 1.5) doped with 1.0 wt% of V_2O_5 were investigated. It was found that the microwave properties of ferrites with various Co concentrations are enhanced with V_2O_5 doping, and these ferrites are suitable for use as EM materials in different frequency bands.

It is well known that most of BaY ferrites have *c*-plane anisotropy, and *c*-plane anisotropy is necessary for microwave absorbing materials. Thus, BaY substituted with various metal ions was investigated in the final part of this study. One of the important findings for this part of the study is the coexistence of three resonance peaks in permeability spectra for NiZn-substituted BaY. These three peaks are located at different frequency range. The highest frequency peak results from natural resonance and the other two peaks are both contributed by domain wall resonance. The predicted *RL* shows that the composites with high Zn^{2+} concentration are suitable for C-band, while those with high Ni^{2+} concentration are suitable for X-band, and those with high Co^{2+} concentration are for Ku-band. In addition, it was also found that the composite with 50 vol% of $Ba_2Zn_{1.2}Ni_{0.8}Fe_{12}O_{22}$ powders has the best absorbing property for use as EM materials. The bandwidth for absorption of more than 10 dB is

from 3.9 to 11.8 GHz, and the relative bandwidth is lager than 3 with a thickness of 3.3 mm.

The main contributions of this study are discussed as follows.

(1). This is a systematical study on the effect of oxides doped in BaW. Ten kinds of oxides have been investigated and compared. The results have shown that V_2O_5 is the most promising candidate to enhance the absorbing performance for BaW. Furthermore, $BaCo_xZn_{2-x}Fe_{16}O_{27}$ doped with 1.0 wt% of V_2O_5 have excellent absorbing behavior and the absorbing band can be effectively modified with substituted amount x, which successfully satisfied the need of EM materials with wide absorbing band covering various frequency for practical applications.

(2). There are two kinds of resonance mechanisms, natural resonance and domain wall resonance. For BaW and most of BaY composites, there are two resonance peaks. The peak at higher frequency is attributed to natural resonance, while the other at lower frequency results from domain wall resonance. However, for BaY composites with large Zn concentration, the occurrence of three magnetic resonance peaks was observed. It was verified that the highest frequency peak is for natural resonance and the other two low frequency peaks are contributed by domain wall resonance.

(3). There are two kinds of EM absorption mechanisms, magnetic loss and thickness loss (quarter wavelength effect); thus two dips were observed in mostly RL_{min}-t curves, especially for the composites with large ferrite concentration. The location of the absorbing peak originated from magnetic loss is tightly related with the natural resonance frequency. However, for the composites with low ferrite content, magnetic loss is negligible and thickness loss is the major contribution of absorption. In this

case, only one dip was observed in RL_{min}-t curves. Normally, for EM materials with large absorbing band, besides the magnetic loss, the thickness of composites also makes an important contribution on the reflection loss.

(4). It was found that the crystalline anisotropy is modified with the suitable ions substitution in hexaferrites, leading to a great shift of natural resonance frequency. For BaW and BaY with *c*-plane anisotropy, a linear relationship between the natural resonance frequency and anisotropy field has been verified. This result presents an effective way to control the location of absorbing frequency band, which is very useful for the design of EM materials covering various frequency bands. In addition, the natural resonance frequency is also related with the shape of ferrite particles.

(5). With the investigation on composites with various ferrites concentration, the most suitable volume concentration of ferrite powders for practical applications was pointed out, which has significant contribution for developing ferrites as absorbing materials.

8.2 Suggestions for future work

There are some interesting directions for future work. The directions range from direct extensions of current work to search of new materials for microwave absorption.

(1). V_2O_5 doping in BaY. In this thesis, it has been shown that V_2O_5 can effectively improve the absorbing properties for BaW. As we know, BaY has been attracted much attention for microwave absorption due to its intrinsic *c*-plane anisotropy. Therefore, the effect of V_2O_5 doping in BaY should be explored.

(2). Nanocomposite materials. For decades, researchers have been searching for soft

magnetic materials with high saturation magnetization and high permeability. Metallic magnetic materials are promising candidates with high saturation magnetization and low coercivity. However, due to their metallic characteristics, the eddy current generation severely limits the application at high frequencies. It is expectable that one may obtain high permeability in magnetic nanocomposites while suppress the negative effect of eddy current by coating an insulating shell on the surface of its soft magnetic metal nanoparticle cores. There are some studies involving the preparation, structure, and properties of magnetic nanoparticles coated with protective shells in the past decade.[115, 116, 117, 118] It was reported that the insulated shell gives an improvement in EM performance at high frequency over conventional soft magnetic materials. The magnetic properties of the nanocomposites with insulated shells remain relatively stable over a wide range of frequencies. Therefore, nanocomposite materials are promising candidates for microwave absorption and shielding materials.

APPENDIX A

Various Oxides Doping in BaW

A.1 Crystal structure and static magnetic properties

$BaCoZnFe_{16}O_{27}$ doped with 1.0 wt% of various oxides were prepared using solid-state reaction. For comparison, the undoped sample was also prepared simultaneously. The doped oxides are varied from divalent to pentavalent, including CaO, CuO, MgO, Bi_2O_3, MnO_2, IrO_2, RuO_2, SiO_2, Nb_2O_5 and V_2O_5. Fig. A-1 shows the XRD spectra for the doped and undoped samples. The standard position and intensity of the X-ray diffraction lines are also given in the figure. All samples are identified to be single phase with *W*-type hexagonal structure and no other phases are detected. The lattice parameters, *a*, *c* and *V*, are listed in Table A-1.

The bulk densities for all sintered samples are measured by two methods, Archimedean method and mass-volume method, represented by ρ_A and ρ_m, respectively. The results from both methods are also listed in Table A-1. The theoretical density of BaW is about 5.3 g/cm^3. Based on the principle of Archimedean rule, the density measured by the Archimedean method is for the particles and is not related to the porosity of the sintered samples. Therefore, there is some discrepancy between the values of ρ_A and ρ_m for all samples. Especially, for the sample doped with V_2O_5, ρ_A is about 5.1 g/cm^3, while ρ_m is only 3.3 g/cm^3. The discrepancy implies a large porosity in this sample, which has been proved by SEM morphology.

For other samples, the densities measured by two different methods are almost consistent with each other.

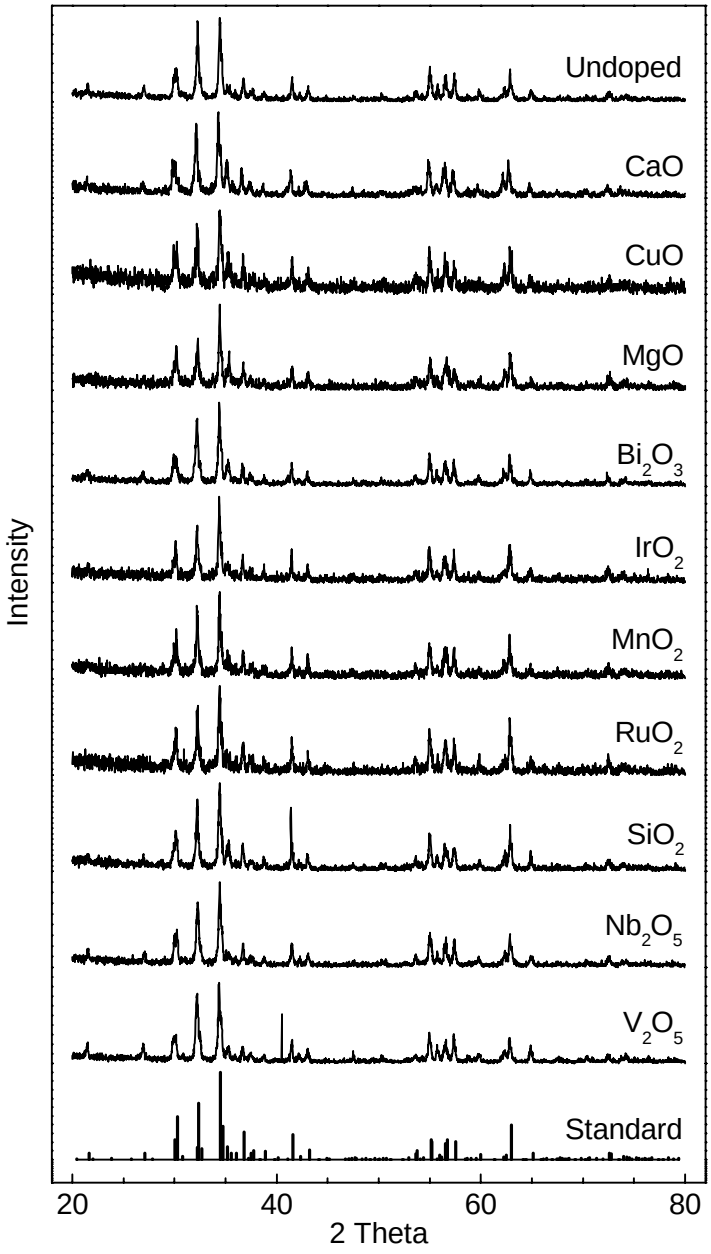

Fig. A-1. X-ray diffraction patterns for undoped and 1.0 wt% of oxide doped $BaCoZnFe_{16}O_{27}$.

The magnetization curves and *M-H* loops for sintered samples were measured using VSM with the maximum applied field of 14 kOe. The saturation magnetization M_s

was defined as the value at applied field of 14 kOe and the coercivity H_c was obtained from the *M*-*H* loop. The values of M_s and H_c for all samples are listed in Table A-2. As we know, large M_s and small H_c are desired for ideal EM absorbing materials, since the magnitude of initial permeability is related to the ratio of M_s to H_c.[88] As shown in Table A-2, M_s slightly increases with the doping of SiO_2, Nb_2O_5 and V_2O_5, and H_c decreases with the doping of CaO, Bi_2O_3, RuO_2, Nb_2O_5 and V_2O_5. Especially for the sample with V_2O_5 doping, H_c significantly decreases from 26.1 to 18.7 Oe, decreasing by about 30 %, while M_s slightly increases. Therefore, the doping of 1.0 wt% of V_2O_5 will greatly enhance the static magnetic property of $BaCoZnFe_{16}O_{27}$.

Table A-1. Lattice parameters and density for undoped and 1.0 wt% of oxide doped $BaCoZnFe_{16}O_{27}$. ρ_A and ρ_m represent the results measured by Archimedean and mass-volume method, respectively.

Doped with	Lattice Parameter			Density (g/cm^3)	
	a (nm)	*c* (nm)	*V* (nm^3)	ρ_A	ρ_m
undoped	0.5915 (1)	3.299 (2)	1.000 (1)	4.98	4.80
CaO	0.5928 (1)	3.316 (3)	1.009 (1)	5.04	4.90
CuO	0.5914 (2)	3.297 (4)	0.999 (2)	5.06	4.82
MgO	0.5915 (1)	3.298 (1)	0.999 (1)	4.91	4.71
Bi_2O_3	0.5919 (1)	3.305 (2)	1.003 (1)	5.03	4.83
IrO_2	0.5918 (1)	3.306 (3)	1.003 (1)	4.98	4.71
MnO_2	0.5916 (1)	3.304 (3)	1.001 (1)	4.97	4.74
RuO_2	0.5916 (1)	3.297 (1)	0.999 (1)	4.95	4.73
SiO_2	0.5914 (1)	3.304 (3)	1.001 (1)	5.05	4.80
Nb_2O_5	0.5923 (1)	3.311 (2)	1.006 (1)	4.76	4.57
V_2O_5	0.5924 (2)	3.303 (2)	1.004 (1)	5.07	3.28

Table A-2. Static and dynamic magnetic properties for undoped and 1.0 wt% of oxide doped $BaCoZnFe_{16}O_{27}$.

Doped with	Static Magnetic Property		Dynamic Mgnetic Property		
	M_s (emu/g)	H_c (Oe)	$\mu_0^{'}$	$\mu_{max}^{"}$	f_r (GHz)
undoped	78.2	26.1	3.0	1.2	5.6
CaO	76.5	21.9	4.2	1.3	2.2
CuO	76.9	28.4	4.4	1.5	2.9
MgO	74.6	30.9	3.6	1.1	5.3
Bi_2O_3	78.0	23.4	3.9	1.3	2.4
IrO_2	77.7	30.1	4.3	1.6	3.5
MnO_2	77.8	26.2	5.0	1.7	2.5
RuO_2	78.1	22.7	4.4	1.5	3.5
SiO_2	78.6	26.8	3.4	1.0	4.3
Nb_2O_5	78.9	25.3	4.2	1.6	3.2
V_2O_5	79.1	18.7	5.1	1.9	0.8-3.0

A.2 Electromagnetic properties

The complex permittivity of the composites filled with 50 vol% barium ferrite powders was measured from 0.5 to 16.5 GHz.

Figure A-2 shows the complex permittivity for all composites. For the undoped sample, the real and imaginary permittivity, ε' and ε'', are about 7.4 and 0.4, respectively, and are almost independent of frequency over the measured frequency range. There are no obvious changes in ε' and ε'' for the V_2O_5 doped sample, while a slight increase in ε' and ε'' for the Nb_2O_5 doped sample. However, for the samples doped with other oxides, the values of ε' and ε'' greatly increase as compared

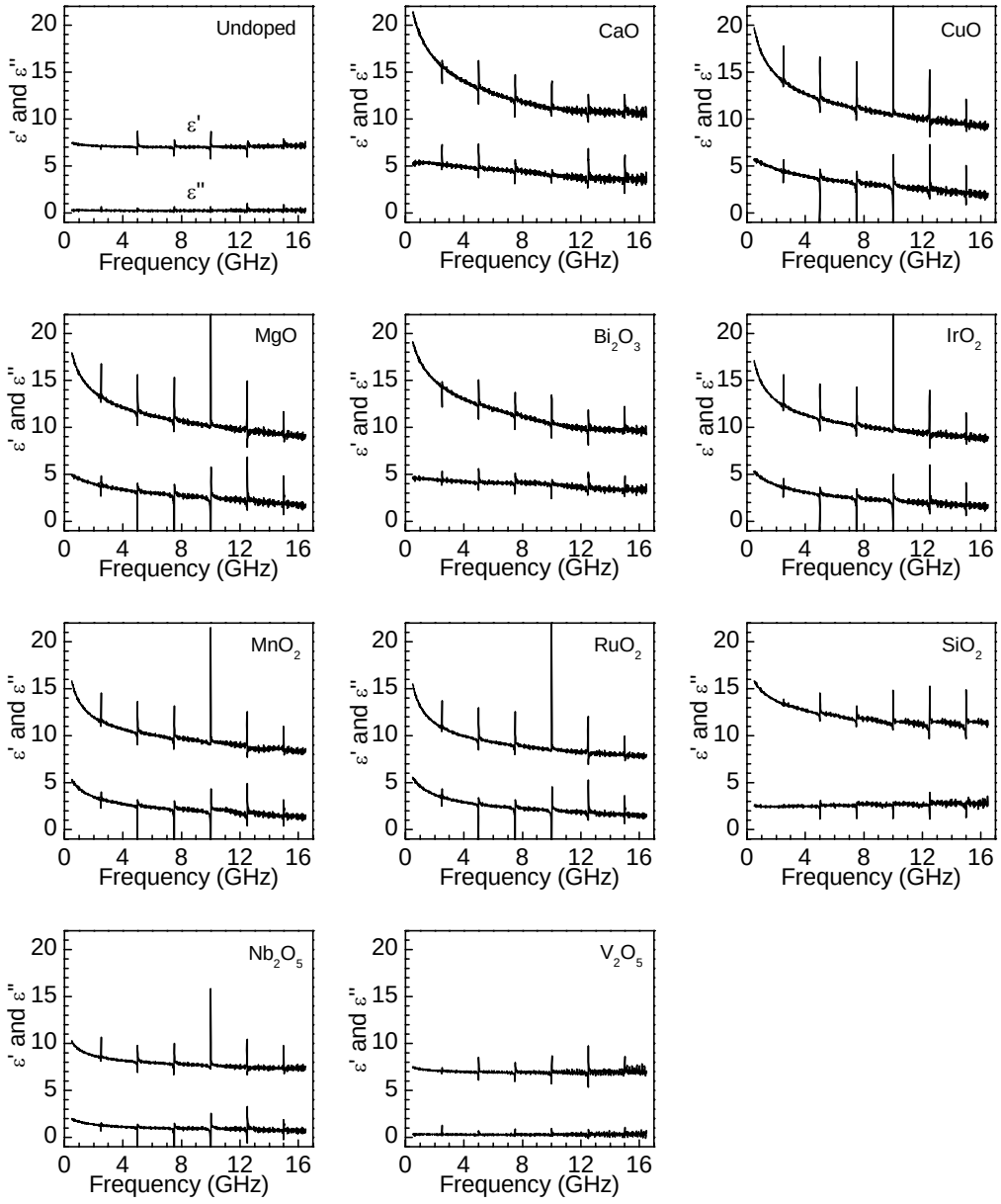

Fig. A-2. Complex permittivity spectra for all composites doped by 1.0 wt% of CaO, CuO, MgO, Bi_2O_3, IrO_2, MnO_2, RuO_2, SiO_2, Nb_2O_5 and V_2O_5. In addition, the spectrum for undoped sample is also presented for comparison.

with the undoped sample. Furthermore, for a given sample, both ε' and ε'' decrease with the increase in frequency. Especially for the samples doped with CaO and CuO, the maximum value of ε' obtained is more than 20 at 0.5 GHz.

The increase in permittivity should be attributed to the electron hopping between Fe^{2+}

and Fe^{3+}.[119, 120, 121, 122, 123] The peak of Fe^{2+} in XPS spectra is observed for the ferrites with extremely high permittivity, while disappeared for the ferrites with low permittivity. The existence of Fe^{2+} also can be indirectly confirmed by the change of the resistivity. In order to present the relationship between the resistivity and permittivity more clearly, the samples of BaW doped with various amounts of SiO_2 (0, 0.5, 0.75 and 1.0 wt%) were fabricated. The complex permittivity for the composites filled with 50 vol% ferrite powders was measured from 0.5 to 16.5 GHz. Fig. A-3 shows all permittivity spectra. Similarly, both ε' and ε'' increase with the doping amount of SiO_2. For example, at 1.0 GHz, ε' are 7.4 for the undoped sample, while 11.3, 13.3 and 14.6 for the samples doped with SiO_2 of 0.5, 0.75 and 1.0 wt%. On the other hand, the resistivity was also measured using the four probes method for the bulk samples and are shown in Fig. A-3. By doping with SiO_2 from 0 to 1.0 wt%, the resistivity reduces rapidly from 2.4×10^6 to 0.3×10^6 Ω·cm. Interestingly, the values of ε' (at 0.5 and 16.5 GHz) and ε'' have a good linear relationship with resistivity, as shown in Fig. A-4. The origin of the linear relationship is not clear and need more investigation. However, the following conclusion can be made. For the sample with large permittivity, the resistivity must be low, which is induced by the hopping between Fe^{2+} and Fe^{3+}. In conclusion, in order to fabricate the sample with low permittivity, it is necessary to avoid the formation of Fe^{2+} ions.

The complex permeability of the composites filled with 50 vol% barium ferrite powders was measured from 0.1 to 16.5 GHz, as shown in Fig. A-5. The high-frequency magnetic parameters, μ_0', μ_{max}'' and f_r are listed in Table A-2. Here, μ_0', the static permeability, is also defined as the real permeability at 0.1 GHz. It is obvious that, most of oxides doping can effectively improve the permeability and shift

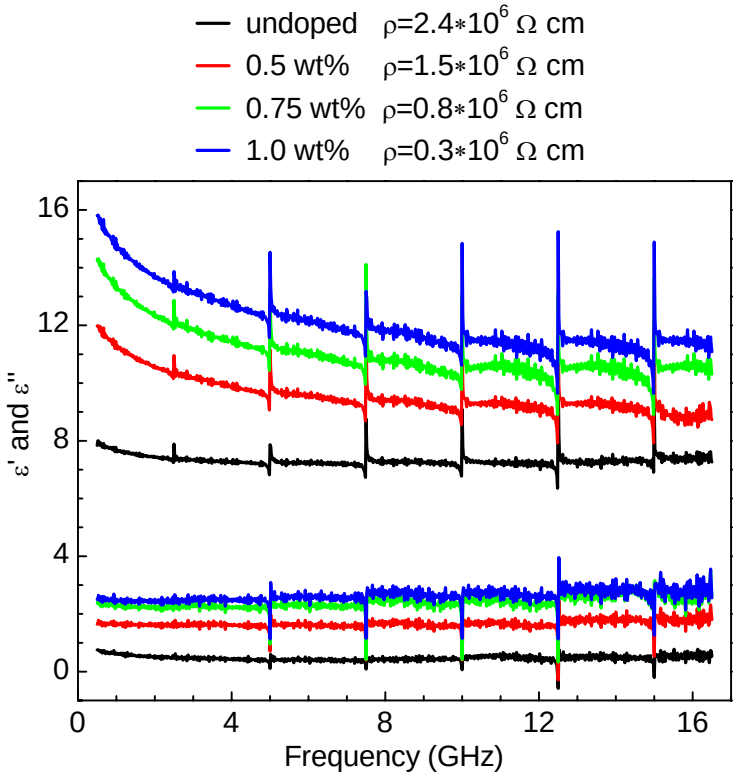

Fig. A-3. Complex permittivities ε' and ε'' from 0.5 to 16.5 GHz for BaW composites doped with various amounts of SiO_2. The values of resisitivity for each sample are also indicated.

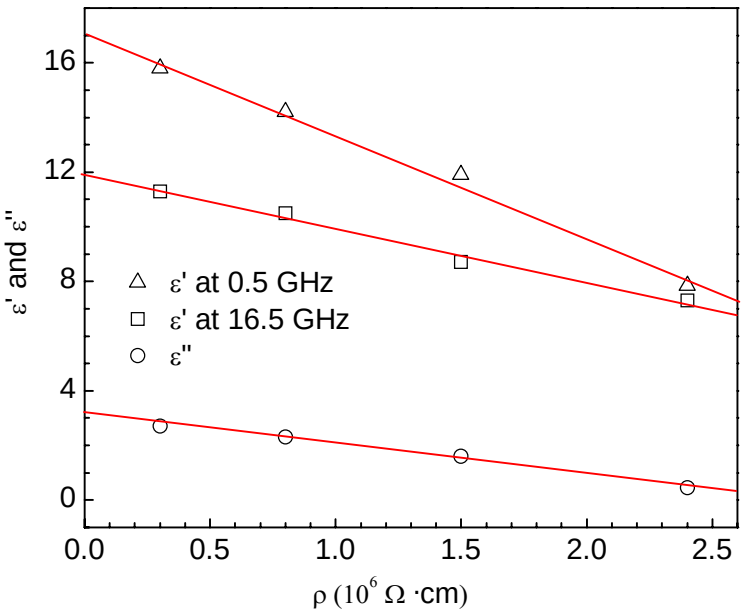

Fig. A-4. The relationship between resisitivity and permittivities ε' and ε'' for BaW composites doped with various amounts of SiO_2. The straight lines represent the results of linear fitting.

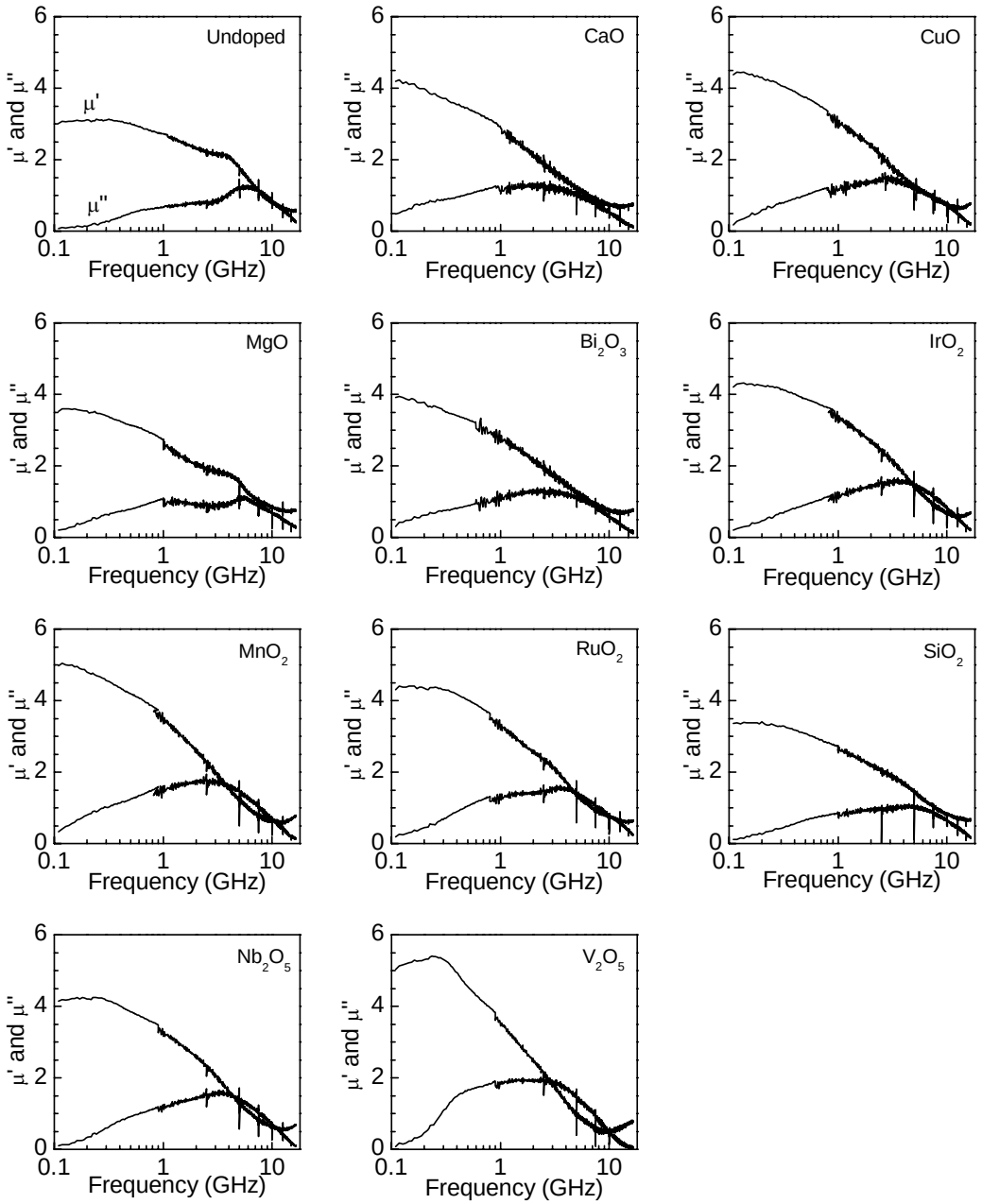

Fig. A-5. Complex permeability spectra for all composites doped by 1.0 wt% of CaO, CuO, MgO, Bi_2O_3, IrO_2, MnO_2, RuO_2, SiO_2, Nb_2O_5 and V_2O_5. In addition, the spectrum for undoped sample is also presented for comparison.

the resonance to low frequency. Especially for V_2O_5 doped sample, $\mu_0^{'}$ and $\mu_{max}^{"}$ increase to 5.1 and 1.9 from 3.0 and 1.2 for undoped sample, respectively. In addition, for the sample with MnO_2 doping, $\mu_0^{'}$ and $\mu_{max}^{"}$ also increase to 5.0 and 1.7,

respectively. As we know, high permeability is desired for an ideal EM absorption material. Taking into account the results of dynamic magnetic property, we can deduce that both V_2O_5 and MnO_2 are possible candidates for doping in BaW to enhance the absorbing performance. However, as shown in Fig. A-2, the permittivity for MnO_2 doped composite is very high, which is definitely disadvantage to EM absorption. Therefore, V_2O_5 is the most promising candidate to enhance the absorbing ability in BaW.

APPENDIX B

Table B-1. Lattice parameters (*a* and *c*) and cell volume *V* for *Y*-type ferrites of $Ba_2Co_xZn_{2-x}Fe_{12}O_{22}$, $Ba_2Ni_xCo_{2-x}Fe_{12}O_{22}$ and $Ba_2Zn_xNi_{2-x}Fe_{12}O_{22}$.

x		*a* (nm)	*c* (nm)	*V* (nm^3)
Co_xZn_{2-x}-Y	0	0.5892 (2)	4.388 (4)	1.319 (2)
	0.4	0.5890 (2)	4.387 (3)	1.318 (2)
	0.8	0.5885 (3)	4.387 (1)	1.316 (2)
	1.2	0.5885 (1)	4.382 (1)	1.314 (1)
	1.6	0.5882 (2)	4.381 (2)	1.313 (1)
	2.0	0.5876 (1)	4.380 (2)	1.310 (1)
Ni_xCo_{2-x}-Y	0.8	0.5873 (3)	4.372 (4)	1.306 (3)
	1.0	0.5871 (2)	4.368 (1)	1.304 (1)
	1.2	0.5867 (1)	4.364 (3)	1.301 (1)
	1.5	0.5863 (1)	4.361 (2)	1.298 (1)
Zn_xNi_{2-x}-Y	0	0.5861 (1)	4.350 (2)	1.294 (1)
	0.4	0.5872 (3)	4.363 (2)	1.303 (2)
	0.8	0.5877 (2)	4.374 (5)	1.308 (2)
	1.2	0.5886 (1)	4.377 (3)	1.313 (1)
	1.6	0.5886 (2)	4.379 (3)	1.314 (2)
	2.0	0.5890 (1)	4.384 (2)	1.317 (1)

Table B-2. Static magnetic properties for CoZn-, NiCo- and ZnNi-substituted BaY.

x		H_θ (kOe)	M_s (emu/g)	H_c (Oe)
Co_xZn_{2-x}-Y	0	9.0	35.42	6.9
	0.4	11.5	39.96	11.8
	0.8	21.2	41.89	17.7
	1.2	23.8	41.40	24.9
	1.6	32.2	37.41	32.2
	2.0	41.5	32.83	39.1
Ni_xCo_{2-x}-Y	0.8	29.6	28.28	34.0
	1.0	27.2	27.29	35.9
	1.2	19.8	26.32	36.9
	1.5	19.2	24.84	36.2
Zn_xNi_{2-x}-Y	0	18.0	20.47	36.6
	0.4	12.3	27.24	23.6
	0.8	10.9	31.76	17.1
	1.2	11.5	34.43	12.0
	1.6	10.4	33.81	9.7
	2.0	8.7	30.94	6.6

Table B-3. Dynamic magnetic parameters for composites of CoZn-, NiCo- and ZnNi-substituted BaY.

x		$\mu_0^{'}$	$\mu_{max}^{''}$	f_{r1} (GHz)	f_{r2} (GHz)	f_{r3} (GHz)
Co_xZn_{2-x}-Y	0	4.7	1.6	~ 1.7		0.08
	0.4	3.6	1.3	~ 3.2	~ 1.6	-
	0.8	2.9	1.2	5.3	2.4	-
	1.2	2.5	0.92	8.6	3.4	-
	1.6	1.8	0.63	14.1	4.8	-
	2.0	1.6	0.38	-	7.1	-
Ni_xCo_{2-x}-Y	0.8	1.8	0.56	13.0	4.7	-
	1.0	1.8	0.60	11.7	4.0	-
	1.2	2.0	0.64	10.1	3.6	-
	1.5	2.1	0.70	7.8	2.9	-
Zn_xNi_{2-x}-Y	0	2.6	0.84	6.1	1.6	-
	0.4	3.1	1.1	4.4	1.4	0.13
	0.8	3.9	1.3	3.4	1.3	0.13
	1.2	4.4	1.5	~ 2.9	~ 1.1	0.12
	1.6	4.6	1.5	~ 2.3	~ 1.1	0.10
	2.0	4.8	1.6	~ 1.6		0.08

Table B-4. The optimum thickness t_o, the upper- and lower-frequency limits, f_{up} and f_{low}, for absorption of more than 10 dB, and the relative bandwidth of $W = f_{up} / f_{low}$ for CoZn-, NiCo- and ZnNi-substituted BaY.

x		t_o (mm)	f_{low} (GHz)	f_{up} (GHz)	$W_{\max}$
Co_xZn_{2-x}-Y	0	3.7	3.9	10.7	2.74
	0.4	3.0	4.7	12.2	2.60
	0.8	2.2	7.0	16.5	2.36
	1.2	2.0	8.3	16.5	1.99
	1.6	1.9	10.3	16.5	1.60
	2.0	1.7	13.6	16.5	1.21
Ni_xCo_{2-x}-Y	0.8	2.0	10.2	16.5	1.62
	1.0	2.1	9.4	16.5	1.76
	1.2	2.2	8.6	16.4	1.91
	1.5	2.5	7.3	14.9	2.04
Zn_xNi_{2-x}-Y	0	3.1	5.4	12.1	2.24
	0.4	3.2	4.5	12.3	2.73
	0.8	3.2	4.3	12.4	2.88
	1.2	3.3	3.9	11.8	3.03
	1.6	3.4	3.9	11.0	2.82
	2.0	3.7	3.9	10.7	2.74

REFERENCES

[1] W.H. Emerson, *IEEE Trans. Antennas & Propag.* **21**, 484 (1973).

[2] P.T.C. Wong, B. Chambers, A.P. Anderson and P.V. Wright, *Electron. Lett.* **28**, 1651 (1992).

[3] K. Naishadham and P.K. Kadaba, *IEEE Trans. Microw. Theory & Tech.* **39**, 1158 (1991).

[4] R.A. Stonier, *Sampe Journal*, **27**, 9 (1991).

[5] T. Yamamuna, T. Toshikawa and M. Shibuya, *Electromagnetic Wave Absorbing Materials*, USP 5094907, (1992).

[6] Y. Naito and K. Suetake, *IEEE Trans. Microw. Theory & Tech.* **19**, 65 (1971).

[7] K.J. Vinoy and R.M. Jha, *Radar Absorbing Materials* Ed. R.M. Jha, (Kluwer academic publishers), 108 (1996).

[8] S. Yoshida, M. Sato, E. Sugawara and Y. Shimada, *J. Appl. Phys.* **85**, 4636 (1999).

[9] T. Maeda, S. Sugimoto, T. Kagotani, D. Book, M. Homma, H. Ota and Y. Houjou, *Mater. Trans. JIM* **41**, 1172 (2000).

[10] M. Sato, S. Yoshida, E. Sugawara and Y. Shimada, *J. Magn. Soc. Jpn.* **20**, 4214 (1996).

[11] M. Matsumoto and Y. Miyata, *IEEE Trans. Magn.* **33**, 523 (1997).

[12] L. Olmedo, G. Chateau, C. Deleuze and J.L. Forveille, *J. Appl. Phys.* **73**, 6992 (1993).

[13] G. Viau, F. Ravel, O, Acher, F. Fievet-Vincent and F. Fievet, *J. Appl. Phys.* **76**, 6570 (1994).

[14] S. Sugimoto, T. Maeda, D. Book, T. Kagotani, K. Inomata, M. Homma, H. Ota, Y. Houjou and R. Sato, *J. Alloy. & Compd.* **330**, 301 (2002).

[15] D. Rousselle, A. Berthault, O. Acher, J.P. Bouchaud and P.G. Zerah, *J. Appl. Phys.* **74**, 475 (1993).

[16] G. Alex, *Modern Ferrite Technology*, Van Nostrand Reinhold, 21 (1990).

[17] Y.Y. Li and G.D. Li, *Physics of Ferrite (in Chinese)*, Scientific Publish, (1972).

[18] J.L. Snoek, *Physica* **14**, 207 (1948).

[19] J. Nicolas, *Ferromagnetic Materials*, Ed. E.P. Wohlfarth, North-Holland Publishing Company, **2**, 243 (1980).

[20] M.B. Amin and J.R. James, *Radio & Electron. Engi.* **51**, 209 (1981).

[21] C. Okazaki, T. Kubota and S. Mori, *J. Phys. Soc. Jpn.* **16**, 119 (1961).

[22] G. Winkler, *Magnetic Properties of Materials,* Ed. J. Smit, (McGraw-Hill, London),

20 (1971).

[23] H. Kojima, *Ferromagnetic Materials*, Ed. E.P. Wohlfarth, North-Holland Publishing Company, **3**, 308 (1982).

[24] H. Kojima, *Ferromagnetic Materials*, Ed. E.P. Wohlfarth, North-Holland Publishing Company, **3**, 309 (1982).

[25] H. Kojima, *Ferromagnetic Materials*, Ed. E.P. Wohlfarth, North-Holland Publishing Company, **3**, 321 (1982).

[26] V. Adelskold, *Arkiv Kemi. Mineral. Geol.* **12A**, 1 (1938).

[27] R. Valenzuela, *Magnetic Ceramics,* Ed. B. Dunn, J.W. Goodby and A.R. West, (Cambridge University Press), 33 (1994).

[28] G. Albanese, M. Carbucicchio, and G. Asti, *Appl. Phys.* **11**, 81 (1976).

[29] G. Albanese, M. Carbucicchio, and A. Deriu, *Appl. Phys.* **7**, 227 (1975).

[30] G. Albanese, A. Deriu and S. Rinaldi, *J. Phys. C. Solid State Phys.* **9**, 1313 (1976).

[31] P.W. Anderson, *Exchange in Insulators*, Eds., G.T. Rado and H. Suhl, (Academic Press, New York, London), **Vol. 1**, 25-86 (1963).

[32] R.C. O'Handley, *Modern Magnetic Materials: Principles and Applications*, Ed. R.C. O'Handley, A Wiley-Interscience Publication, 124 (1999).

[33] L. Jahn and H.G. Muller, *Phys. Status Solidi A* **35**, 723 (1969).

[34] H. Kojima, *Ferromagnetic Materials*, Ed. E.P. Wohlfarth, North-Holland Publishing Company, **3**, 324 (1982).

[35] M. Sugimoto, *Ferromagnetic Materials*, Ed. E.P. Wohlfarth, North-Holland Publishing Company, **3**, 411 (1982).

[36] J. Smit, *J. Phys. Rad.* **20**, 370 (1959).

[37] N. Fuchikami, *J. Phys. Soc. Jpn,* **20**, 760 (1965).

[38] H.J. Kwon, J.Y. Shin and J.H. Oh, *J. Appl. Phys.* **75**, 6109 (1994).

[39] M. Matsumoto and Y. Miyata, *J. Appl. Phys.* **79**, 5486 (1996).

[40] I.G. Chen, S.H. Hsu and Y.H. Chang, *J. Appl. Phys.* **87**, 6247 (2000).

[41] L. Landau and E. Lifshitz, *Phys. Zh. Sov.Un.*, **8**, 153 (1935).

[42] C. Kittle, *J. Phys. Radium* **12**, 332 (1951).

[43] G.T. Rado, *Rev. Mod. Phys.* **25**, 81 (1953).

[44] J.Y. Shin and J.H. Oh, *IEEE Trans. Magn.* **29**, 3437 (1993).

[45] H.S. Cho and S.S. Kim, *IEEE Trans. Magn.* **35**, 3151 (1999).

[46] I. Nedkov, A. Petkov and V. Karpov, *IEEE Trans. Magn.* **26**, 1483 (1990).

[47] S.G. Abarenkova, V.I. Ivanova, V.N. Karpov, A.A. Kitaizev, I.I. Mechkauskas and L.K. Michailovski, *The Vth International Conference on Microwave Ferrites,* Proc., Vilnus, USSR, October 8-14, 170 (1980).

[48] E. Brando, H. Vincent, O. Dubrinfaut, A. Fourrier-Lamer and R. Lebougeois, *J. Phys. IV France* **7**, C1-421, (1997).

[49] T. Nakamura and K.I. Hatakeyama, *IEEE Trans. Magn.* **36**, 3415 (2000).

[50] Y.J. Kim and S.S. Kim, *IEEE Trans. Magn.* **38**, 3108 (2002).

[51] P. Lubitz, *J. Appl. Phys.* **87**, 4978 (2000).

[52] P. Lubitz and F.J. Rachford, *J. Appl. Phys.* **91**, 7613 (2002).

[53] Y. Bai, J. Zhou, Z.L. Gui and L.T. Li, *Mater. Sci. & Engi. B* **103**, 115 (2003).

[54] H.J. Zhang, Y. Xi and L.Y. Zhang, *J. European Ceram. Soc.* **22**, 835 (2002).

[55] C.S. Wang, L.T. Li, J. Zhou, X.W. Qi, Z.X. Yue and X.H. Wang, *J. Magn. Magn. Mater.* **257**, 100 (2003).

[56] X.H. Wang, T.L. Ren, L.T. Li, Z.L. Gui, S.Y. Su, Z.X. Yue and J. Zhou, *J. Magn. Magn. Mater.* **234**, 255 (2001).

[57] X.H. Wang, L.T. Li, S.Y. Su, Z.L. Gui, Z.X. Yue and J. Zhou, *J. European Ceram. Soc.* **23**, 715 (2003).

[58] J.E. Bao, J. Zhou, Z.X. Yue, L.T. Li and Z.L. Gui, *Mater. Sci. & Engi. B* **99**, 98 (2003).

[59] K. Haga, S. Sugimoto, T. Kagotani and K. Inomata, *Mater. Trans.* **45**, 2606 (2004).

[60] S. Sugimoto, K. Haga, T. Kagotani and K. Inomata, *J. Magn. Magn. Mater.* **290-291**, 1188 (2005).

[61] H. Ota, M. Kimura, R. Sato, K. Okayama, S. Kondo and M. Homma, *IEEE Trans. Magn.* **35**, 590 (1999).

[62] S. Sugimoto, S. Kondo, K. Okayama, H. Nakamura, D. Book, T. Kagotani and M. Homma, *IEEE Trans. Magn.* **35**, 3154 (1999).

[63] T. Kagotani, D. Fujiwara, S. Sugimoto, K. Inomata and M. Homma, *J. Magn. Magn. Mater.* **272-276**, e1813 (2004).

[64] H.I. Hsiang and H.H. Duh, *J. Mater. Sci.* **36**, 2081 (2001).

[65] D.Y. Kim, Y.C. Chung, T.W. Kang and H.C. Kim, *IEEE Trans. Magn.* **32**, 555 (1996).

[66] S.S. Kim, S.B. Jo, K.I. Gueon, K.K. Choi, J.M. Kim and K.S. Churn, *IEEE Trans. Magn.* **27**, 5462 (1991).

[67] H. Sakai, K. Hanawa and K. Aoyagi, *IEEE Trans. Magn.* **28**, 3355 (1992).

[68] R. Muller, *J. Magn. Magn. Mater.* **120**, 61 (1993).

[69] C. Surig, K.A. Hempel and D. Bonnenberg, *IEEE Trans. Magn.* **30**, 4092 (1994).

[70] J. Ding, R. Street and H. Nishio, *J. Magn. Magn. Mater.* **164**, 385 (1996).

[71] M.A. El Hiti, A.L. El Shora, A.S. Seoud and S.M. Hammed, *Phase Trans.* **56**, 35 (1996).

[72] X.Y. Liu, J. Wang, L.M. Gan, S.C. Ng and J. Ding, *J. Magn. Magn. Mater.* **184**, 344 (1998).

[73] K. Haneda, C. Miyakawa and K. Goto, *IEEE Trans. Magn.* **23**, 3134 (1987).

[74] H.S. Shin and S.J. Kwon, *Ferrites: ICF 6*, Tokyo and Kyoto, 1402 (1992).

[75] H. Hibst, *Angew. Chem. Int. Ed. Engl.* **21** 270 (1982).

[76] P. Singh, V.K. Babbar, A. Razdan, S.L. Srivastava and R.K. Puri, *Mater. Sci. & Engi. B* **67**, 132 (1999).

[77] K. Okada and T. Sekino, *Impedance Measurement Handbook*, (Agilent Technologies Co. Ltd.), (2003).

[78] G.D. Zhou, *Testing of Crystal Structure (in Chinese)*, (Scientific Publish), 44 (1984).

[79] R. Grossinger, *Phys. Status Solidi A* **66**, 665 (1981).

[80] R. Grossinger, *J. Magn. Magn. Mater.* **28,** 137 (1982).

[81] D.T. Margulies, F.T. Parker, F.E. Spada, R.S. Goldman, J. Li, R. Sinclair and A.E. Berkowitz, *Phys. Rev. B* **53**, 9175 (1996).

[82] Z.W. Li, C.K. Ong, Z. Yang, F.L. Wei, X.Z. Zhou, J.H. Zhao and A. Morrish, *Phys. Rev. B* **62**, 6530 (2000).

[83] L. Neel, *J. Phys.* (France) **9**, 148 (1948).

[84] L. Neel, *J. Phys.* (France) **9**, 193 (1948).

[85] A.T. Aldred and P.H. Froehle, *Int. J. Magn.* **2**, 195 (1972).

[86] H.M. Musal, Jr. and H.T. Hahn, *IEEE Trans. Magn.* **25**, 3851 (1989).

[87] Y. Kotsuka and H. Yamazaki, *IEEE Trans. Electromagn. Compat.* **42**, 116 (2000).

[88] G.F. Dionne, *IEEE Trans. Magn.* **39**, 3121 (1991).

[89] G.J. Yin and S.B. Liao, *IEEE Trans. Magn.* **27**, 5459 (1991).

[90] *Handbook of Chemistry and Physics*, electronic version, Ed. by D. R. Lide, 12-14 (1998).

[91] H. Graetsh, H. Haberey, R. Leckebusch, M. Rosenberg and K. Sahl, *IEEE Trans. Magn.* **20**, 495 (1984).

[92] A. Collomb, O. Wolfers and X. Obradors, *J. Magn. Magn. Mater.* **62**, 57 (1986).

[93] A. Paoluzi, F. Licci, O. Moze, G. Turilli, A. Deriu, G. Albanese and E. Calabrese, *J. Appl. Phys.* **63**, 5074 (1988).

[94] J. Smit and H.P.J. Wijn, *Ferrites* (Philips Technical Library, Eindhoven, Netherlands), 1959.

[95] R.A. Braden, I. Cordon and R.L. Harvey, *IEEE Trans. Magn.* **2**, 43 (1966).

[96] M. Sugimoto, *Ferromagnetic Materials*, Ed. E.P. Wohlfarth (North-Holland, Netherlands), **3**, 393 (1982).

[97] J. Verwell, in *Magnetic Properties of Materials*, Ed. J. Smit (McGraw-Hill, New York), 64 (1971).

[98] J.L. Snoek, *Physica (Utrecht)* **XIV**, 245 (1948).

[99] Z.W. Li, L.F. Chen and C.K. Ong (unpublished).

[100] S.C. Jiang, *Stealthy Materials*, Ed. L. Y. Xing, (Chemical Industry Press, Beijing), 96 (2004).

[101] H.G. Zhang, J. Zhou, Y.L. Wang, L.T. Li, Z.X. Yue and Z.L. Gui, *IEEE Trans. Magn.* **38**, 1797 (2002).

[102] H.I. Hsiang, C.S. Hsi, T.C. Lee and C.H. Chang, *J. Magn. Magn. Mater.* **268**, 186 (2004).

[103] A. Goldman, *Modern Ferrite Technology*, Ed. by A. Goldman, (Van Nostrand Reinhold, New York), 125 (1990).

[104] J. Smit, *Magnetic Properties of Materials*, Ed. by J. Smit (McGraw-Hill, New York), 1 (1971).

[105] M. Obol and C. Vittoria*, J. Appl. Phys.* **94**, 4013 (2003).

[106] R.D. Shannon, *Acta Cryst.* **A32**, 751 (1976).

[107] S.G. Lee and S.J. Kwon, *J. Magn. Magn. Mater.* **153**, 279 (1996).

[108] A. Goldman, *Modern Ferrite Technology*, edited by A. Goldman (Van Nostrand Reinhold, New York), 12 (1990).

[109] G. Albanese, M. Carbucicchio and G. Asti, *Nuovo Cimento* **14**, 207 (1975).

[110] J. Verwell, *Magnetic Properties of Materials,* **13**, Ed. J. Smit, (McGraw-Hill, New York), 101 (1971).

[111] Y.W. Du, *Ferrites*, (Publishing House of Jiangsu Science and Technology), 109 (1996).

[112] H. Kojima, *Ferromagnetic Materials*, Ed. E.P. Wohlfarth (North-Holland, Amsterdam), **3**, 357 (1982).

[113] J. Verwell, *Magnetic Properties of Materials,* **13**, Ed. J. Smit, (McGraw-Hill Book Company), 83 (1971).

[114] A.M. Clogston, *Bell Syst. Tech. J.* **34**, 739 (1995).

[115] W. Wernsdorfer, E. Bonet Orozco, K. Hasselbach, A. Benoit, B. Barbara, N. Demoncy, A. Loiseau, H. Pascard and D. Mailly, *Phys. Rev. Lett.* **78**, 1791 (1997).

[116] Y.D. Zhang, J.I. Budnick, W.A. Hines, S.A. Majetich and E.M. Kirkpatrick, *Appl. Phys. Lett.* **76**, 94 (2000).

[117] M.Z. Wu, Y.D. Zhang, S. Hui, T.D. Xiao, S.H. Ge, W.A. Hines, J.I. Budnick and M.J. Yacaman, *J. Appl. Phys.* **92**, 6809 (2002).

[118] E.E. Carpenter, S. Calvin, R.M. Stroud and V.G. Harris, *Chem. Mater.* **15**, 3245 (2003).

[119] A.J. Bosmann and C.C. Creve, *Phys. Rev.* **144**, 763 (1966).

[120] P.K. Larsen and J.M. Robertson, *J. Appl. Phys.* **45**, 2867 (1974).

[121] S. Besenicar, M. Drofenik, T. Koemao and V. Krasevec, *IEEE Trans. Magn.* **24**, 1838 (1988).

[122] T.S. Rao, *Ferrite Materials Science and Technology,* Ed. by B. Viswanathan and V.R.K. Murthy (Springer, Narosa, Berlin), 38 (1990).

[123] H.G. Zhang, L.T. Li, Y.L. Wang, J. Zhou, Z.X. Yue and Z.L. Gui, *J. Appl. Phys.* **91**, 5230 (2002).